JUSTUS-LIEBIG-UNIVERSITÄT GIESSEN

Institute of Applied Physics

Deciphering Self-Assembly Mechanisms and Chemical Reactions of Organic Building Blocks on Metal Surfaces by Chemical Bond Imaging

Entschlüsselung von Selbstassemblierungsmechanismen und Chemischen Reaktionen Organischer Moleküle auf Metallsubstraten mittels Chemical Bond Imaging

Dissertation

presented to Faculty 07 - Mathematics and Computer Science, Physics, Geography of Justus-Liebig-Universität Gießen

in candidacy for the degree of

Doctor rerum naturalium

Dr. rer. nat.

Miguel Wiche

Date of Thesis Submission: 24th September 2025

Date of Disputation: 10th December 2025

Reviewers:

1st Prof. Dr. André Schirmeisen

2nd Prof. Dr. Hermann A. Wegner

Abstract

In recent years, the novel field of on-surface synthesis has been established as one of the main tools for constructing customized, low-dimensional organic nanostructures via bottom-up approaches on atomically flat metal substrates. The self-assembly of the molecular precursors, a process that often serves as pre-step of the on-surface reaction, determines the precise local arrangement of atoms and bonds in neighboring molecules, thus playing a decisive role in product formation. Thereby, intermolecular interactions between hydrogen and fluorine atoms have proven to be a valuable tool to steer molecular alignments. In this work, the mainly unexplored intermolecular hydrogen-fluorine interaction is systematically investigated on inert Au(111) and reactive Cu(111) substrates, using a linear, unilaterally fluorinated 1,2,10,11,12,14-hexafluoropentacene molecule as a model system. In the combined scanning tunneling microscopy and chemical bond imaging study, the local arrangement of hydrogen and fluorine atoms in neighboring molecules is determined in the picometer range and angular variations of a few degrees. While on Au(111) the intermolecular interactions between the molecules are the main contributor to the self-assembly, the higher reactivity of Cu(111) results in different adsorption geometries and molecular arrangements. The highly precise self-assembly study provides new insights into the on-surface interaction of hydrogen and fluorine atoms, thereby highlighting its significance for the field of on-surface synthesis. An on-surface reaction that solely takes place using halogenated precursors is the on-surface Ullmann coupling reaction, which enables the formation of covalent carbon-carbon bonds with the underlying metal surface as a catalyst. However, when applying Ullmann coupling reaction steps, complex self-assembly mechanisms can occur when halogenated precursors interact with the metal surface. Further, cleaved halogens adsorbed on the surface may potentially inhibit the reaction steps. Hence, there is a growing demand for halogen-free precursors for on-surface reactions. Recently, it has been demonstrated that halogen-free (6)Cycloparaphenylene ((6)CPP) molecules are suited to thermally induce a ring-opening polymerization reaction for the synthesis of graphene and biphenylene nanoribbons of confined widths. However, the mechanism of the ring-opening polymerization and the use of cycloparaphenylenes as precursors have not been investigated sufficiently. To contribute to the fundamental understanding of this remarkable reaction, in this thesis we systematically investigate the influence of the ring strain, which decreases with increasing ring size, using a set of cycloparaphenylenes of different sizes ((6)CPP vs. (8)CPP vs. (10)CPP). Our results demonstrate that the ring-opening polymerization is facilitated when using smaller, highly strained cycloparaphenylenes. For larger molecules with lower strain energies, the initial ring-opening is hampered, leading to only partial polymerization for (8)CPP and no polymerization in case of (10)CPP. Additionally, dehydrogenation of individual phenyl rings in intact molecules is observed for (8)CPP and (10)CPP, which further impedes the polymerization reaction.

Kurzzusammenfassung

In den vergangenen Jahren hat sich das noch junge Forschungsfeld der oberflächengestützten Synthese als eines der wichtigsten Werkzeuge zur Herstellung maßgeschneiderter, organischer Nanostrukturen durch Bottom-up Ansätze auf atomar flachen Metallsubstraten etabliert. Die Selbstassemblierung der molekularen Präkursoren, welche als Vorstufe zur Oberflächenreaktion fungieren kann, bestimmt die exakte lokale Anordnung der Atome und Bindungen in benachbarten Molekülen und ist somit essenziell bei der Produktbildung. Dabei haben sich intermolekulare Wechselwirkungen zwischen Wasserstoff- und Fluoratomen als wirksames Mittel zur Steuerung der molekularen Anordnungen erwiesen. In dieser Arbeit wird die weitgehend unerforschte intermolekulare Wechselwirkung zwischen Wasserstoff und Fluor untersucht, wobei ein lineares, unilateral fluoriertes 1,2,10,11,12,14-Hexafluorpentacen als Modellsystem verwendet wird. In der kombinierten Rastertunnelmikroskop und chemical bond imaging Studie wird die lokale Anordnung von Wasserstoff- und Fluoratomen in benachbarten Molekülen im Pikometerbereich und Winkeln von wenigen Grad bestimmt. Während die intermolekularen Wechselwirkungen zwischen den Molekülen auf Au(111) den Hauptbeitrag zur Selbstassemblierung liefern, führt die stärkere Wechselwirkung auf Cu(111) zu unterschiedlichen Adsorptionsgeometrien und Molekülanordnungen. Die hochpräzise Bestimmung der Adsorptionsgeometrie ermöglicht neue Einblicke in die Wechselwirkung von Wasserstoff- und Fluoratomen auf Oberflächen und unterstreicht die Signifikanz dieser Wechselwirkung für das Forschungsgebiet der oberflächengestützten Synthese. Eine Oberflächenreaktion, die unter Verwendung halogenierter Präkursoren abläuft, ist die oberflächengestützte Ullmann-Kupplung, welche die Bildung kovalenter Kohlenstoffbindungen mit der katalysierenden Metalloberfläche ermöglicht. Bei der Selbstassemblierung halogenierter Präkursoren treten komplexe Mechanismen auf, weswegen diese schwer zu prognostizieren ist. Des Weiteren können auf der Oberfläche adsorbierte, abgespaltene Halogene die Reaktion der Moleküle hemmen. Daher besteht ein wachsender Bedarf an halogenfreien Präkursoren für die oberflächengestützte Synthese. Kürzlich wurde demonstriert, dass halogenfreie (6)Cycloparaphenylen-Moleküle ((6)CPP) geeignet sind, mittels thermischer Ringöffnungspolymerisationsreaktion Graphen- und Biphenylen-Nanostrukturen definierter Breite zu synthetisieren. Der Mechanismus der Ringöffnung und die Verwendung von Cycloparaphenylenen als Präkursoren sind jedoch bis dato nicht weitreichend erforscht. Um zum grundlegenden Verständnis dieser bemerkenswerten Reaktion beizutragen, wird in dieser Arbeit systematisch der Einfluss der Ringspannung, welche mit zunehmender Ringgröße abnimmt, unter Verwendung einer Serie verschieden großer Cycloparaphenylenene ((6)CPP vs. (8)CPP vs. (10)CPP) untersucht. Die Ergebnisse zeigen, dass die Ringöffnungspolymerisation bei kleineren Cycloparaphenylenen mit großer Ringspannung begünstigt ist. Bei größeren Molekülen mit kleinerer Ringspannung ist die initiale Ringöffnung erschwert, was bei (8)CPP nur zur teilweisen und bei (10)CPP zu keiner Polymerisation führt. Darüber hinaus wird bei (8)CPP und (10)CPP eine Abspaltung von Wasserstoffatomen in Phenylringen intakter Moleküle beobachtet, was die Polymerisationsreaktion zusätzlich hemmt.

Contents

Abstract I

Kurzzusammenfassung III

1 Introduction 1

2 Theory 3
2.1 Scanning Probe Microscopy . . . 3
2.2 Scanning Tunneling Microscopy . . . 5
2.2.1 Constant Current and Constant Height Mode . . . 7
2.3 Atomic Force Microscopy . . . 9
2.3.1 Forces Between Tip and Sample . . . 9
2.3.2 General Working Principle of Atomic Force Microscopy . . . 12
2.3.3 Frequency Modulation Atomic Force Microscopy . . . 15
2.3.4 Chemical Bond Imaging . . . 17
2.4 On-Surface Self-Assembly Processes of Organic Molecules . . . 20
2.4.1 The Halogen Bond in On-Surface Self-Assembly Processes . . . 22
2.5 On-Surface Synthesis . . . 24
2.5.1 On-Surface Ullmann Coupling . . . 25

3 Experimental 27
3.1 Instrumentation . . . 27
3.2 Sample Preparation . . . 29
3.2.1 Crystal Cleaning . . . 29
3.2.2 Molecule Evaporation . . . 30
3.2.3 Tip Preparation and Characterization . . . 30
3.3 Experimental Details on Chapter 4 . . . 31
3.4 Experimental Details on Chapter 5 . . . 31

4 Self-Assembly of Unilaterally Fluorinated Pentacene Molecules on Au(111) and Cu(111) 33
4.1 Introduction . . . 33
4.2 Results and Discussion . . . 35
4.2.1 Self-Assembly Process of F_6PEN on Au(111) . . . 35
4.2.2 Self-Assembly Process of F_6PEN on Cu(111) . . . 46
4.2.3 Comparison of Molecular Bending on Au(111) and Cu(111) . . . 50
4.3 Summary . . . 53

5 Temperature Induced On-Surface Ring-Opening Polymerization Reaction for the Synthesis of Nanoribbons: Strain Influence of Cycloparaphenylenes 55
5.1 Introduction . . . 55

5.2 Results and Discussion 58
5.2.1 (6)CPP - Overview 58
5.2.2 (8)CPP - Overview 60
5.2.3 (10)CPP - Overview 63
5.2.4 Probe Particle Model Simulations of (8)CPP and (10)CPP 65
5.2.5 Investigation of Intermediates and Products 67
5.2.6 Discussion 72
5.3 Summary 74

6 Conclusion and Outlook **75**

A Supplementary Information on Chapter 4 **79**

B Supplementary Information on Chapter 5 **95**

Bibliography **111**

Acknowledgements **127**

List of Publications **129**

1 Introduction

In the iconic "There's Plenty of Room at the Bottom" speech (1959) [1], Richard Feynman shared his vision "of manipulating and controlling things at the small scale", thereby capitalizing on the altered material properties that emerge upon dimension reduction when one "could arrange the atoms one by one". With his speech, he potentially initiated today's rapidly expanding research field of nanoscience- and technology. Upon analyzing nanostructures, one of the primary challenges identified was the insufficient resolution inherent in conventional microscopy techniques. A milestone towards realizing Feynman's conception was the invention of the scanning tunneling microscope (STM), introduced in 1982 by Binnig, Rohrer et al. [2, 3]. Compared to by then established microscopy methods, the STM uses a different approach: A sensitive sensor with a sharp measuring tip is brought to the close proximity of a surface, whereby variations in a recorded tunneling current serve as measurement variable. Even in its early stages, the method proved to be capable of imaging and manipulating matter on the atomic scale [4, 5, 6]. Based on the forces acting between sample and tip in the STM, a further breakthrough in the field of high-resolution microscopy was achieved merely four years later with the development of the atomic force microscope (AFM) [7, 8]. Since the sensed forces, which are used as measurement signal, act between all materials, the portfolio of possible samples to be investigated has been further extended to all non-conductive materials.

The first STM real-space observation of organic molecules, which can be regarded as atomic building blocks themselves, was conducted by Ohtani et al. in 1988 [9]. The pioneering work eventually led to the research field of self-assembly of organic molecules on atomically flat surfaces [10, 11]. Self-assembly processes involve complex, reversible arrangements of molecular precursors driven by intermolecular interactions. The resulting two-dimensional self-assembled structures exhibit interesting electronic properties, which designate them for the use in organic electronic devices [12]. In 2007, Grill et al. initiated the novel research field of on-surface synthesis (OSS), demonstrating that polymerization reactions of self-assembled molecular building blocks can be performed on metal surfaces in vacuum environments [13]. In contrast to self-assembled structures, a characteristic feature of OSS is the formation of covalent bonds between molecular building blocks. The newly created carbon nanostructures exhibit one-dimensional expansions, thereby providing a further step to Feynman's vision of dimension reductions resulting from atom by atom arrangements. The dimensional restriction of the molecules adsorbed on the substrate hinders the three-dimensional rotatability, whereby different products with the same precursors can be achieved, compared to conventional organic synthesis in liquid environments [14, 15]. The field of OSS gained substantial growth with the introduction of the chemical bond imaging method in 2009 by Gross et al. [16]. In this groundbreaking study, the lateral structure of an organic molecule was deciphered for the first time by passivating the otherwise reactive metal tip with an inert carbon monoxide molecule.

Thereby, another of Feynmans's early ideas, namely to analyze the structure of newly created chemical compounds by having a "look at it and see where the atoms are", was fulfilled. The first chemical reaction on a surface, showing a rearrangement and formation of covalent carbon-carbon bonds, was resolved by de Oteyza et al. in 2013 [17]. In recent years, OSS has led to the creation of various remarkable carbon nanostructures, which have been unequivocally identified using the chemical bond imaging method. These include, for example, benzenoid carbon nanoribbons [18, 19, 20], non-benzenoid carbon nanoribbons, including rings with an odd number of carbon atoms [21, 22, 23], patches of graphene nanoribbons, often referred to as nanographenes [14, 24, 25, 26, 27] and unique carbon model structures, which are, due to their high reactivity, inaccessible using conventional in-solution chemistry [28, 29, 30]. These low-dimensional quantum materials have in common that they feature different, unique electronic properties compared to their two- and three-dimensional counterparts [31]. Therefore, the semiconducting graphene nanostructures are candidates for the integration into nano-electronic devices [32, 33]. However, the electronic properties of these materials are highly sensitive to the local chemical structure, particularly considering the width of the ribbons [21, 34, 35]. Consequently, achieving a defect-free and precise synthesis that ensures the exact arrangement of the structure's atoms is essential for controlling their properties. Nonetheless, this turns out to be a major challenge, as many parameters play a role in the synthesis of such structures. These include, for example, the choice of the substrate, precursors and their functionalization as well as the manipulation methods (e.g. temperature, tip manipulation) [36, 37].

The versatile selection of precursors and surfaces results in an almost infinite number of possible combinations for creating new nanostructures, which again reinforces the title of Feynman's speech that "There's *Plenty* of Room at the Bottom". The motivation of the work presented here is to provide a small yet meaningful contribution to the expansive research field of self-assembly and on-surface synthesis. In Chapter 4, the self-assembly of unilaterally fluorinated 1,2,10,11,12,14-hexafluoropentacene is investigated on inert Au(111) and reactive Cu(111) substrates, to gain deeper insight into the intermolecular interaction of hydrogen and fluorine atoms. The interaction has proven to be a valuable tool in self-assembly processes prior to on-surface reactions, but is to date not sufficiently investigated. While the interaction of the molecules on the inert Au(111) substrate is predominantly steered by intermolecular interactions, the enhanced reactivity of Cu(111) results in distinct adsorption geometries and molecular arrangements. The subtle arising differences are visualized using the chemical bond imaging method, which provides access to bond lengths in the picometer range and angular variations of a few degrees.

In the second part of this work, the on-surface reaction of cycloparaphenylene precursors is investigated. Usually, one of the most widely used on-surface reaction mechanisms is the Ullmann coupling, which involves halogenated precursors. However, due to the complex interplay of the halogens and the surface, the exact outcome of the reaction is typically difficult to predict. The recently presented ring-opening polymerization of halogen-free (6)Cycloparaphenylene molecules has proven to be a valuable alternative to commonly used Ullmann coupling reactions. However, the effect of the ring-opening and the influence of the ring strain in cycloparaphenylene molecules is not comprehensively analyzed yet. The investigation of a set of different ring sizes (see Chapter 5) shows that the occurring ring-opening polymerization is facilitated for smaller cycloparaphenylenes with higher ring strain.

2 Theory

2.1 Scanning Probe Microscopy

Scanning probe microscopy (SPM) defines a group of various microscopy methods used to image and manipulate matter on surfaces on the molecular and atomic scale. Despite their diversity, all SPM methods work according to a very similar principle: A sensor with a sharp measuring tip is placed in the close proximity of a sample, whereby different sample properties can be determined depending on the SPM method. Notably, each SPM technique employs different types of sensors and tip materials, relying on distinct physical mechanisms to measure a surface's topography or to extract various physical properties of the sample. The scanning tip (or sample) is mounted to a scanner which consists of a piezoelectric material. Based on the inverse piezoelectric effect, the piezo scanner expands when a voltage is applied to the component, making it possible to precisely control the x-, y- and z-position of the tip [38]. In this thesis, the x- and y-direction refers to the plane that is parallel to the surface of the sample. The tip-sample separation along the z-direction is generally regulated by a feedback controller mechanism that maintains a constant interaction between the sensor and the sample during scanning [39, 40, 41]. The basic principle of the SPM measurement is shown in Figure 2.1.

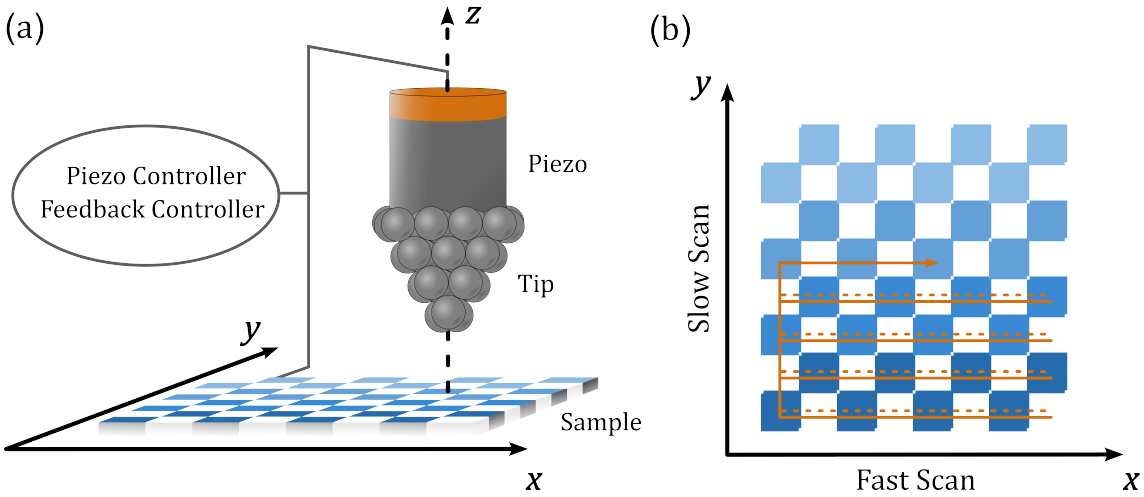


Figure 2.1: (a) Sketch illustrating the general principle of scanning probe microscopy with the main components [adapted by [39]]. (b) Illustration of the scanning path of the SPM tip during the measurement. Each blue and white tile represents one image pixel, the scanning path of the tip is represented by an orange arrow [adapted by [42]].

During imaging, the tip is scanned back and forth in a raster pattern (indicated by solid and dashed orange lines) while acquiring the respective surface properties in a line-by-line scan. Upon completing data acquisition in one line, the scan continues by moving to the next line. The recorded data can then be plotted in a two-dimensional (or three-dimensional) image. In Figure 2.1 (b), the pixels are displayed as white and blue tiles, each tile representing one pixel. Compared to scanning in a single line in x-direction, the defined scanning path of the tip results in a longer data acquisition time in y-direction. Therefore, the x- and y-axis are often denoted as fast scan axis and slow scan axis, respectively [40, 42]. Measurements along the slow scan axis are more susceptible to image artifacts, such as thermal drift and piezoelectric creep. Thermal drift refers to the gradual change in the system's measurements due to temperature variations, while piezoelectric creep occurs due to a non-linear expansion of the scanner when applying a voltage to the piezoelectric component [41, 43]. An overview of the manifold SPM methods to characterize various surface properties is given in Ref. [44]. In the scope of this thesis, two of the most popular scanning probe microscopy methods, the scanning tunneling microscopy and the atomic force microscopy, were utilized. Details on the methods are given in Sections 2.2 and 2.3.

2.2 Scanning Tunneling Microscopy

The groundbreaking scanning tunneling microscopy (STM) was introduced by Binnig, Rohrer et al. in 1982 [2, 45]. Merely four years later, the inventors were honored with the Nobel Prize in physics for their pioneering work [46]. The STM measurement is based on a simple, but effective measuring principle. A sharp metallic tip is scanned very closely (usually 0.3 - 1.0 nm [47, 48]) over an atomically flat, electronically conductive surface. The tip is attached to a piezoelectric actuator, enabling it to move freely in all three spatial directions (x-, y- and z-directions). When the tip is scanned in the close vicinity of the sample and a gap voltage V_g (usually 0.002 - 2.0 V [49, 50]) is applied, a detectable current flows between the tip and sample [2, 3].

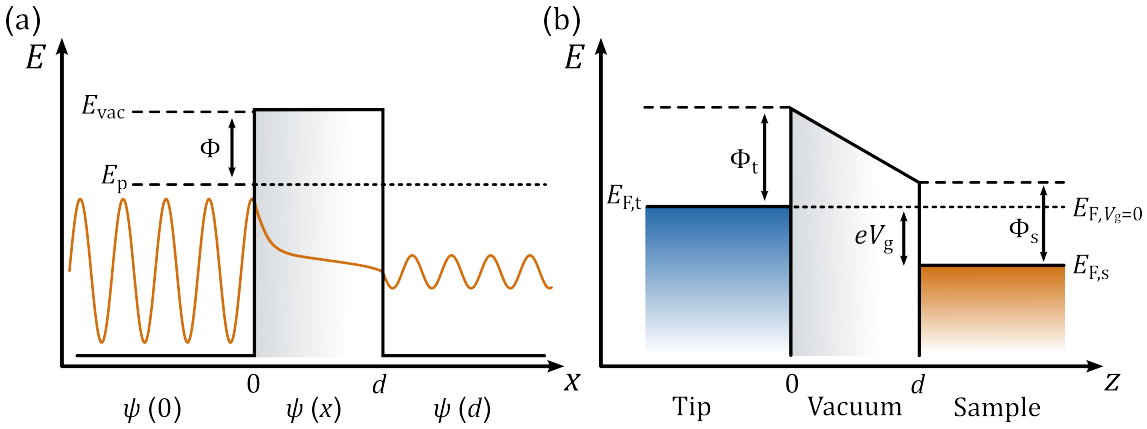


Figure 2.2: (a) Sketch of a particle tunneling through a one-dimensional vacuum barrier [adapted by [51, 52]]. (b) Energy level diagram of a tunneling junction in STM [adapted by [39, 53]].

The current I_t detected during the scanning process, despite the absence of physical contact between the tip and sample, arises from the quantum mechanical tunnel effect. This tunneling process can be explained in a simplified one-dimensional model using two solids with a vacuum gap between them. The vacuum gap can be modeled as a square-shaped potential barrier, as shown in Figure 2.2 (a). In classical mechanics, an incoming particle with a particle energy E_p would be fully reflected at the barrier if the vacuum energy E_{vac} is higher than the energy of the incoming particle $E_{vac} > E_p$. In quantum mechanics however, electrons in solids have a wave character and can be described by a wave function $\psi(r)$. To solve the Schrödinger equation inside the square-shaped potential, an ansatz with an exponentially decaying wave can be used: $\psi(x) = \psi(0)e^{-\kappa x}$. The approximate probability $|\psi(x)|^2$ (Equation 2.1 [52]) of finding a particle inside the barrier is

$$|\psi(x)|^2 = |\psi(0)|^2 \, e^{-2\kappa x}, \quad \kappa = \sqrt{\frac{2m_e\Phi}{\hbar^2}}, \tag{2.1}$$

with the electron mass m_e, the reduced Planck constant $\hbar$ and the work function Φ. The

latter represents the minimum energy required to release an electron from the solid. On the left and right side of the barrier, the electrons can be described by the wave function of free electrons [54]. Overall, there is a high probability to find an electron on the left side of the barrier ($x < 0$), whereas the probability of finding a particle inside the barrier ($0 < x < d$) decays exponentially. However, if the barrier width d is smaller than the penetration depth of the particles, they can tunnel through the potential barrier. Thus, on the right side of the barrier ($x > d$) there will be a small, but finite probability to find an electron [55]. The ratio of the probabilities of finding a particle on the left $|\psi(0)|^2$ or right side $|\psi(d)|^2$ of the barrier can be expressed by the transmission coefficient T (Equation 2.2 [52]):

$$T = \frac{|\psi(d)|^2}{|\psi(0)|^2} \approx e^{-2\kappa d}. \tag{2.2}$$

Two essential properties of the STM can already be derived from this simplified model: The tunneling current $I_\mathrm{t} \propto \exp(-2\kappa d)$ [50, 56] shows an exponential dependency and increases with decreasing gap size d and decreasing work function Φ of the analyzed sample.

For the STM experiment, the simplified tunneling representation in Figure 2.2 (a) can be conceptualized as a vacuum barrier that separates the tip and sample (with work functions Φ_t and Φ_s) at a distance z, as shown in Figure 2.2 (b). In absence of a gap voltage V_g, the Fermi energies of the tip $E_\mathrm{F,t}$ and sample $E_\mathrm{F,s}$ equal each other (indicated by a dashed line, $E_{\mathrm{F},V_\mathrm{g}=0}$) and no current will flow. When a gap voltage V_g is applied between tip and sample, the respective Fermi levels $E_\mathrm{F,t}$ and $E_\mathrm{F,s}$ will be shifted relative to each other by an energy eV_g ($e =$ elementary charge) and the square-shaped barrier will be transformed into a trapezoidal barrier. Consequently, electrons can tunnel from occupied states in one electrode to unoccupied states in the other electrode (in case of Figure 2.2 (b) from tip to sample), which results in a tunneling current I_t [39, 49, 57]. Electrons in electronic levels with energy states between $E_{\mathrm{F},V_\mathrm{g}=0} + eV_\mathrm{g}$ can contribute to the tunneling current during the measurement [48].

The exponential relationship between the tunneling current and the tip-sample distance makes the STM a highly sensitive measuring device. For example, a change in distance of one angstrom leads to a change of approximately one order of magnitude in the detected tunneling current [50, 58]. Notably, the sharpness of the tip plays an important role in the sensitivity and resolution of the measurement. For sharp tips, ending in a single or few metallic atoms, the tunneling effect is concentrated in a very small area, making it possible to resolve surfaces with atomic resolution, as initially demonstrated by Binnig et al. in 1982 on a Si(111)-7×7 surface [4]. The ultra-high precision of the STM could, for example, further be demonstrated by the positioning and manipulation of single atomic structures on a surface, as shown by Eigler, Schweizer and Stroscio [6, 59].

In STM imaging, the height of the tip is usually adjusted via a feedback loop to maintain a steady current. When the tip encounters an unevenness, such as an adatom or a step edge, it is lifted up to keep the defined current constant. The changes in tip height can be recorded, resulting in a height map. However, even though the image interpretation in

STM seems to be straightforward at first glance, in some cases it can be rather difficult, as exemplified in the following. When analyzing the measurement data, it is crucial to consider that the height determined by STM does not represent the actual physical sample height, but rather the z-displacement of the piezo element as a function of the measured tunneling current. Since the tunneling current is dependent on the work function of the investigated material, regions with a lower work function will appear higher in the STM image [2, 3]. In a theoretical STM model by Tersoff and Hamann, it was demonstrated that the tunneling current is proportional to the surface's local density of states (LDOS) at tip position. Thus, the STM image can be interpreted as a map of constant LDOS of the surface around the Fermi level [60, 61]. As a consequence, a change in polarity of the applied voltage can result in different STM image contrasts, because either filled (negative bias) or empty (positive bias) states are mapped [48, 62]. Due to the aforementioned properties, certain species adsorbed on the substrate, such as i.e. carbon monoxide (CO) molecules, can appear as dark dots in the STM image (meaning "lower" relative to the surface) [63].

2.2.1 Constant Current and Constant Height Mode

While the prototype of the STM was operated in constant current mode (cc-mode) [2], STM measurements can also be performed in constant height mode (ch-mode). A comparison of both modes is sketched in Figure 2.3.

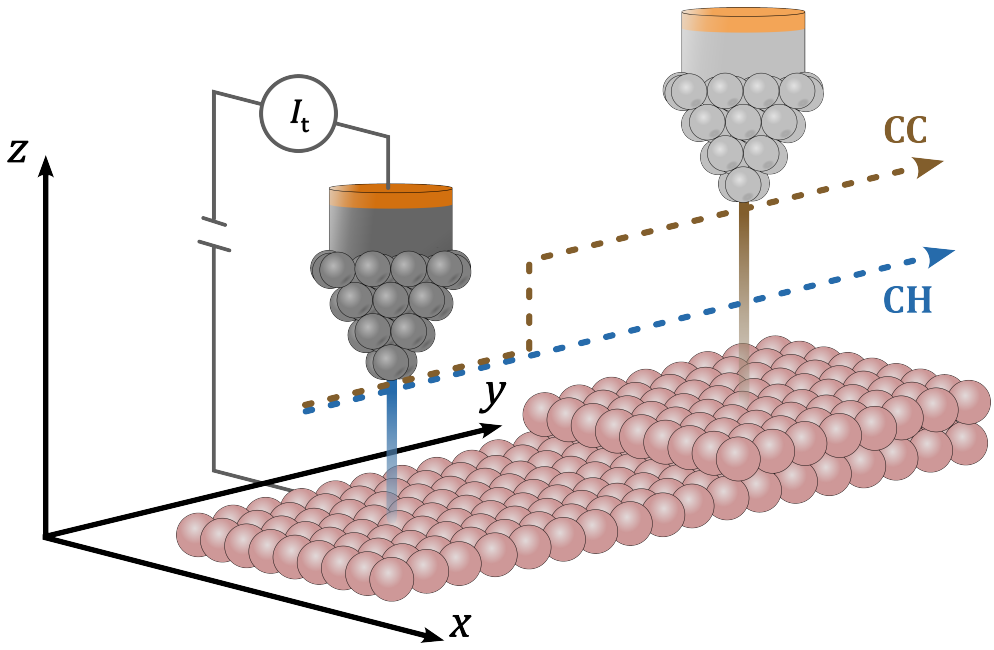


Figure 2.3: Comparison of the constant current and constant height mode in STM. When encountering an obstacle, the tip in cc-mode (light-colored tip) will follow the brown line, whereas in ch-mode (dark-colored tip) it will follow the blue line [adapted by [50]].

In the more common cc-mode, the tip is scanned over the surface, while a feedback loop adjusts the tip height z in such a way that the monitored current during scanning is kept constant. Consequently, when the tip in cc-mode encounters an obstacle, it will be lifted up to adjust the current to the current setpoint. As shown in Figure 2.3, the tip (light-colored tip) will follow the brown line. Tip height adjustments are done by applying a voltage to the piezo tube [47, 64]. Thus, the cc-STM image shows a plot of the tip height z at the x- and y-positions [50, 64]. Due to the height adjustment, the cc-mode is safe to use on rough surfaces which are not atomically flat [50, 53]. As a consequence, also large scan areas can be imaged safely. However, the response time of the feedback loop to adjust the height results in rather low scan speeds and data acquisition rates [64].

When the feedback loop is omitted, measurements can also be performed in constant height mode. In ch-mode, the tip is scanned over the surface at nearly constant height and voltage (see blue line and dark-colored tip in Figure 2.3). While scanning, the current I_t is recorded, resulting in an I_t versus x- and y-position STM image [50, 64]. Due to the absence of a feedback loop, measurement data can be recorded more quickly, making it possible to investigate dynamic surface processes on the atomic scale [53, 64, 65]. Because of the higher scan speeds compared to the cc-mode, image artifacts like piezoelectric creep, thermal noise and mechanical vibrations can be reduced [50, 64]. The major drawback of the ch-mode is that tip damage can occur if the investigated surface is not atomically flat [53, 64]. Moreover, as there is no direct access to the height data, it needs to be extracted from the current data [64]. The concept of ch- and cc-measurements was explained here using the STM as an example. However, it can also be applied to other scanning probe microscopy methods. Depending on the measurement method, these can also be carried out in ch-mode or with respect to the specific feedback parameter that is controlled in the selected mode [40].

In the framework of this thesis, the constant current STM mode proves to be an indispensable analysis method, as it allows to image large scan areas in a reasonable amount of time while maintaining a stable tip. Consequently, adsorption positions of molecules on the surface can be determined in order to follow and resolve self-assembly processes step-by-step. Furthermore, molecules can be localized before and after self-assembly processes and chemical reactions. Reaction products can be further investigated using the chemical bond imaging method. For more details see Section 2.3.3 and 2.3.4.

Already in the early days of their measurements with the STM, Binnig and Rohrer noticed that significant forces act between tip and sample [45]. These forces are fundamental for another high-resolution microscopy method, the atomic force microscopy, which was introduced by Binnig, Quate and Gerber in 1986. Prior to the explanation of the working principle of the atomic force microscope, it is worth having a look at the numerous forces acting between tip and sample (Section 2.3.1).

2.3 Atomic Force Microscopy

2.3.1 Forces Between Tip and Sample

In scanning probe microscopy, a variety of different long-range and short-range forces act between the tip and sample. In a simplified approach, the tip-sample interaction can be modeled by the so-called Lennard-Jones potential $V_{\mathrm{LJ}}(r)$ (LJP). The LJP describes the interaction of uncharged single atoms or small molecules as they approach each other at a distance r. It consists of two main interaction components, a repulsive ($\propto r^{-12}$) and an attractive part ($\propto r^{-6}$):

$$V_{\mathrm{LJ}}(r) = V_0 \left[\left(\frac{\sigma}{r}\right)^{12} - \left(\frac{\sigma}{r}\right)^{6} \right]. \tag{2.3}$$

In Equation 2.3 [66, 67], V_0 describes the depth of the potential well and σ denotes the distance between the atoms where $V_{\mathrm{LJ}}(r)$ is zero [68]. The potential curve of the Lennard-Jones potential as a function of the distance r is represented in Figure 2.4 by a gray dashed line. The respective attractive and repulsive components are shown as dashed orange and blue lines.

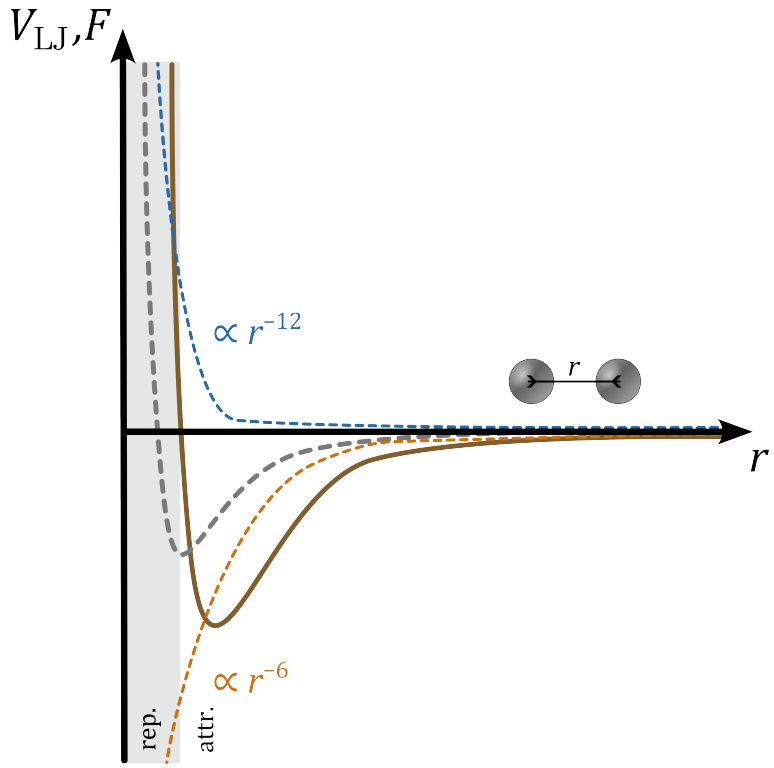


Figure 2.4: Lennard-Jones potential (gray, dashed) and its attractive (orange, dashed) as well as repulsive (blue, dashed) components. The resulting force is shown as solid brown line. The transition from the attractive to the repulsive force regime is highlighted by a gray box [adapted by [67, 69]].

The force F (Equation 2.4 [67]) acting between the two atoms at a distance r is given by

$$F = -\frac{\partial V_{\mathrm{LJ}}(r)}{\partial r}, \tag{2.4}$$

and is shown as solid brown line. At large distances r, no force acts between the two atoms. As the distance decreases, the interaction is dominated by an attractive (negative) force. When the distance between the atoms is reduced even further, the attractive force converts into a repulsive (positive) force. The initially negative course of the force curve passes through a minimum and the strong, repulsive force dominates the interaction between the atoms. The transition from the attractive to repulsive force regime is indicated by a gray box. The forces contributing to the LJP are mainly van der Waals dipole interactions (attractive) and Pauli repulsion (repulsive) and will be explained in the following [70].

Van der Waals Force

The van der Waals force describes the various interactions of all induced and permanent dipoles. A dipole is a system of two opposing charges q, which are spatially separated from each other at a distance l. The associated dipole moment $\vec{p} = q \cdot l$ is a vector that points from the positive to the negative charge and indicates the orientation and strength of the dipole [71]. In total, three different dipole-dipole interactions contribute to the van der Waals force, namely the Keesom, Debeye and London dispersion interactions [72]. The Keesom interaction describes the attraction between two permanent dipoles, whereas the Debeye interaction is the attraction between a permanent and an induced dipole [73]. The London dispersion interaction is the main contribution to the van der Waals force and acts between all molecules or atoms. London forces arise as a result of a transient fluctuation in the charge distribution within atoms. This can temporarily induce a dipole, generating an electric field that subsequently induces polarization and dipole formation in a nearby atom. Consequently, the resulting interaction between the two dipoles results in an attractive force [66, 74]. However, the previous description only applies to individual atoms or dipoles. Owing to the long-range nature of van der Waals forces, which exhibit an inverse sixth-power dependence, these forces act not only among individual atoms but collectively between many atoms in the sample and tip in an AFM experiment [75]. Moreover, these forces depend on the geometry of the interacting bodies. In case of the tip and sample, the van der Waals force is often modeled using a spherical body with radius R interacting with a flat surface. The van der Waals force F_{vdw} between the two bodies is described in Equation 2.5 [66]:

$$F_{\mathrm{vdw}} = -\frac{A_{\mathrm{H}} R}{6 z^2}, \tag{2.5}$$

where z describes the distance between the two bodies and A_{H} the Hamaker constant which contains, e.g. the number of atoms per interacting unit volume.

Pauli Repulsion

The strong repulsive force, which acts in areas of very small atomic distances ($\propto r^{-12}$) is the so-called Pauli repulsion. In the range of very small atomic distances, the wave functions of the approaching atoms overlap. Since electrons are fermions with half-integer spin, they cannot occupy the same quantum state due to the Pauli exclusion principle. Consequently, when two fully filled orbitals overlap, the electrons of approaching atoms must transition to unoccupied states of higher energy. This leads to an increase in the total energy of the system and results in a repulsive force that is strongly dependent on the distance [69, 76].

Electrostatic Forces

Electrostatic forces arise between charged or conductive tips and samples when a potential difference, in case of the STM experiment a gap voltage V_g, is applied. For a spherical tip with radius R and tip-sample distances z smaller than the tip radius, the electrostatic force can be written as Equation 2.6 [77]:

$$F_\mathrm{el}(z) = -\frac{\pi\epsilon_0 R V_\mathrm{g}^2}{z}, \tag{2.6}$$

with the dielectric constant ϵ_0. The electrostatic force can be classified as a long-range force. However, with a distance dependence of z^{-1}, compared to the van der Waals force, the electrostatic force acts in an even longer range [78, 79]. Usually, when performing AFM measurements, the gap voltage between the tip and sample is set to zero or a value close to zero to compensate the electrostatic forces, as also done for the AFM measurements in this thesis.

Capillary Forces, Adhesion

Two more notable forces are capillary and adhesion forces. Capillary forces arise when water molecules are adsorbed on the sample and tip. The van der Waals force between the water molecules leads to the formation of a meniscus, which results in an attractive force between the tip and sample [41]. Adhesion forces arise when the tip and sample are in physical contact and comprise various contributions, including van der Waals interactions, electrostatic forces, hydrogen bonds, capillary forces and chemical bonding forces. Generally, it represents the force required to separate the sample from the tip upon contact [72]. However, since the SPM measurements performed in this thesis are carried out exclusively under ultra-high vacuum (UHV) conditions and in non-contact modes, capillary forces and adhesion might be largely neglected.

2.3.2 General Working Principle of Atomic Force Microscopy

In 1986, just four years after the introduction of the STM, Binnig, Quate and Gerber presented another high-resolution SPM method, the atomic force microscopy (AFM). While the working principle is not fundamentally different from the STM, the key distinction of the method lies in the use of the acting forces as measurement signal, which also makes it suitable for analyzing insulating samples [7]. Although all measurements performed in this thesis were carried out in an advanced AFM mode, the frequency modulation AFM mode (see Section 2.3.3), for a general understanding it is worth having a look at basic principles of atomic force microscopy.

The setup of the AFM measurement is presented in Figure 2.5. In AFM, a cantilever with a sharp tip is scanned over a flat sample surface. The forces that are acting on the tip lead to a displacement of the cantilever and can be used as feedback signal. For instance, in the prototype of the AFM, the tip was scanned in direct contact over the sample, while a feedback loop was used to maintain a constant force between the tip and sample. The deflection of the cantilever was monitored through variations in the tunneling current of a STM tip positioned in the close proximity of the cantilever [7, 8]. In nowadays applications, the deflection of the cantilever is typically measured using the optical beam deflection method, which employs a laser and a position sensitive detector, as introduced by Meyer and Amer [80]. This is exemplified in Figure 2.5 by a laser beam that is reflected by the backside of a cantilever and directed onto a photodiode using a mirror.

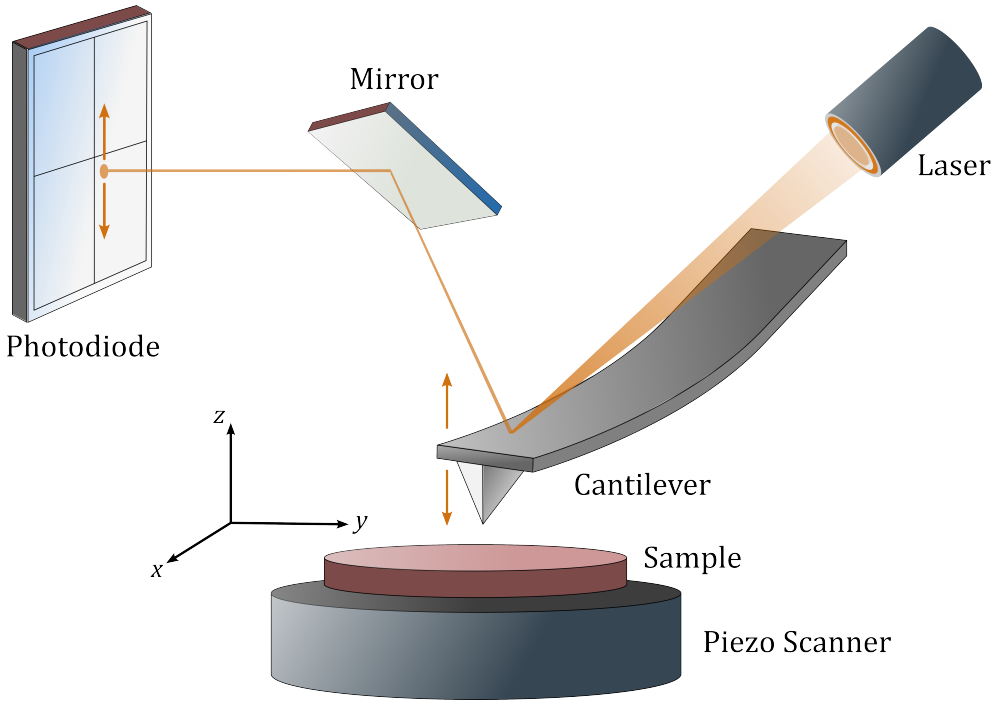


Figure 2.5: Sketch of the general setup of atomic force microscopy. A sharp tip is scanned over a flat sample that is attached to a piezo scanner. The displacements of the cantilever are measured using a laser and a photodiode [adapted by [81]].

Overall, AFM experiments can be conducted in two different operation modes, the static mode (non-oscillating cantilever) and the dynamic mode (oscillating cantilever). In the static mode, the non-oscillating cantilever acts as a spring with the spring constant k. According to Hooke's law (Equation 2.7 [71]), the force F acting on a spring is, in the elastic regime, proportional to its displacement Δz:

$$F = -k \cdot \Delta z. \tag{2.7}$$

The acting force between the tip and sample leads to a deflection of the cantilever. During the measurement, a feedback loop attempts to keep the deflection of the cantilever constant, which corresponds to maintaining a constant force. When a displacement of the cantilever is present, the height is adjusted by means of a piezo scanner to maintain a constant deflection, whereby the adjusted height corresponds to the surface topography. Generally, the static mode can be operated in either the attractive or repulsive regime of the force-distance curve (see Figure 2.4). When operated in the repulsive regime, this mode is also known as contact mode AFM [82].

In dynamic mode, the cantilever is externally driven into oscillation, acting as a damped harmonic oscillator. One of the main operation modes in dynamic AFM is the so-called amplitude modulation (AM) mode, which is based on initial measurements with oscillating cantilevers by Martin et al. [83]. In AM mode, the cantilever is excited with a fixed amplitude and driving frequency ω_d close to its resonance frequency ω_0. Upon tip-sample interaction, the resonance frequency of the oscillator changes, resulting in changes in the amplitude and phase of the oscillation signal relative to the excitation signal. The feedback loop adjusts the tip-sample distance in such a way that a constant amplitude is maintained, leading to a topographic image of the sample surface [84]. Please note that this is an abbreviated introduction of the dynamic mode, for further information refer to Section 2.3.3.

The properties of the cantilevers used in the experiment are of great importance in AFM measurements. The resonance frequency $\omega_0 = (k/m_0)^{\frac{1}{2}}$ of the spring depends on its spring constant and effective mass m_0. To obtain a high deflection for a given force F, soft cantilevers with small spring constants are required [7]. A necessary condition to ensure stability during the measurement is that the negative force gradient of the tip-sample interaction $-\partial F_\mathrm{ts}/\partial z$ does not overcome the restoring force of the cantilever. Otherwise, the tip will jump to the surface, which is often referred to as snap-to-contact [81]. Therefore, in general, a trade-off is required between a cantilever with sufficient stiffness to ensure stable measurement conditions and adequate sensitivity.

While the prototype of the AFM was operated in air [7], AFM measurements can, depending on their respective application, also be performed in liquid environments [85, 86] as well as under UHV conditions [87, 88]. A critical parameter that describes the properties of an oscillating system, which is influenced by the environment in that the oscillator is driven, is the so-called quality factor (Q factor). The Q factor is a dimensionless variable that expresses after how many oscillation cycles the amplitude of a damped oscillating system decays to 1/e of its initial amplitude without external excitation. It is inversely

proportional to the external environmental damping γ of the system: $Q = m_0\omega_0\gamma^{-1}$ [81]. As a result, large Q factors are achieved in less damped vacuum environments (order of several 10 000) [89], whereas Q factors in air are only a few 100 and in highly damped environments, such as liquids, an order of magnitude lower [81, 90]. The Q factor is of great importance for the sensitivity of the AFM measurement, as it affects the smallest detectable force gradient, which can be described by the following Equation 2.8 [91]:

$$\frac{\partial F}{\partial z}|_{\min} = \sqrt{\frac{4k \cdot k_{\mathrm{B}}T \cdot B}{\omega Q \langle z_{\mathrm{osc}}^2 \rangle}}, \tag{2.8}$$

where T is the temperature, B the bandwidth of the measurement, $\langle z_{\mathrm{osc}}^2 \rangle$ the mean square oscillation amplitude, k_{B} the Boltzmann constant and ω the angular frequency of the free cantilever. Consequently, high Q factors are advantageous for detecting small force gradients and achieving high measurement sensitivities. Therefore, in terms of measurement sensitivity, it is beneficial to conduct AFM experiments under UHV conditions. However, the Q factor also influences the transient time $\tau = 2Q/\omega_0$ of the oscillating system, which describes the time needed for the amplitude to decrease to 1/e of its original value without excitation [81]. Upon tip-sample interaction, the cantilever's changes in resonance frequency lead to changes in amplitude and phase. Since in AM mode, a steady-state amplitude is required to reliably record data, the same period must be waited to record a new data point. For Q factors of several 10 000 in vacuum applications, this leads to unreasonably long measurement times [84, 92]. Since the self-assembly studies and on-surface reactions investigated in this thesis require UHV conditions to ensure clean and adsorbate free surfaces, the AM mode is not suited to be used. A strategy to avoid the long transient times is the use of the frequency modulation AFM mode, which is further described in Section 2.3.3.

2.3.3 Frequency Modulation Atomic Force Microscopy

In 1991, Albrecht et al. introduced the so-called frequency modulation (FM) mode, using the recorded frequency as feedback parameter. In FM mode, the cantilever is externally excited at its exact resonance frequency. In contrast to the amplitude response, the frequency response reacts instantaneously to a change in the tip-sample interaction. Therefore, the long acquisition times are avoided, even when operating sensors with high Q factors in vacuum environments [93]. In the dynamic mode, the tip acts as a driven, damped harmonic oscillator. When the equation of motion is solved for the same, the following well-known expression for the oscillation amplitude A_{osc} (Equation 2.9 [94]) of the oscillator is obtained:

$$A_{\mathrm{osc}}^2 = \frac{A_{\mathrm{d}}^2}{\left(1 - \frac{\omega_{\mathrm{d}}^2}{\omega_0^2}\right)^2 + \frac{1}{Q^2}\frac{\omega_{\mathrm{d}}^2}{\omega_0^2}}. \tag{2.9}$$

Here, ω_0 describes the resonance frequency of the oscillator, ω_{d} the driving frequency and A_{d} the driving amplitude. Further, the resulting phase shift φ between the input and output signal can be written as (Equation 2.10 [94]):

$$\varphi = \arctan \frac{-\frac{\omega_{\mathrm{d}}}{\omega_0}}{Q\left[1 - \left(\frac{\omega_{\mathrm{d}}}{\omega_0}\right)^2\right]}. \tag{2.10}$$

The corresponding amplitude and phase responses of the driven harmonic oscillator with damping are shown as black curves in Figure 2.6 as a function of the driving frequency.

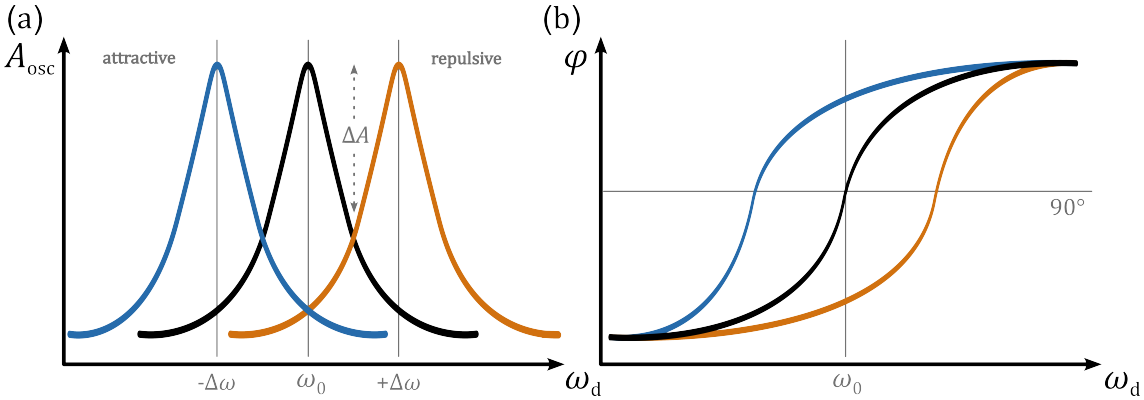


Figure 2.6: (a) Amplitude response as a function of the driving frequency for a driven, damped harmonic oscillator [adapted by [93]]. (b) Resulting phase response [adapted by [81]]. Black curves show the amplitude and phase curves of the undisturbed oscillation, whereas colored curves are shifted upon tip-sample interaction.

When an additional force gradient acts on the tip during interaction with the sample, the resonance frequency ω_0 of the cantilever shifts. In addition to the spring constant k of the sensor, the interaction of tip and sample can be modeled by a second spring with spring constant k_{ts}. Assuming that the force gradient between sample and tip is constant in the entire interaction range [79], the resulting frequency shift upon tip-sample interaction can be described using the following Equation 2.11 [84, 91]:

$$\Delta\omega = \omega_0 \frac{k_{\mathrm{ts}}}{2k} = -\frac{\omega_0}{2k}\frac{\partial F_{\mathrm{ts}}}{\partial z}. \tag{2.11}$$

Attractive forces (positive force gradient, $\partial F_{\mathrm{ts}}/\partial z > 0$) shift the amplitude and phase curves along the frequency axis towards lower frequencies (blue curves), whereas repulsive forces (negative force gradient, $\partial F_{\mathrm{ts}}/\partial z < 0$) shift them towards higher frequencies (orange curves) [84]. The resulting frequency shifts are used as a measurement signal in FM mode and lead (in constant height mode) to a frequency shift map (see Figure 2.7 (c)). When the resonance curves shift along the frequency axis, the oscillation amplitude consequently changes by ΔA (see gray arrow in Figure 2.6 (a)) [92]. To ensure stable measurement conditions, the amplitude is always kept constant via a feedback loop [81]. Since the phase curves are also shifting upon tip-sample interaction (see Figure 2.6 (b)), a second feedback loop is required to keep a steady excitation of the cantilever at its resonance frequency. The resonance condition is thereby fulfilled when the cantilever is oscillated with a phase shift of 90 ° [81]. Technically, this is often realized using a phase-locked loop (PLL), which employs a feedback loop to compare the phase of the cantilever oscillation with a reference signal. The PLL keeps the phase locked by feeding back the measured phase difference to maintain the phase at its reference value [95].

Due to the use of two feedback loops, the FM mode is technically more difficult to perform than the AM mode. Nevertheless, because of the long acquisition times in AM mode, the FM mode is the state-of-the-art method for AFM measurements in dynamic mode in vacuum as well as for performing the so-called chemical bond imaging method. The chemical bond imaging method, which makes it possible to reveal the molecular structure of organic species, is introduced in Section 2.3.4.

2.3.4 Chemical Bond Imaging

While STM and conventional AFM measurements made it possible to image the surfaces to be investigated with atomic resolution at an early stage [4, 8, 88, 96], the lateral structure of molecular compounds remained unresolved for an extended period. As described in Section 2.2, the tunneling current in STM is a function of the local density of states at tip position [60, 61]. As a result, molecules that are resolved using STM do not show the appearance of a molecular wireframe structure, but often appear inflated in STM images (see Figure 2.7 (b)), which makes it difficult to assign an exact structure to the STM image of a molecule [97]. However, attempting to resolve the structure of molecules in dynamic AFM mode using metallic AFM tips presents challenges due to the high reactivity of the tips. As a consequence, molecules adsorbed on the surface are either displaced or picked up by the tip [16]. In 1997, Bartels et al. demonstrated that a functionalization of the metallic tip apex with a single CO molecule results in significantly increased STM image contrasts. Further, the appearance of CO molecules adsorbed on a Cu(111) surface changed from a dark crater to a dark crater with a centered dot [63, 98]. Although the measurements were already interpreted as an enhancement in chemical sensitivity of the STM measurements, the chemical structure of organic compounds had not yet been deciphered at that time. In 2009, Gross et al. achieved a milestone in visualizing the lateral chemical structure of an organic pentacene molecule for the first time, using the same functionalization of the metal tip by means of a single inert CO molecule [16]. The basic principle of this method, often referred to as chemical bond imaging, is shown in Figure 2.7.

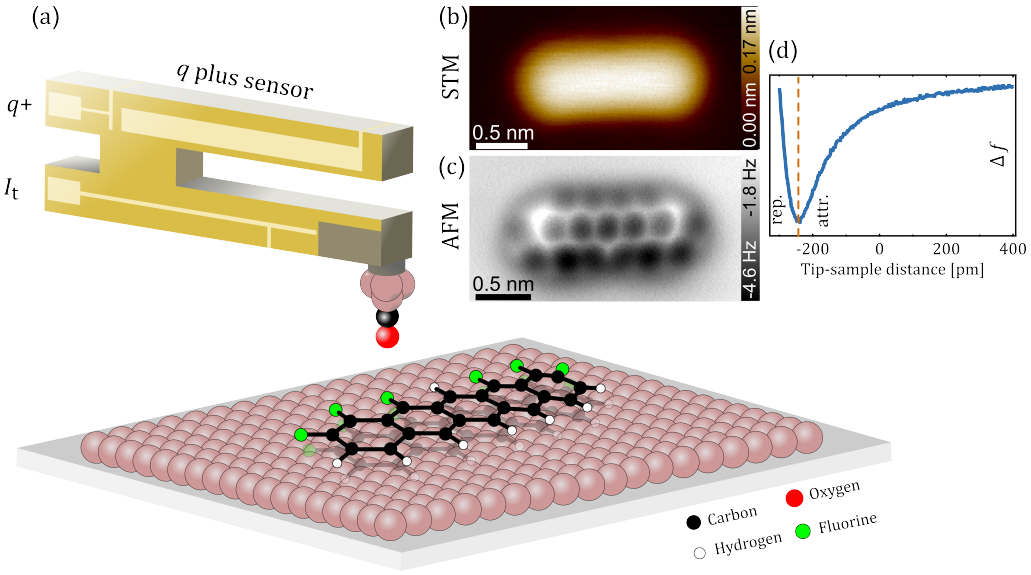


Figure 2.7: (a) General setup of the chemical bond imaging method [adapted by [99]]. A F_6PEN molecule is placed on an atomically flat sample, while a q plus sensor with CO-functionalized tip is used to obtain (b) STM images and (c) bond resolved frequency shift images of the molecule. (d) Experimental frequency shift vs. tip-sample distance curve, taken over the center of the F_6PEN molecule with a CO tip.

In the chemical bond imaging method, the molecules are investigated on atomically flat substrates, as exemplified for a 1,2,10,11,12,14-hexafluoropentacene (F_6PEN) molecule in Figure 2.7 (a). The cantilevers sketched in Figure 2.5, which are usually used in conventional AFM measurements, are replaced by the so-called q plus sensor, introduced by Giessibl in 1998 [100]. The core of the sensor consists of a quartz tuning fork with two prongs, which is usually used in wristwatches. One prong is attached to a mount, while the other prong is able to oscillate freely with a tip chemically etched to it (usually tungsten or platinum/iridium). With its high spring constant of typically about $1800\,\mathrm{N\,m^{-1}}$, it allows stable operation at high forces, avoids snap-to-contact and offers sub-piconewton sensitivity. Owing to the piezoelectricity of the quartz sensor, the deflection is read out electronically (q^+). Further, the tunneling current (I_t) can be recorded simultaneously, which enables combined STM and AFM measurements. Therefore, the optical detection via a laser and a photodiode, as used in the AFM experiment performed with cantilevers (see Figure 2.5), is no longer required [100, 101]. In order to ensure stable measurement environments and adsorbate-free substrates, the chemical bond imaging method is usually performed in UHV environments and at cryogenic temperatures of approximately 5 K (liquid helium (He)). The UHV environments minimize sample contamination, while low temperatures ensure stable measurements, suppress molecular diffusion and reduce drift as well as thermal noise [99, 102]. Figure 2.7 (b) shows a STM image of a F_6PEN molecule. In the STM image, the molecule's shape does not correspond to the actual molecular structure, but appears as a straight bar with rounded corners, precluding any conclusions about its chemical structure. Consequently, to resolve the chemical structure of the molecule, AFM measurements need to be performed. To avoid the lateral manipulation of the molecule under investigation, it is necessary to passivate the reactive metal tip with an inert CO tip and create a well-defined, single atomic tip apex [16, 102]. Due to the UHV environment, the AFM measurements are usually carried out in FM AFM mode (see Section 2.3.3). The frequency shift is imaged pixel-by-pixel, leading to a frequency shift map with the resolved molecular structure of the F_6PEN molecule, as shown in Figure 2.7 (c).

Figure 2.7 (d) shows an experimentally obtained frequency shift Δf curve as a function of the tip-sample distance, which was recorded with a CO tip over the center of a F_6PEN molecule. The transition from the attractive to the repulsive regime is highlighted by an orange dashed line. As already shown in the original bond imaging publication of Gross et al., the chemical bond contrast becomes more prominent when decreasing the tip height while measuring, meaning entering further into the repulsive regime. These findings were corroborated in a computational study by Moll et al., concluding that the Pauli repulsion is the primary source of the molecular resolution, whereas electrostatic and van der Waals forces contribute only an indistinct, featureless background [103]. Consequently, to obtain sub-molecular resolution, the chemical bond imaging method needs to be conducted in the repulsive regime of the curve shown in Figure 2.7 (d). Thereby, smaller tip-sample distances will lead to increased frequency shifts, resulting in brighter contrasts. The measurements are usually performed with small amplitudes in the range of several tens of picometers [104, 105], since the contribution of short-range forces increases with decreasing amplitudes [106, 107]. As the frequency noise is proportional to the inverse of the amplitude [79], a trade-off must be found between achieving good image contrast and low signal-to-noise ratio.

The chemical bond imaging method can technically be performed in constant height as well as constant frequency shift mode. However, due to the non-monotonic dependence of the frequency shift as a function of interatomic forces, the method is usually performed in constant height mode [99, 102]. A significant drawback of measuring in constant height mode is the exponential increase of the frequency shift at small tip-sample distances (see Figure 2.7 (d)). This results in a limited range of a few hundred picometers over which chemical bond contrast can be achieved before instabilities arise [16, 108]. Therefore, the chemical bond imaging method is mainly suited for resolving planar adsorbed molecular structures. For bulky and non-planar structures whose height exceeds the repulsive interaction range of sample and tip, often only a portion of the molecule can be resolved, making it difficult to interpret the experimental results without the aid of theoretical calculations [14, 109, 110]. An improvement in the method was presented by Martin-Jimenez et al. with the introduction of the constant current AFM mode. In this mode the structure of a molecule is resolved while simultaneously enabling the tunneling feedback. Due to the enabled tunneling feedback, the tip follows the contour of the molecular species, resulting in smaller tip-sample distances. This makes it possible to resolve a larger portion of strongly adsorbed molecules [104].

Upon interpreting image features of frequency shift AFM images taken of molecules with CO-functionalized tips, it needs to be emphasized that the CO molecule is able to bend horizontally at the apex of the metal tip. Particularly at close tip-sample distances, the bending can lead to bond sharpening and image artifacts, which could be misinterpreted as e.g. intermolecular bonds. Therefore, care must be taken when interpreting experimental AFM images recorded with CO tips, especially when operating at small tip-sample distances. These findings are based on a theoretical AFM model introduced by Hapala et al., the so-called probe particle model [108]. This model is used in the course of this thesis to simulate theoretical AFM images in order to interpret experimental data (see Chapter 5). At this point, it is also noteworthy that molecular resolution of organic compounds can be achieved using a row of different tip functionalizations, such as bromine (Br), chlorine (Cl) [111] and xenon (Xe) [111, 112]. However, to date, the CO tip is the state-of-the-art tip functionalization for performing the chemical bond imaging method.

The introduction of the chemical bond imaging method by Gross et al. expanded the possibilities for investigations of molecules on surfaces in the already versatile field of SPM applications. These include, for example, the structure elucidation of undetermined organic species [113, 114], bond order discrimination [115], tip induced single molecule manipulation [28, 29, 30, 105], the investigation of single molecule reactions [17, 105, 116], assigning the absolute configuration of chiral compounds [110] as well as the identification of adsorption geometries of molecules [117, 118, 119]. The two most relevant subareas addressed in this thesis, which are frequently analyzed by chemical bond imaging, are the self-assembly mechanism of organic molecules on surfaces and the on-surface synthesis of carbon nanostructures via single molecule chemical reactions. These are explained further in Section 2.4 and 2.5. The SPM methods described so far are used for the experiments in the herein presented work. In general, large image areas are captured using the cc-STM mode (see Section 2.2.1) to localize organic species on the surface. For molecular resolution of organic structures, the chemical bond imaging method described in this section is applied in FM mode (see Section 2.3.3). Planar adsorbed molecules are imaged in ch-mode, while the cc-AFM mode is used to analyze bulky structures.

2.4 On-Surface Self-Assembly Processes of Organic Molecules

Self-assembly is an universal term employed across interdisciplinary research fields such as biology, on-surface chemistry and nanotechnology. It refers to the spontaneous formation of ordered nanostructures due to the reversible, typically non-covalent intermolecular interactions between atomic and molecular species [120, 121, 122]. In the field of on-surface chemistry on metal substrates, self-assembled monolayers of organic molecules gained, among others, a lot of attention through the investigation of thiols on gold surfaces [123, 124]. Nowadays applications are, for example, focused on the use of tailored, functionalized organic building blocks to control self-assembly mechanisms for the creation of bottom-up fabricated, customized materials for the integration into organic electronic devices [125]. The device performance is mainly determined by the charge carrier mobility in organic thin films, which in turn depends on the overlap of the π-orbitals of the organic molecules and thus on their orientation [12]. In case of the on-surface synthesis of carbon nanostructures in a bottom-up reaction mechanism, self-assembly processes of the precursors in the sub-monolayer regime can mark the pre-step of on-surface reactions [13, 21, 126, 127, 128] and can even determine which product is created at a local level with the same precursors [21, 129, 130, 131]. Therefore, upon predicting the outcome of an on-surface reaction, a profound knowledge of the molecular on-surface alignment is required. However, self-assembly processes of organic molecules on metal substrates are usually difficult to anticipate, since they are governed by the complex interplay of intermolecular and molecule-substrate interactions [10]. The process of molecular on-surface self-assembly is exemplified for a functionalized carbon backbone on a metal surface in Figure 2.8.

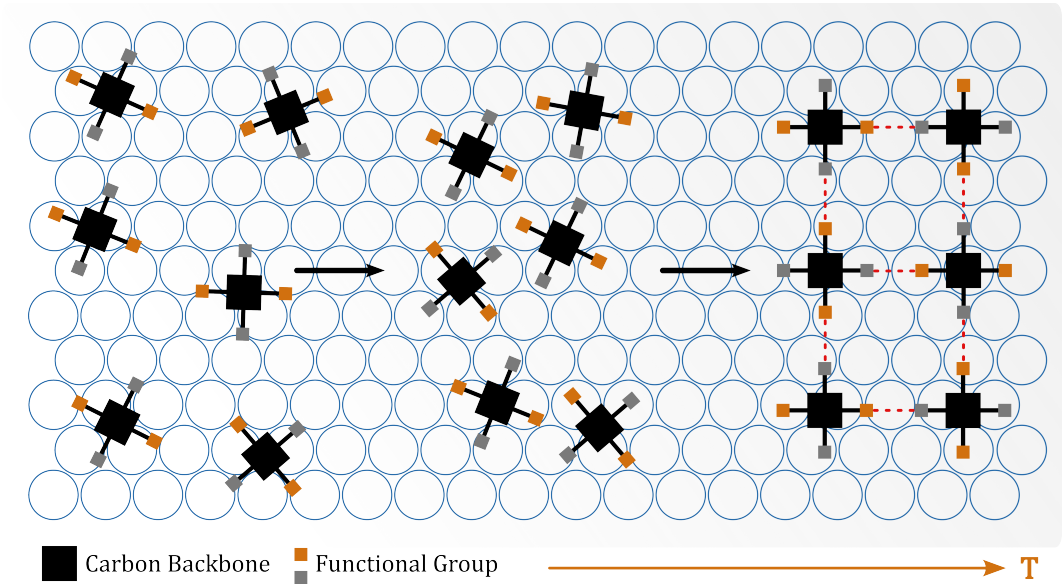


Figure 2.8: Sketch of the thermally induced self-assembly process of organic molecules on a metal surface [adapted by [11]].

The molecules to be investigated are usually evaporated onto a cold substrate (in the case of the experiments in this thesis approximately 7 K) and bind to the surface with the

binding energy E_b. To facilitate surface diffusion and transition into a thermodynamically favored equilibrium state, the sample can be (subsequently) annealed. During annealing, thermal energy is transferred to the molecules. The resulting kinetic energy E_{kin} enables them to overcome the diffusion barrier E_d on the substrate. A necessary condition for the stable adsorption of the molecules on the surface, before and after the self-assembly process, is that the kinetic energy E_{kin} does not exceed the binding energy E_b of the molecules to the substrate. Otherwise, the molecules will desorb from the surface. The self-assembly process is influenced by the various intermolecular interactions E_{inter} between the molecules (exemplified as dashed red lines in the ordered structure in Figure 2.8), such as van der Waals forces, hydrogen bonding and electrostatic forces [11, 132]. In case of the self-assembly process prior to on-surface reactions, often the halogen bonding between halogenated precursors plays a major role. The halogen bond is introduced in Section 2.4.1.

Due to the complex interplay of the investigated molecules and the substrate, self-assembly processes and the outcome of on-surface reactions are usually difficult to predict. Therefore, experimental studies are required to decipher self-assembly mechanisms. For example, previous studies have shown that self-assembly processes are dependent on the molecule coverage on the surface [133, 134, 135] as well as on the substrate that is used. Even in case of simple, linear pentacene molecules, different orderings, lattice parameters and adsorption structures are observed on commonly used Au(111), Ag(111) and Cu(111) coinage metal surfaces [135, 136, 137]. Moreover, the molecule-substrate interaction can vary across different surface regions on the same sample [138, 139]. Also, the molecule functionalization, such as e.g. substitution of hydrogen with fluorine atoms, has a major impact on the molecular alignments [140, 141, 142].

Initially, the study of self-assembly processes on surfaces was limited to spectroscopic and diffraction methods, which do not provide real-space resolution of organic species. Therefore, the invention of the STM revolutionized the investigation of molecular self-assembly processes in the monolayer and sub-monolayer range. Soon after the introduction of the STM, its inventors demonstrated that small inorganic molecular species, such as oxygen, can be resolved using this technique [5]. The first real-space image of an organic molecule on a surface was presented by Ohtani et al., investigating the superlattice of benzene molecules formed on a rhodium surface [9]. Since then, the STM emerged to one of the state-of-the-art tools to follow on-surface self-assembly processes of organic molecules, providing studies of various organic species on many different surfaces [10, 11, 133, 134, 135, 138, 140, 143, 144]. However, due to lack of lateral molecular resolution when performing STM measurements (see Sections 2.2 and 2.3.4), a significant drawback of investigating self-assembly processes using STM is that the exact molecular arrangements, such as bonding angles and distances of single atoms, are not experimentally accessible. The invention of the chemical bond imaging method has enabled even more precise investigations of molecular self-assembly processes by revealing the molecular structures and local bond arrangements of neighboring self-assembled molecules. This allows to determine the bonding patterns in the range of a few picometers and degrees [109, 118, 145, 146, 147].

2.4.1 The Halogen Bond in On-Surface Self-Assembly Processes

A valuable tool for steering self-assembly processes on surfaces is the interaction of halogens attached to carbon backbones. The term halogen bonding describes the non-covalent interaction between a halogen atom and an electron-rich, nucleophilic species. It was defined by the IUPAC in 2013 as follows: "A halogen bond occurs when there is evidence of a net attractive interaction between an electrophilic region associated with a halogen atom in a molecular entity and a nucleophilic region in another, or the same, molecular entity" [148]. This definition initially may seem to be counterintuitive when considering the simple bond-line formula of a Halogen X, which forms a covalent bond to another atom R (e.g. carbon), as depicted in Figure 2.9 (a). Since halogens, because of their high electronegativity, are typically regarded as centers of high electron density, they would be assigned a negative charge in this simple representation. Therefore, in case of Figure 2.9 (a), the two halogen atoms would repel each other due to an occurring repulsive force. To gain a deeper understanding of the halogen bond's nature, it is essential to closely examine the charge distribution within the covalent bond of the halogen atom. When a halogen forms a covalent bond to another atom, the charge density is not localized in the center of the two atoms, but slightly shifts towards the overlapping orbitals of the covalent bond. This leads to an anisotropic charge distribution within the halogen, resulting in a negatively charged electron belt oriented perpendicular to the covalent bond. Consequently, a region of lower electron density forms at the outer cap of the halogen. This region, the so-called σ-hole, can engage in attractive interactions with electron-rich, nucleophilic sites [149, 150].

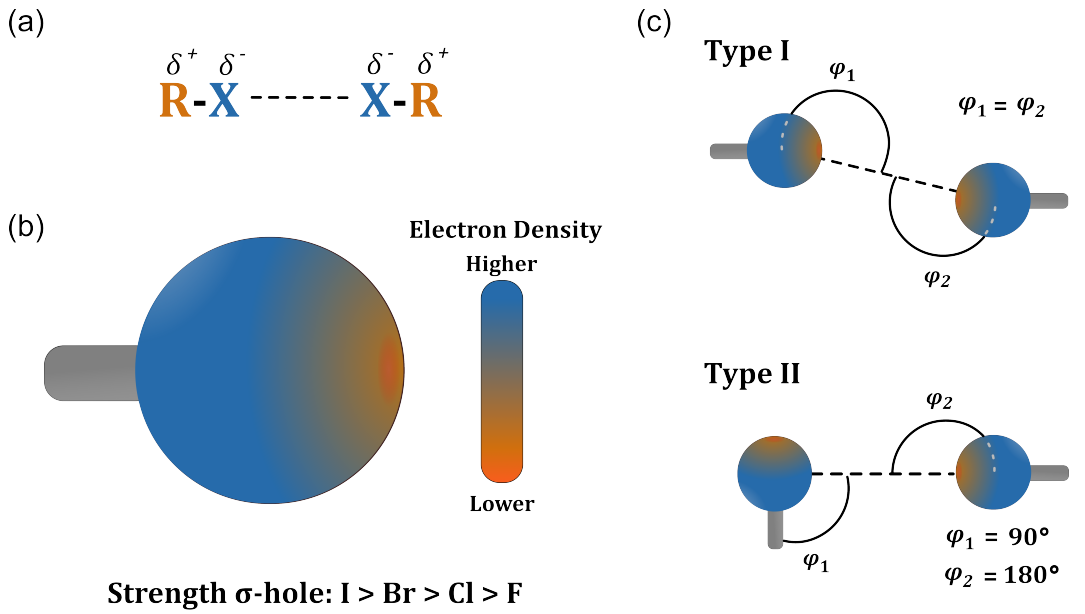


Figure 2.9: (a) Bond-line formula of a halogen X forming a covalent bond to another species R. (b) Representation of the σ-hole. High electron densities are depicted in blue, whereas lower ones are shown in orange. (c) Sketch of the two most common types of halogen bonding patterns involving two halogens. Type I: $\varphi_1 = \varphi_2$. Type II: $\varphi_1 = 90\,^\circ$ and $\varphi_2 = 180\,^\circ$ [adapted by [149, 151]].

A halogen atom with σ-hole is sketched in a simplified representation in Figure 2.9 (b). The halogen atom is schematically represented as a sphere, with a belt of higher electron density orthogonal to the covalent bond (blue). The σ-hole, characterized by its positively charged cap exhibiting lower electron density, is depicted in orange. In general, the strength of the σ-hole is influenced by the polarizability of the halogen, thus increasing for larger halogens with lower electronegativities (strength σ-hole: I > Br > Cl > F). However, due to the high electronegativity and low polarizability of the fluorine atom, resulting in a strong localization of the electrons around the atom, the σ-hole for the fluorine atom is usually neutralized [151, 152]. Therefore, a σ-hole for fluorine can only be observed in certain cases, for example in environments with very strongly electron-withdrawing substituents [153, 154]. The halogen bond is further characterized by the relative arrangement of two or more halogens. Among the various bonding patterns that can arise, the two most relevant types in which two halogens interact with each other are shown in Figure 2.9 (c). The upper sketch illustrates the type I halogen bond, where the atoms are arranged such that the angles relative to the covalent bond R-X and non-covalent halogen bond equal each other ($\varphi_1 = \varphi_2$). In contrast, in the type II arrangement (lower sketch), the σ-hole of one halogen is oriented perpendicular to the negative belt of the other halogen. This results in bond angles of $\varphi_1 = 90\,^\circ$ and $\varphi_2 = 180\,^\circ$, respectively [149, 150].

Due to the position of the σ-hole along the extension of the covalent bond, the halogen bond is considered a directional bond. Given that the strength of the σ-hole can be tuned, for example, by varying the type of halogens and other substituents involved, it serves as a valuable tool for controlling self-assembly processes [149]. Therefore, the halogen bond is often used to influence self-assembly processes prior to the molecules on-surface reactions. However, other difficulties can arise when using halogenated precursors, such as complex interactions of the halogenated molecules with the substrate and interactions of the precursors with cleaved halogen atoms. This is further discussed in Section 2.5.1.

As already mentioned, the σ-hole in fluorine atoms is usually neutralized. This might also be the case for the 1,2,10,11,12,14-hexafluoropentacene molecule investigated in Chapter 4, since the fluorine atoms in the molecule are only surrounded by non-strongly electron withdrawing compounds such as carbon and hydrogen atoms. It is important to highlight that in the examined system, intermolecular hydrogen-fluorine interactions are being studied. Accordingly, this interaction does not qualify as a halogen bond, since, by definition, a halogen bond requires the interplay of an electron-deficient (electrophilic) site of a halogen and a nucleophilic site of another atom. However, in case of the hydrogen-fluorine interaction, a positively charged hydrogen atom interacts with a negatively charged halogen. Therefore, this type of interaction is accurately classified as a hydrogen bond [149]. For comparison, the bond configurations shown in Figure 2.9 (c) are nevertheless used to describe the arrangement of the hydrogen and fluorine atoms in the self-assembly process of 1,2,10,11,12,14-hexafluoropentacene molecules and are denoted as quasi-type I and quasi-type II halogen bonds. The hydrogen-fluorine interactions, which are useful to steer self-assembly processes prior to the molecules on-surface reactions, are investigated in detail in Chapter 4 with the chemical bond imaging method, using 1,2,10,11,12,14-hexafluoropentacene molecules as a model system.

2.5 On-Surface Synthesis

In general, organic synthesis involves the chemical reactions of precursors that are primarily composed of carbon, hydrogen and other elements such as oxygen, nitrogen, sulfur, phosphorus as well as halogens to construct complex molecules. Its origins trace back to the beginning of the 19th century, whereas over two centuries of research have enabled the creation of a diverse array of compounds that are integral to various aspects of daily life, including drug manufacturing as well as materials and polymer science [155, 156]. Compared to conventional organic synthesis, which is commonly performed in liquid environments, the reaction of molecules performed on atomically flat substrates in vacuum, the so-called on-surface synthesis (OSS), is a novel field of research that can only draw on a few years of research experience to date. While the first organic molecule reactions on surfaces were reported around the turn of the millennium [157, 158, 159, 160], a milestone in the foundation of this new field of research was laid by Grill et al. in 2007. In this pioneering study, it was demonstrated that polymerization reactions and the formation of covalent bonds between molecular building blocks can be performed directly on the substrate at a larger scale [13].

Much like the impact of the chemical bond imaging method on the field of on-surface self-assembly processes of organic molecules, the introduction of this technique has significantly advanced the research in on-surface synthesis. For the first time, chemical reactions and the formation of covalent bonds could be followed step-by-step with sub-molecular resolution, as initially demonstrated by de Oteyza et al. [17]. Due to the loss of the rotational freedom of the precursors on a two-dimensional, flat surface, the same precursor can lead to different products in on-surface and conventional in-solution synthesis [14, 15]. The two-dimensional constraint has enabled direct access to various types of carbon nanostructures on surfaces. This includes several types of graphene patches, known as nanographenes [14, 24, 25, 26, 27], benzenoid carbon nanoribbons [19, 20, 161, 162] as well as non-alternant carbon allotropes which, in addition to six-membered carbon rings, also contain rings with an odd number of carbon atoms in their structure [21, 22, 23]. Further, some unique carbon structures could be synthesized under UHV conditions on surfaces, which are usually inaccessible due to their high reactivity [28, 29, 30]. The carbon nanostructures synthesized directly on a surface show a number of distinct electronic properties, which make them promising candidates for their integration into organic electronic devices [32, 33]. For example, the band-gap of graphene nanoribbons can be tuned as a function of their width [15, 21, 34, 35], which is why the controlled synthesis of nanostructures of defined widths is desired.

In recent years, several systematic reaction mechanisms have been established in the on-surface synthesis to form new carbon-carbon bonds between the involved precursors. These include, for example, the surface-supported cyclodehydrogenation reaction [14, 25, 26, 163, 164], Glaser coupling [165, 166, 167] and a large number of further on-surface reactions, which are reviewed in the following articles: [36, 37]. One of the most frequently used on-surface reactions is the dehalogenative Ullmann coupling reaction, which will be, due to the relevance in this thesis, explained separately in Section 2.5.1.

2.5.1 On-Surface Ullmann Coupling

The Ullmann coupling is a reaction mechanism in organic chemistry used to form covalent carbon-carbon bonds between halogenated organic species. The method was pioneered by the chemist Fritz Ullmann, who annealed halogenated benzene compounds in the presence of copper powder as a catalyst, yielding biphenyls as a product [168]. Decades later, it was demonstrated by Xi et al. that a similar reaction takes place on a copper surface. Compared to copper powder, the surface on which the molecules are adsorbed acts as the catalyst itself in this reaction [157]. The on-surface Ullmann reaction is exemplified in Figure 2.10 by means of two halogenated benzene molecules on a metal surface and was precisely deciphered by Zint et al. using the chemical bond imaging method [116].

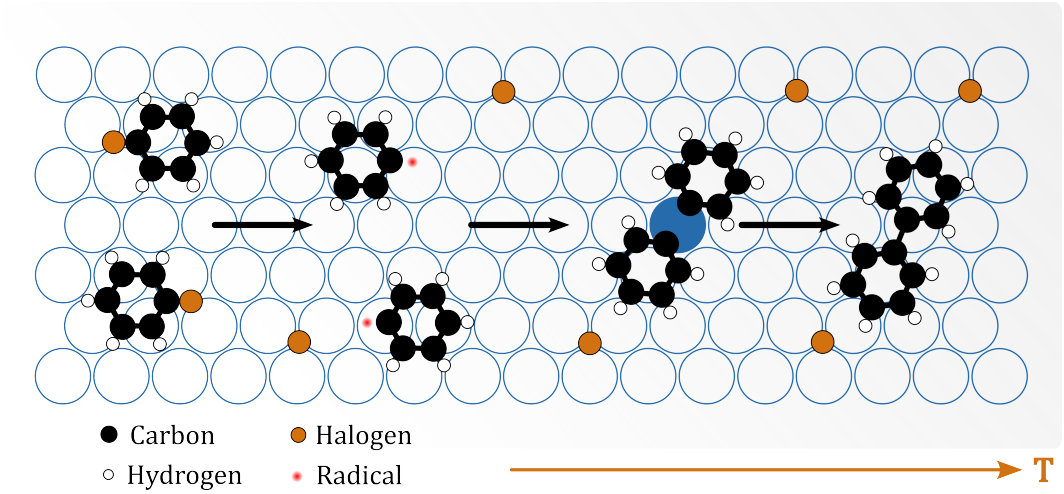


Figure 2.10: On-surface Ullmann coupling reaction of halogenated benzene molecules on a metal substrate, resulting in the formation of a biphenyl molecule [adapted by [116, 157]].

Upon annealing, the first reaction step is the dehalogenation of the benzene molecules, leading to a formation of phenyl radicals. The radicals are represented as red circles in Figure 2.10. On reactive substrates such as Cu(111), an organometallic intermediate state is typically observed, where the radicals bind to a surface adatom. This is indicated by a filled, blue atom. In the final reaction step, a covalent carbon-carbon bond is formed, resulting in the formation of a biphenyl molecule in the example of Figure 2.10.

Nowadays, the on-surface Ullmann reaction is one of the most widely employed methods for synthesizing carbon nanostructures on surfaces, resulting in a diverse array of structures [13, 19, 22, 25, 27, 35, 161, 162, 169, 170, 171, 172, 173]. However, when applying an Ullmann-type reaction step in an OSS routine, the self-assembly process of the molecules is mostly governed by halogen bonds. As explained in Section 2.4.1, the halogen bond is a directional bond that can be tuned due to the varying strength of the σ-hole as well as the carbon backbone and other functional groups. Therefore, it should be beneficial to tweak self-assembly processes of precursors. Though, it was shown in comprehensive experimental and computational studies of halogen bonds on surfaces by Tschakert et al. [118] and Henkel et al. [174] that the strength of the σ-hole is influenced by the surface on

which the halogenated molecules are adsorbed. For example, the interaction of iodine and bromine with the copper surface results in a more pronounced weakening of the σ-hole in the case of polarizable iodine. Hence, bromine-bromine bonds are favored on a reactive Cu(111) surface over iodine-iodine bonds, even though iodine has the stronger σ-hole in the gas phase and should therefore be preferred [151, 152]. Consequently, self-assembly processes and on-surface reactions of halogenated molecules are usually difficult to predict. For instance, due to different dehalogenation temperatures, the type of halogen functionalization can have an influence on the product of the OSS. Thus, a sequential occurrence of subsequent reaction steps for a precursor with lower dehalogenation temperatures can lead to increased lengths of graphene nanoribbons [175]. Additionally, the same halogenated precursors can yield different products depending on the surface on which the OSS is performed [176, 177]. For example, a frequently used 10,10'-dibromo-9,9'-bianthryl (DBBA) molecule for synthesizing graphene nanoribbons leads to three different products on Au(111) [161], Cu(111) [97, 171] and Cu(110) [172]. Further, the same precursor can result in different products on the same surface [21, 131, 173].

An intermediate that is frequently used to synthesize graphene nanoribbons in on-surface reactions are poly(*para*-phenylene) chains, consisting of phenyl rings connected in para-position. However, when these chains are synthesized using a halogenated precursor, the cleaved halogen atoms might inhibit the chain arrangement and chain growth. Further, the self-assembly mechanism of the halogenated precursors on different surfaces is difficult to predict. The problem can be circumvented by using halogen-free cycloparaphenylene molecules as initial precursors. This topic is further investigated and discussed in the results section in Chapter 5.

3 Experimental

3.1 Instrumentation

All STM and AFM measurements in this thesis were performed with a low temperature (LT) STM/AFM (*Scienta Omicron*, LT STM Lab, Germany). A sketch of the setup is shown in Figure 3.1.

The system consists of two stainless steel UHV chambers, the preparation and SPM chamber. Both chambers are equipped with ion pumps (*Gamma Vacuum*, USA), achieving base pressures during operation of $5{\cdot}10^{-11}$ mbar in both chambers. The chambers are separated by a plate valve (1). Samples can be moved between both chambers using a manipulator (2). A sample holder at the end of the manipulator with a heating and cooling position (3) is used to prepare the samples prior to experiments. Samples can be transferred into and out of the system by a load-lock (4). Carbon monoxide (*Westfalen AG*, Germany) (5) and argon (Ar) (*Nippon Gases*, Japan) (6) bottles are connected to the preparation chamber through a leak valve (7). Upon sample cleaning and CO dosing, while floating the preparation chamber with CO or Ar, the chamber is pumped by a turbo pump (*Pfeiffer Vacuum*, Germany) (8), which is connected to the chamber via another plate valve. This setup maintains a constant CO and Ar pressure, which is regulated by the leak valve. In order to operate the turbo pump, clean the Ar and CO pipes and evacuate the manipulator, a pre-pump (*Kashiyama, Neodry 15E*, Japan) (9) is required. Samples are cleaned by ion sputtering, using a sputter gun connected to the preparation chamber (*Prevac*, Poland) (10). For more information on the cleaning process see Section 3.2.1.

The SPM chamber is equipped with two rotatable sample carousels (11), which offer space for a total of 12 samples. Using a wobble stick (12), the samples can be moved between the manipulator, the sample carousels and the microscope (13). The scanner is attached to a liquid helium bath cryostat (14) to maintain a stable operation temperature of approximately 5.2 K. Molecules can be directly evaporated onto the cold sample within the scanner using a molecule evaporator (*Kentax*, Germany) (15). For more information see Section 3.2.2. The entire system is supported by three passive low-frequency vibration isolators (*minus k technology*, USA) to minimize mechanical background noise.

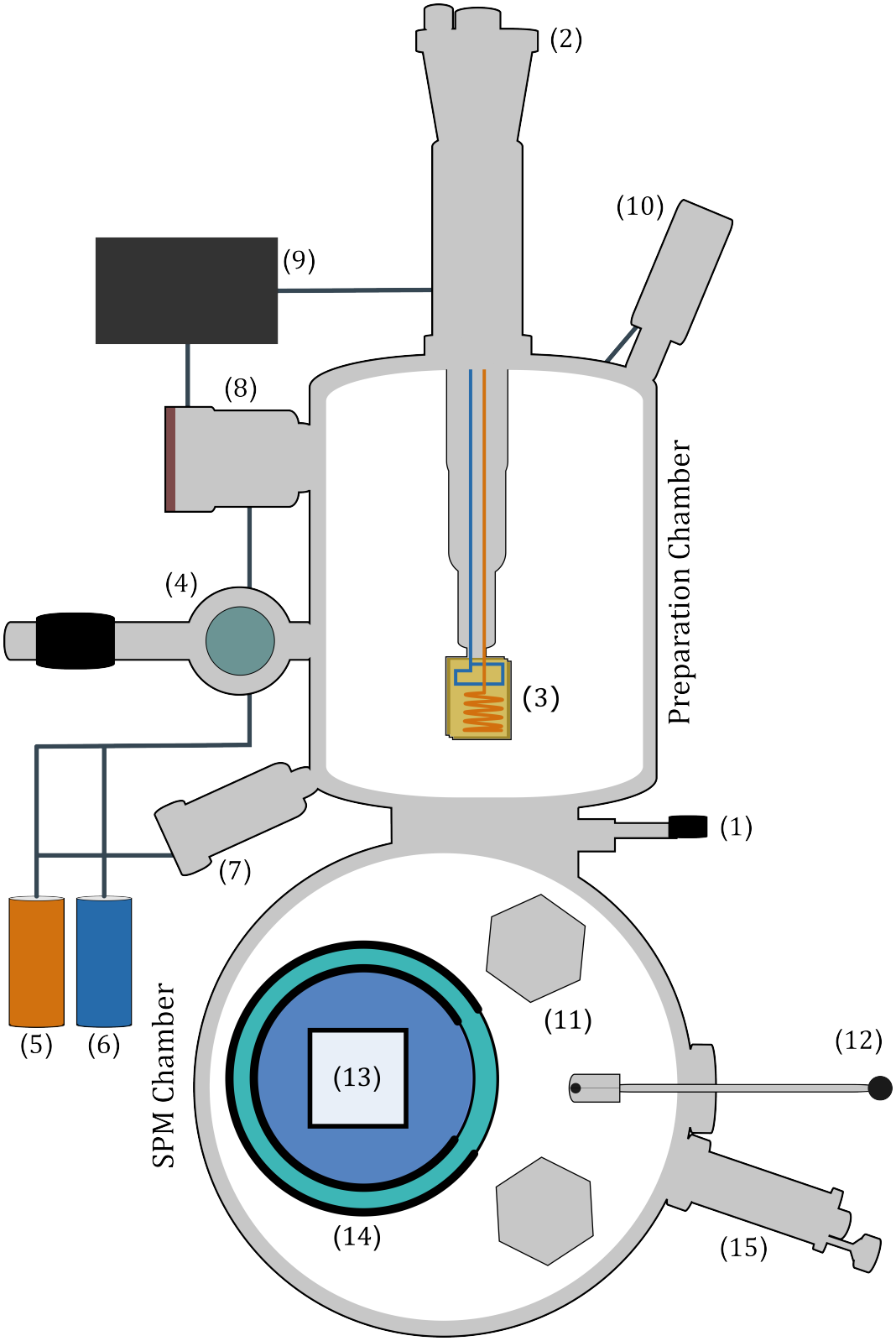


Figure 3.1: Sketch of the LT scanning probe microscope setup used for the experiments in this thesis.

3.2 Sample Preparation

3.2.1 Crystal Cleaning

Investigations of adsorbed molecules on metal surfaces using scanning probe microscopy techniques require atomically flat, highly pure and defect-free metal substrates. Substrate contamination can result in undesired side effects, such as contamination of the tip by adsorbates, which may alter the image contrast and make it impossible to resolve molecular structures using the chemical bond imaging method. Furthermore, the self-assembly process of the molecules can be disturbed by the interactions with contaminants and lead to unwanted side reactions in the on-surface reactions of molecular precursors. To achieve the substrate conditions necessary for the experiments, high-purity Au(111) and Cu(111) single crystals (*MaTeck*, Germany, purity: 99.999 %) were cleaned in the preparation chamber using a sputtering and annealing routine prior to each experiment. Details of the cleaning procedure are listed in Table 3.1 and 3.2, respectively.

Table 3.1: Parameters for the sputter and annealing routine used to clean the Au(111) single crystal.

Time [min]	**Description**	$p_{\mathbf{Ar}}$ **[mbar]**	$E_{\mathbf{ion}}$ **[kV]**	$I_{\mathbf{em}}$ **[mA]**	$T_{\mathbf{s}}$ **[°C]**
30	Sputtering only	$6 \cdot 10^{-6}$	1.5	10	25
20	Sput. + Annealing	$6 \cdot 10^{-6}$	1.5	10	760
10	Sput. + Annealing	$3 \cdot 10^{-6}$	1.5	10	640
5	Sput. + Annealing	$3 \cdot 10^{-6}$	0.8	10	460

Table 3.2: Parameters for the sputter and annealing routine used to clean the Cu(111) single crystal.

Time [min]	**Description**	$p_{\mathbf{Ar}}$ **[mbar]**	$E_{\mathbf{ion}}$ **[kV]**	$I_{\mathbf{em}}$ **[mA]**	$T_{\mathbf{s}}$ **[°C]**
30	Sputtering only	$6 \cdot 10^{-6}$	1.5	10	25
30	Sput. + Annealing	$6 \cdot 10^{-6}$	1.5	10	760
5	Sput. + Annealing	$3 \cdot 10^{-6}$	0.8	10	660

Ion sputtering was performed with Ar^+ ions at argon pressures p_{Ar} in an order of magnitude of 10^{-6} mbar. E_{ion} denotes the ion energy, I_{em} the emission current of the Ar^+ ions accelerated towards the sample and T_s indicates the sample temperature.

3.2.2 Molecule Evaporation

Molecule evaporation onto the substrate was performed by a physical vapor deposition (PVD) process with a commercial molecule evaporator (*Kentax GmbH*, Germany). The molecule evaporator is connected to the SPM chamber through a plate valve. For deposition, the plate valve was opened and the evaporator was moved into the measurement chamber. After the deposition, the evaporator was retracted and the plate valve was closed.

The molecules to be investigated were filled into a quartz crucible and placed inside the molecule evaporator. Prior to the first deposition, the entire evaporator was evacuated and pumped overnight. To determine the evaporation temperature, the crucible was heated in steps of 10 K, starting at 303 K. After reaching the target temperature, the temperature was kept constant for 12 minutes to ensure an uniform temperature inside the crucible. On completion of each evaporation cycle (usually for a period of 2 - 5 minutes), the surface coverage of the sample was inspected using STM. Once molecules were observed on the surface, the crucible was degassed for several hours at a temperature 20 K below the deposition temperature to remove contaminants. After the sublimation temperature of the molecules was determined, the sample was cleaned again and molecules were evaporated onto a pristine sample.

3.2.3 Tip Preparation and Characterization

CO was dosed for 5 - 10 minutes at pressures of about $1{\cdot}10^{-9}$ mbar onto the cold sample surface ($\approx$ 7 K) inside the SPM chamber. The tip was sharpened by applying voltage pulses in the range of -10 - 10 V and tip indentations to -10 nm. Frequency shifts were recorded using a phase-locked loop (*Zurich Instruments*, Switzerland), whereby frequency shifts of less than -1.5 Hz have proven to be a good value for picking up a CO molecule from the surface.

3.3 Experimental Details on Chapter 4

The tip was grounded, all bias voltages mentioned refer to the sample bias voltage. AFM images were acquired in constant height and constant current mode and were performed in frequency modulation mode using an external phase-locked loop (*Zurich Instruments*, Switzerland). During AFM imaging, a small gap voltage of $V_g = -0.57\,\text{mV}$ was applied to compensate for internal offsets of the current amplifier. All STM and AFM measurements were performed at cryogenic temperatures of 5.2 K.

F_6PEN on Au(111)

F_6PEN molecules were evaporated for 5 minutes at $\approx 493\,\text{K}$ directly onto the cold Au(111) sample surface ($\approx 7\,\text{K}$) inside the SPM chamber. Sensor parameters: Resonance frequency $\omega_0 \approx 25.88\,\text{kHz}$, quality factor Q $\approx$ 15 - 25 k, oscillation amplitude $A_{\text{osc}} = 400\,\mu\text{V}$ corresponding to $\approx 70\,\text{pm}$, PLL bandwidth = 10 Hz.

F_6PEN on Cu(111)

F_6PEN molecules were evaporated for 5 minutes (Figure 4.5 (a): 3 minutes) at $\approx 493\,\text{K}$ directly onto the cold Cu(111) sample surface ($\approx 7\,\text{K}$) inside the SPM chamber. Sensor parameters: Resonance frequency $\omega_0 \approx 26.99\,\text{kHz}$, quality factor Q $\approx$ 15 - 72 k, oscillation amplitude $A_{\text{osc}} = 400\,\mu\text{V}$ corresponding to $\approx 70\,\text{pm}$, PLL bandwidth = 10 Hz.

3.4 Experimental Details on Chapter 5

(8)CPP molecules were evaporated for 2 minutes (Figure 5.3 (c): 2.5 minutes) at $\approx 553\,\text{K}$. (10)CPP molecules were evaporated for 4 minutes at $\approx 578\,\text{K}$ plus additional 4 minutes at $\approx 588\,\text{K}$ without performing a sample cleaning. Molecules were evaporated directly onto the cold sample surface ($\approx 7\,\text{K}$) inside the SPM chamber. If not stated elsewhere, the sample was heated at the respective mentioned temperatures for 30 minutes (Figure 5.3 (a): 50 minutes). The tip was grounded, all bias voltages mentioned refer to the sample bias voltage. AFM images were acquired in constant height and constant current mode and were performed in frequency modulation mode using an external phase-locked loop (*Zurich Instruments*, Switzerland). Sensor parameters: Resonance frequency $\omega_0 \approx 26.99\,\text{kHz}$, quality factor Q $\approx$ 17 - 49 k, oscillation amplitude $A_{\text{osc}} = 400\,\mu\text{V}$ corresponding to $\approx 70\,\text{pm}$, PLL bandwidth = 10 Hz. During AFM imaging, a small gap voltage of $V_g = -0.57\,\text{mV}$ was applied to compensate for internal offsets of the current amplifier. All STM and AFM measurements were performed at cryogenic temperatures of 5.2 K.

4 Self-Assembly of Unilaterally Fluorinated Pentacene Molecules on Au(111) and Cu(111)

4.1 Introduction

A powerful tool to steer the formation of three-dimensional supramolecular arrangements in molecular crystal architecture are intermolecular interactions of hydrogen and fluorine atoms (in the following referred to as H-F interactions) [178, 179, 180]. The same principle can be extended to two dimensions to direct molecular self-assembly processes on metal surfaces through H-F interactions [146, 181, 182, 183]. Recent studies have shown that reactions involving well-aligned, adjacent hydrogen and fluorine atoms can lead to the formation of covalent carbon-carbon bonds through a process denoted as H-F zipping or cyclodehydrofluorination reactions [21, 184, 185, 186]. For example, Fan et al. have demonstrated that H-F zipping can be employed to synthesize a remarkable nonbenzenoid biphenylene network by fusion of poly(2,5-difluoro-para-phenylene) intermediates [21]. Further, Grossmann et al. successfully synthesized exceptional two-dimensional polymers that exhibit mesoscale ordering by photopolymerization, whereas precursors were initially aligned through H-F interactions [126]. The alignment and positioning of the precursors in the sub-monolayer regime is an important concept for on-surface synthesis, as it can mark the pre-step prior to the on-surface reaction. Consequently, the precise alignment of the precursor's atoms and bonds can dictate the local product formation, even when using identical precursors. Therefore, it is crucial to obtain a profound understanding of self-assembly processes of organic molecules on surfaces. Nonetheless, due to the intricate interplay of the substrate with the adsorbed molecules, which often contain complex substitutes, self-assembly processes are usually difficult to predict. As a consequence, experimental studies are required to determine the complex adsorption structures and the local arrangement of the molecules. For further information see Section 2.4. However, since a large portion of on-surface reactions are performed through Ullmann-type reaction steps (see Section 2.5.1), the intermolecular H-F interactions on surfaces are so far only investigated in a few experimental studies with molecular resolution [146, 182, 183]. To enhance the comprehension of self-assembly facilitated by H-F interactions in on-surface reactions, it is essential to analyze these interactions on the sub-molecular level in order to obtain fundamental insights.

In this study, we investigate the H-F interactions on inert Au(111) and reactive Cu(111) coinage metals, which are state-of-the-art substrates for on-surface reactions. The linear 1,2,10,11,12,14-hexafluoropentacene (F_6PEN, $C_{22}H_8F_6$) molecule [187], which is fluorinated unilaterally along the horizontal molecule axis (see sketch in Figure 4.2 (b)), acts as a

self-assembly model system for the investigations. H-F interactions are studied in detail by exploiting the self-assembly of F_6PEN, using combined STM and chemical bond imaging measurements. The self-assembly of regular pentacene [135, 136, 137, 143, 188] and the effect of full fluorination [141, 142, 189, 190, 191, 192, 193] was extensively investigated on various substrates. However, the unilaterally fluorinated F_6PEN, which allows for the investigation of H-F interactions, was so far only studied using STM on an unreactive molybdenum disulfide substrate [140], which is, due to its low catalytic activity, not commonly used to perform on-surface reactions.

Our results indicate that, owing to the strong intermolecular interaction, F_6PEN forms dimers and small clusters even at cryogenic temperatures, whereas a transformation into larger clusters is observed with increasing temperatures on Au(111). This unique self-assembly pattern is exploited to investigate the distances and angles of H-F interactions on a local level. Therefore, molecules in various cluster sizes are imaged with ultra-high precision using the chemical bond imaging method. While the arrangements of the molecules appear to be similar in increasing cluster sizes, only by chemical bond imaging measurements it could be revealed that the local alignments differ within monolayers. The precisely determined crystal structure is compared to a calculated bulk crystal structure. Further, an alternative crystal structure could be revealed that remained undetectable via conventional STM measurements. Although the self-assembly process of F_6PEN on Cu(111) is not fundamentally different from that on Au(111), there are indications suggesting stronger molecule-substrate interactions on Cu(111). While the molecules adsorb almost parallel to the surface on Au(111), their interaction with Cu(111) induces a noticeable bending in the center of the molecules. This bending is further investigated by means of reconstructed topography images, using a stack of AFM images taken at sequential heights and currents. While densely packed dimer structures can only be found in specific interaction environments, the molecular arrangements within the dense layer on Cu(111) feature stacks of two and three molecules with discernible gaps between them. In summary, our systematic study reveals precise alignments of hydrogen and fluorine atoms of adjacent F_6PEN molecules in different interaction environments. The results suggest that the intermolecular H-F interactions exhibit a directional character. Even though molecular bending indicates a strong interaction on the reactive Cu(111), the intermolecular H-F interactions allow the molecules to arrange themselves in an ordered manner, making them a valuable tool for their use in on-surface synthesis on inert and reactive surfaces.

4.2 Results and Discussion

4.2.1 Self-Assembly Process of F_6PEN on Au(111)

An overview of the evolution of the temperature induced self-assembly process of F_6PEN molecules on Au(111) is shown in Figure 4.1 for six representative temperatures ranging from 7 - 473 K. Note that all STM and AFM images were taken at cryogenic temperatures of approximately 5.2 K. The STM overview image of the as deposited molecules at a temperature of about 7 K is presented in Figure 4.1 (a). Individual monomers, dimers and small molecular clusters comprising approximately three to five molecules are observed. Note that, prior to the main molecule evaporation, the sample was annealed at 89 K with a minimal coverage of molecules. Subsequently, a higher number of molecules was evaporated without performing a sample cleaning. Consequently, some larger clusters may already be present at lower temperatures of 7 K and 32 K. However, Figure A.1 shows an overview STM image of the surface after annealing at 89 K and before performing the main molecule evaporation, where only larger clusters of more than ten F_6PEN molecules are present. Consequently, the formation of dimers and smaller clusters in Figure 4.1 (a) is not the result of sample annealing. Interestingly, this is in contrast to unsubstituted pentacene molecules on Au(111), which only form densely packed structures at a high coverage [135]. For the fully fluorinated perfluoropentacenes, the formation of molecular islands is observed on an Au(111) substrate held at room temperature (RT) [142]. This indicates that the attraction of the F_6PEN molecules at low coverage and cryogenic temperatures might be a consequence of the altered charge distribution, resulting from the partial fluorination of the molecules [140, 187].

At 32 K and 54 K (see Figure 4.1 (b) and (c)), the temperature induced surface diffusion results in a higher number of larger clusters. The size of the clusters increases with elevated temperatures, resulting in a corresponding decrease in the number of individual molecules and small clusters. At 89 K (see Figure 4.1 (d)), a transition from small unordered clusters to semi-organized molecule chains can be observed. The length of these chains varies from about five to 20 molecules. While at 7 K and 32 K, the molecules seem to adsorb in an arbitrary position, most of the bigger clusters and molecule rows at 54 K and 89 K adsorb in the more reactive fcc domain of the Au(111) herringbone reconstruction [194], which can also be observed for e.g. triphenylene molecules [138]. Upon annealing the sample to RT (see Figure 4.1 (e)), a further transformation into large molecular sheets is observed. These sheets show a sequential arrangement of stacked molecular lines, each line comprising approximately 40 molecules, with a minimum width of 80 nm. This state remains stable up to at least 473 K, as evidenced by the STM image in Figure 4.1 (f).

The adsorption positions of the molecules within larger sheets appear to be unaffected by the more reactive fcc sites of the herringbone reconstruction. The lattice parameters of the large F_6PEN sheets were determined as $\vec{a} = 16.6 \pm 0.1$ Å, $\vec{b} = 7.5 \pm 0.1$ Å and $\gamma = 71.5 \pm 1\,^\circ$, revealing an oblique unit cell. For more information see Figure A.7. This corresponds relatively well with the lattice parameters of $\vec{a} = 16.6 \pm 1.0$ Å, $\vec{b} = 7.3 \pm 1.0$ Å and $\gamma = 70 \pm 5\,^\circ$, found on a less reactive molybdenum disulfide substrate, as determined by overview STM images [140]. These determined lattice vectors are in good agreement with the $\sqrt{31} \times \sqrt{7}R70$ lattice of the Au(111) crystal, indicating the formation of a periodic

F_6PEN superstructure on the Au(111) lattice. For more information see Figure A.8. Similar to their behavior on the molybdenum disulfide substrate, F_6PEN molecules exhibit a non-alternating packing motif on Au(111), with all molecules oriented in the same direction. However, for 1,2,3,4,5,14-hexafluoro-6,13-diazapentacene, which is, in contrast to the herein investigated F_6PEN, fluorinated along the vertical molecule axis, an alternating packing motif is observed on molybdenum disulfide [140].

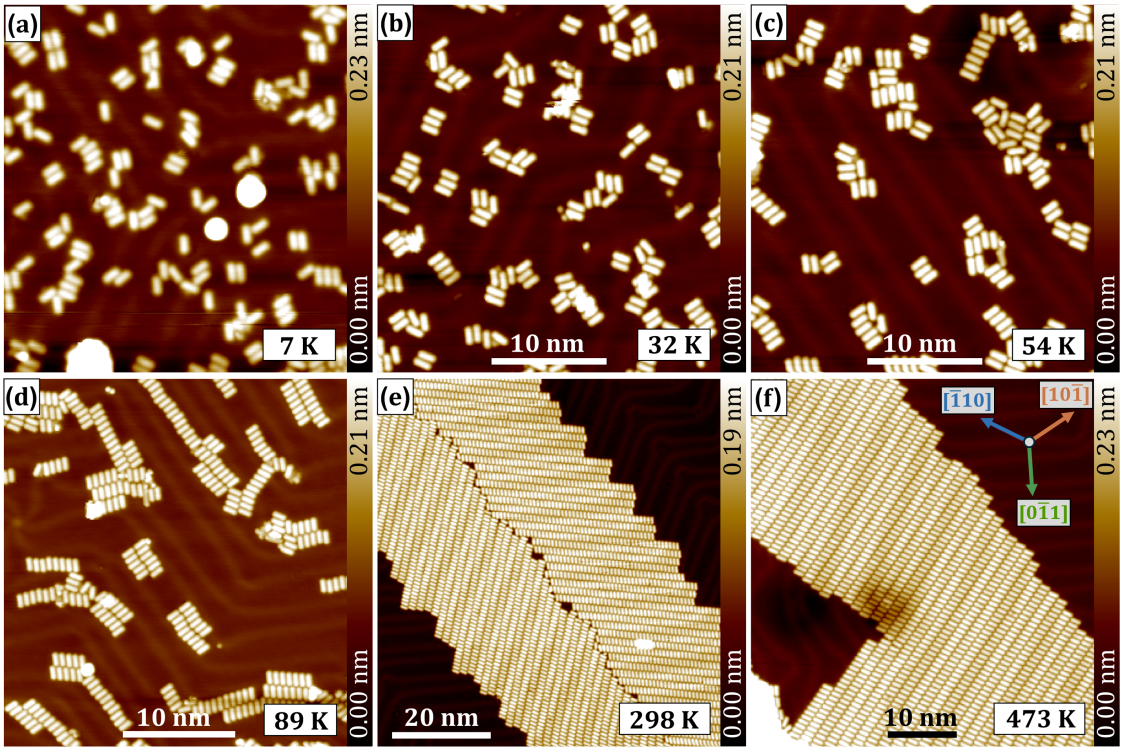


Figure 4.1: Temperature induced self-assembly process of F_6PEN on Au(111). The STM overview images show a transition from single molecules and small clusters to larger clusters and densely packed layers at elevated temperatures. STM overviews are shown for (a) $T = 7\,\mathrm{K}$ (as deposited) and after annealing to (b) $T = 32\,\mathrm{K}$, (c) $T = 54\,\mathrm{K}$, (d) $T = 89\,\mathrm{K}$, (e) $T = 298\,\mathrm{K}$ and (f) $T = 473\,\mathrm{K}$. Imaging parameters: (a) $V_\mathrm{g} = 100\,\mathrm{mV}$, $I_\mathrm{t} = 10\,\mathrm{pA}$, (b) $V_\mathrm{g} = 100\,\mathrm{mV}$, $I_\mathrm{t} = 10\,\mathrm{pA}$, (c) $V_\mathrm{g} = 100\,\mathrm{mV}$, $I_\mathrm{t} = 10\,\mathrm{pA}$, (d) $V_\mathrm{g} = 100\,\mathrm{mV}$, $I_\mathrm{t} = 10\,\mathrm{pA}$, (e) $V_\mathrm{g} = 100\,\mathrm{mV}$, $I_\mathrm{t} = 10\,\mathrm{pA}$ and (f) $V_\mathrm{g} = 100\,\mathrm{mV}$, $I_\mathrm{t} = 30\,\mathrm{pA}$. Note: Prior to the main molecule evaporation, the sample was annealed to 89 K with a low coverage of molecules. Subsequently, a higher number of molecules was evaporated without cleaning the sample. Consequently, some larger clusters may already be present at low temperatures of 7 K and 32 K.

The exact adsorption geometry of single F_6PEN molecules is further investigated using the chemical bond imaging method. In the AFM image in Figure A.2, two different relative scanning heights with respect to the molecule and substrate were chosen to resolve the underlying substrate as well as the molecule in the same image. The underlying surface structure reveals that the molecule aligns along the densely packed [0$\bar{1}$1] direction. Generally, most of the investigated F_6PEN molecules align along one of the densely packed

[$0\bar{1}1$], [$10\bar{1}$] or [$\bar{1}10$] directions, whereby the ratio is approximately one third per crystal direction. About ten percent of the molecules are not oriented along any of the three principal directions. More information can be found in the supplementary material in Figure A.3 and Table A.1 and A.2.

So far, the self-assembly process and lattice parameters of the F_6PEN molecules were determined by STM measurements. However, due to the lack of lateral resolution when imaging molecules using STM (explained in Section 2.2 and 2.3.4), it is not possible to probe the nature of the H-F interaction in assembled F_6PEN molecules. Therefore, now we focus on the investigation of the self-assembly process using the chemical bond imaging method, due to its advantages in lateral resolution compared to conventional STM measurements. Since F_6PEN molecules gradually form larger clusters with increasing temperatures, the linear molecule is suitable as a model system for investigating the H-F interactions. Consequently, the molecular arrangements across various cluster sizes and interaction environments, which are defined by molecule-substrate and molecule-molecule interactions, can be investigated. Therefore, the relative orientation of pairs of molecules in various settings, as well as the precise bond distances and angles between hydrogen and fluorine atoms, can be accurately identified.

Figure 4.2 presents a set of ch-AFM images recorded with a CO tip, illustrating the formation of F_6PEN molecules into various cluster sizes. The single Dimer, utilized as a reference for comparing molecular arrangements and bond interactions within larger clusters, is depicted in Figure 4.2 (a). Additional clusters investigated in this study include a Tridecamer (see Figure 4.2 (d)), a square-shaped cluster referred to as Cluster 1 (see Figure 4.2 (e)), a rectangular-shaped cluster designated as Cluster 2 (see Figure 4.2 (f)), a small chain formed by a Hexamer of molecules (see Figure 4.2 (g)) and a Monolayer formed by the F_6PEN molecules, illustrated in Figure 4.2 (h). As evident in the AFM images, the hydrogen and fluorine atoms in two stacked molecules are not oriented perpendicular to each other, despite their opposite charge. Instead, they exhibit a horizontal displacement relative to each other, which prevents the formation of linear chains. Moreover, it is observed that this displacement does not consistently occur in the same direction. The upper molecule may be displaced to the left or right relative to the underlying molecule (see blue and yellow arrows in Figure 4.2 (d)). If a molecule is shifted to the left or right can be assigned solely by AFM measurements, as a fixed molecular orientation is needed as a starting point, because the molecule does not have a horizontal mirror axis. The analysis of a total of ten AFM images and 139 investigated molecules reveals an approximately equal distribution with a ratio of 48:52 (right:left). Additional information is presented in Figure A.4 and Table A.3.

Figure 4.2 (b) shows the same image of the F_6PEN Dimer with superimposed molecular structures that are used to determine the distances and angles of the H-F arrangements in the respective clusters. In the sketch, carbon atoms are depicted in red, hydrogen and fluorine atoms are represented in yellow and green, respectively. A zoom-in (see Figure 4.2 (c)) illustrates a representative, detailed H-F interaction with the corresponding distance (shown as a dashed blue line) and the angles φ_1 and φ_2. Further, the effective angle θ_{eff} is determined, which describes the head-on angle of the fluorine and hydrogen atoms, virtually shifted perpendicular to each other. For more information on the effective angle θ_{eff} see Figure A.5 (c). For the example of the fluorine atom in Figure 4.2 (c), sitting on the outer left of the molecule, only one H-F interaction can be observed. Note that all other fluorine atoms shown in Figure 4.2 (b) are interacting with a hydrogen atom on their left and right side respectively, leading to a total of seven investigated H-F interactions per dimer. The distances and angles for the respective H-F interactions in the Dimer (see Figure 4.2 (b)) are listed in Table 4.1, leading to means for the distances of 269 pm (standard deviation distance $\sigma_d = 9$) and angles of 153 ° (standard deviation angle $\sigma_\varphi = 4$). The bonding pattern can be described as quasi-type I halogen bond, where φ_1 equals φ_2 [149] (see Figure 2.9 (c)), with effective angles of or close to 180 °. In the following, this bonding pattern is referred to as H-F interaction Type A.

Table 4.1: Distances and angles of the H-F interactions in the Dimer structure (see Figure 4.2 (b)).

	1	**2**	**3**	**4**	**5**	**6**	**7**
Distance [pm]	263	258	262	262	276	280	280
$\boldsymbol{\varphi_1}$ [°]	151	157	153	161	147	152	145
$\boldsymbol{\varphi_2}$ [°]	155	156	154	158	148	150	148
$\boldsymbol{\theta_{\text{eff}}}$ [°]	176	179	179	177	179	178	176

For data processing and comparison, the seven interactions were determined for one dimer in each F_6PEN cluster shown in Figure 4.2. In the Monolayer, three different dimers were chosen, denoted as ML Dimer 1, ML Dimer 2 and ML Dimer 3. The respective dimer structures used for data processing are superimposed by red molecule sketches in the corresponding images.

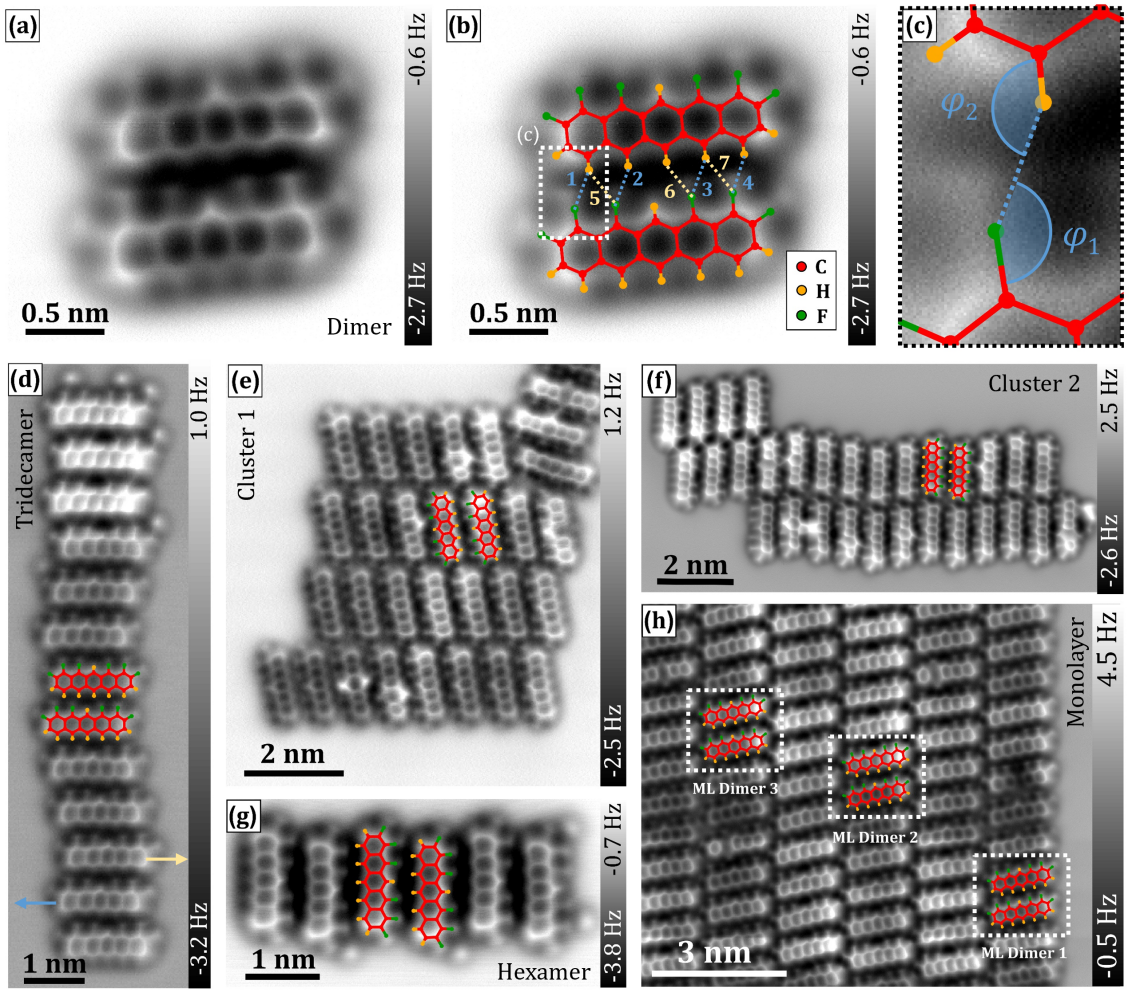


Figure 4.2: Set of ch-AFM images showing different molecular cluster sizes. The respective dimer structures fitted into the figures were used for data processing. For comparison, the different clusters are designated with specific names, as illustrated in the images. (a) F_6PEN Dimer ($T = 7\,\mathrm{K}$) and (b) Dimer with fitted molecular structures. Color code: carbon (red), hydrogen (orange) and fluorine (green). (c) Zoom-in (see box in subfigure (b)) showing an exemplary H-F interaction. The interaction can be described by the distance between hydrogen and fluorine atoms, the angles φ_1, φ_2 and an effective angle θ_{eff}. (d) Tridecamer ($T = 85\,\mathrm{K}$), (e) Cluster 1 ($T = 89\,\mathrm{K}$), (f) Cluster 2 ($T = 89\,\mathrm{K}$), (g) Hexamer ($T = 85\,\mathrm{K}$) and (h) Monolayer ($T = 473\,\mathrm{K}$). In the following, the presented structures are referred to using capital letters to indicate that reference is made to the specific structures depicted in this figure. Imaging parameters: (a) and (b) $\Delta z = -10\,\mathrm{pm}$, (d) $\Delta z = -88\,\mathrm{pm}$, (e) $\Delta z = 0\,\mathrm{pm}$, (f) $\Delta z = -20\,\mathrm{pm}$, (g) $\Delta z = -43\,\mathrm{pm}$ and (h) $\Delta z = -25\,\mathrm{pm}$. Scanning heights are given with respect to the STM setpoint of (a) and (b) $V_\mathrm{g} = -0.57\,\mathrm{mV}$, $I_\mathrm{t} = 30\,\mathrm{pA}$ and (d) - (h) $V_\mathrm{g} = -0.57\,\mathrm{mV}$, $I_\mathrm{t} = 10\,\mathrm{pA}$.

For all investigated bonds of the dimers in the different cluster sizes, slightly varying bond distances in the same order of magnitude ranging from 207 - 280 pm (mean = 253 pm, σ_d = 17) can be observed. The determined angles between the hydrogen and fluorine atoms are ranging from 136 - 161 ° (mean = 150 °, σ_φ = 5) and can be described as Type A bonds. With the given hydrogen-fluorine distances and angles, the bond may be characterized as a weak to moderate hydrogen bond [195]. The spreading of the values for the distances and angles might be a result of the non-perpendicular, but slightly tilted C-F bonds in the F_6PEN molecule (see Figure 4.2 (b)) with respect to the vertical axis. Also the relative position of the two molecules in the investigated dimers plays a role, which will be discussed in more detail in Figure 4.3. An overview of the measured angles φ_1 and φ_2 can be found in Figure A.5 (a). The errors for the distances and angles between the bonds were determined to be ± 20 pm and ± 5 °, using different fits for the upper molecule structure in an exemplary dimer. For more information see Figure A.6 and Table A.4 and A.5. Overall, the H-F bonding motif in all investigated interaction environments (Dimer to Monolayer) resembles a quasi-type I halogen bond ($\varphi_1 = \varphi_2$) pattern. However, for thus far investigated H-F interactions with sub-molecular resolution, the self-assembly process of densely packed rows of unilaterally fluorinated phenylethynylbenzene [182], a coadsorption of phenylethynylbenzene and fully fluorinated phenylethynylbenzene [146] and 1,3,5-trifluorobenzene [183] in densely packed environments, predominantly results in a bonding motif exhibiting unequal H-F bonding angles ($\varphi_1 \neq \varphi_2$).

Despite the ultra-high precision with which the previously investigated distances and angles were determined using the chemical bond imaging method, the measured values exhibit variability. This spreading precludes definitive conclusions about differences in the exact molecular arrangements within various cluster sizes. To further precisely investigate the arrangements of the molecules, the experimentally obtained AFM images are compared to a calculated bulk crystal structure. Figure 4.3 (a) shows a two-dimensional tetramer section of a layer of the calculated F_6PEN bulk crystal structure oriented along a flat plane. The lattice parameters of the calculated structure fully describe the two-dimensional crystal structure of F_6PEN and were determined as $\vec{a}_{\text{calc}}$ = 16.6 Å, $\vec{b}_{\text{calc}}$ = 7.4 Å and γ_{calc} = 71.5 °. Relevant H-F interactions of the molecules are depicted by red dashed lines. Alternatively, single rows of the crystal structure can be described by the angle $\alpha = \gamma - 8.4\,°$ and the distance between the same atoms in stacked molecules, as represented by a dashed bright blue line. In the representation of Figure 4.3 (a), the molecules are tilted by 8.4 ° with respect to the horizontal axis. When this angle α is determined for the dimer structures shown in Figure 4.2, it seems to slightly adjust to the α of the calculated structure for the experimental dimers which were fitted farther inside the Monolayer (ML Dimer 2 and ML Dimer 3). The values are displayed in Figure A.5 (b), the corresponding determined errors are shown in Table A.6. This trend is further corroborated by examining a selection of tetramers superimposed on the experimental AFM image within the Monolayer. Figure 4.3 (b) shows the ch-AFM image of the Monolayer (see Figure 4.2 (h)) with three fitted tetramer structures. One structure is fitted at the edge of the layer (orange tetramer), one in the middle (blue tetramer) and another farther inside the layer (red tetramer). Due to the high resolution of the AFM images acquired by chemical bond imaging, it is possible to compare these precisely fitted molecules in the experimental image to the structure of the calculated tetramer. This is illustrated in Figure 4.3 (c) by overlapping the calculated (black) and experimental (red, blue, orange) structures, respectively. The structures were superimposed in such a way that the lower

left F_6PEN molecule of the calculated black and colored experimental structure exactly matched. The corresponding lattice parameters are highlighted by dashed boxes using the same color code. It can be observed that the experimental orange structure at the edge of the Monolayer does not align well with the calculated structure, since a displacement of the colored molecules in the upper row is present. Interestingly, upon comparing the other two experimental tetramers with the calculated structure, it becomes evident that they assimilate as they extend farther into the Monolayer. Specifically, the blue structure aligns relatively well, while the red structure nearly exactly matches the calculated structure. The red tetramer has the same lattice vectors as the calculated structure and the angle γ only deviates by $0.7\,^\circ$. For the blue and orange structure, the lattice vectors also match relatively well, but the angle γ deviates by several degrees.

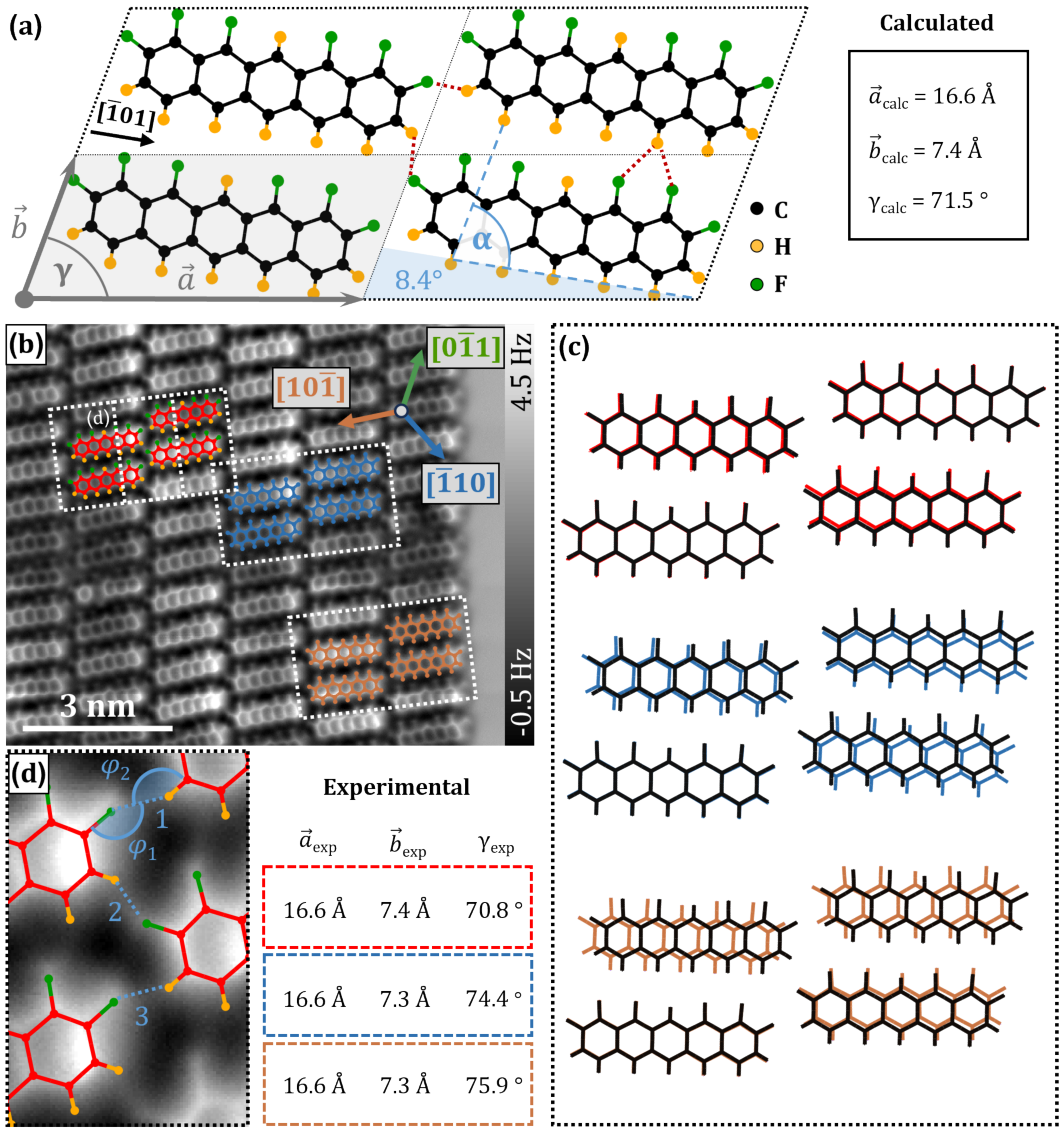


Figure 4.3: (a) Calculated bulk crystal structure of F_6PEN. The structure can be fully described by two vectors $\vec{a}_{\text{calc}}$, $\vec{b}_{\text{calc}}$ and the angle γ_{calc}. Alternatively, the orientation of the molecules is given by the rotation and the distance of the same atom positions in two molecules which are arranged on top of each other. This is depicted by dashed blue lines and the angle α. Latter can be defined as $\alpha = \gamma - 8.4\,°$, where $8.4\,°$ corresponds to the tilting of the molecules with respect to the horizontal axis. Relevant H-F interactions are shown as dashed red lines. (b) AFM image of the Monolayer with three fitted tetramers at different positions inside the Monolayer, colored in orange, blue and red. (c) The sketches illustrate an overlap of the fitted tetramers inside the Monolayer with the calculated crystal structure depicted in black color. The structures are superimposed in such a way that the lower left molecules of the calculated and experimental structure exactly match. Experimentally determined vectors and angles are presented in dashed boxes with the same color code. (d) Zoom-in (see box in subfigure (b)) to determine the distances and angles of the H-F interactions for molecules in adjacent molecule lines. Corresponding distances and angles φ_1, φ_2 and θ_{eff} are listed in Table 4.2. Thanks to Maximilian Dreher and Gregor Witte for providing the F_6PEN molecules and the calculated crystal structure.

The advantages of the chemical bond imaging method are again evident upon examining this precise analysis. While the lattice vectors determined via STM ($\vec{a}$ = 16.6±0.1 Å, $\vec{b}$ = 7.5±0.1 Å and γ = 71.5±1 °; Figure A.7) correspond well with these of the calculated crystal structure, such a local analysis cannot be carried out using STM due to the lack of molecular resolution. In general, it was found that the interaction of F_6PEN is predominantly governed by the H-F interactions. These often have an electrostatic character and can also exhibit covalent components at small atomic distances [196]. This is evidenced by the consistent distances and angles between hydrogen and fluorine atoms observed for small and larger clusters, as well as for dimers within the Monolayer. Even though the molecules align along certain crystal directions, this observation suggests that the molecular interactions occur primarily undisturbed on the Au(111) surface. Only through the analysis using the chemical bond imaging method presented in Figure 4.3 it becomes apparent that the intermolecular interactions may change when the molecules are entirely enclosed by neighboring molecules, leading to an assimilation of the lattice parameters with respect to the calculated structure. This may be the case because, in contrast to small clusters where interactions are predominantly governed by the intermolecular interactions of hydrogen and fluorine atoms among a few molecules, van der Waals forces and H-F interactions with neighboring molecules also come into play within monolayers. The additional interactions may contribute to the assimilation of the experimental structure farther inside the Monolayer with the calculated structure, since the interactions with the surrounding molecules are also considered in the calculation of the bulk crystal structure.

Finally, the bonding configurations of H-F interactions in adjacent molecule lines will be discussed. Figure 4.3 (d) provides a close-up view of four F_6PEN molecules in neighboring rows, with the respective bonds indicated by dashed blue lines. The results of the analysis are gathered in Table 4.2.

Table 4.2: Distances and angles of the H-F interactions of molecules in adjacent molecule lines inside the Monolayer (see Figure 4.3 (d)).

	1	**2**	**3**
Distance [pm]	220	206	203
$\boldsymbol{\varphi_1}$ [°]	153	144	154
$\boldsymbol{\varphi_2}$ [°]	153	146	153
$\boldsymbol{\theta_{\text{eff}}}$ [°]	180	178	179

In summary, the bond lengths vary between 203 - 220 pm (mean = 210 pm, σ_d = 7), while the bond angles range from 144 - 154 ° (mean = 151 °, σ_φ = 4), with effective angles around 180 °. As for the dimers in the varying cluster sizes (see Figure 4.2), these interactions can be characterized as quasi-type I halogen bonds, where φ_1 equals φ_2, exhibiting effective angles of (or close to) 180 °. However, the mean values for the distances differ by about 40 pm compared to the dimers in the varying cluster sizes. Therefore, a new bonding pattern for hydrogen and fluorine atoms of molecules in neighboring lines is defined, which is in the following referred to as H-F interaction Type B.

In addition to the crystal structure shown in Figure 4.3, in which all molecules in the same and neighboring rows are aligned in the same direction, another crystal structure for F_6PEN was revealed using the chemical bond imaging method. This structure is analyzed in Figure 4.4.

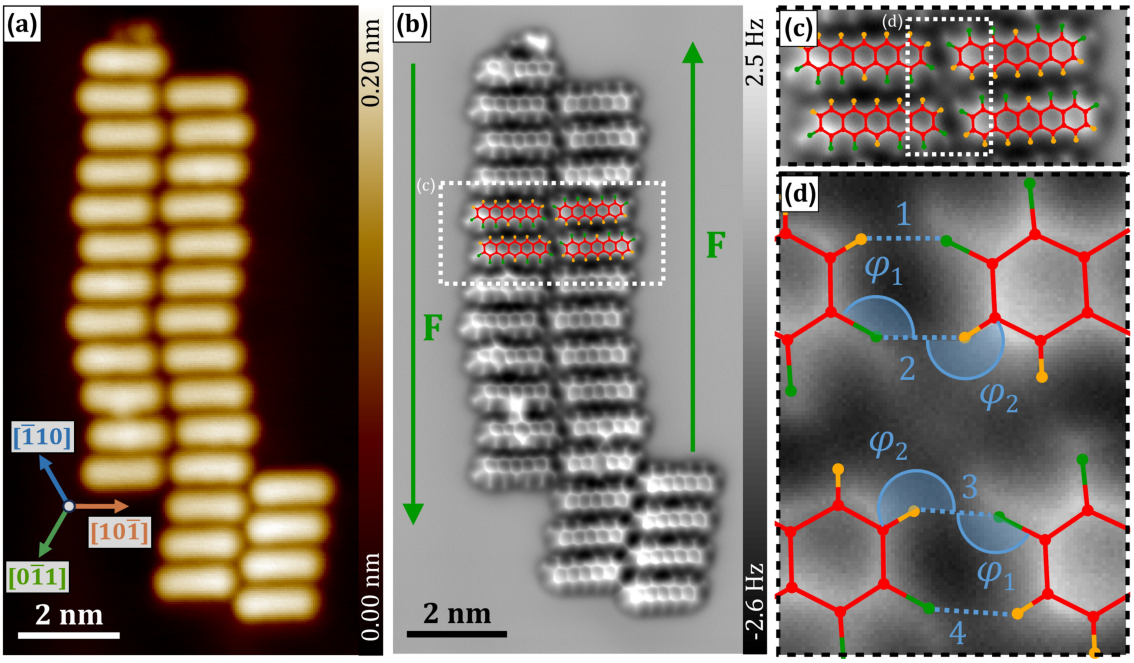


Figure 4.4: Alternative crystal structure that is formed by F_6PEN molecules. (a) STM image of Cluster 2. (b) High-resolution ch-AFM image, allowing for the determination of the absolute orientation of the F_6PEN molecules. The orientation of fluorine atoms is indicated by green arrows. (c) Zoom-in showing a molecule tetramer of the alternative crystal structure. (d) Zoom-in revealing the bonding configuration of the molecules in adjacent molecule lines. The distances and angles φ_1, φ_2 and θ_{eff} are determined for four bonds respectively (see Table 4.3). Imaging parameters: (a) $V_g = 100\,\text{mV}$, $I_t = 10\,\text{pA}$ and (b) $\Delta z = -20\,\text{pm}$ with respect to the STM setpoint of $V_g = -0.57\,\text{mV}$, $I_t = 10\,\text{pA}$.

Figure 4.4 (a) shows a STM image of Cluster 2 (see Figure 4.2 (f)). In the STM image, the F_6PEN molecules appear as symmetric ovals. Even though the image was recorded with a CO tip, the direction in which the fluorine atoms point cannot be assigned with the chosen imaging parameters. Using the chemical bond imaging method, the fluorinated side can be revealed, as indicated by green arrows in the AFM image in Figure 4.4 (b). In this alternative crystal structure, the fluorine atoms in adjacent molecular rows are oriented in different directions, as further illustrated in the magnified images in Figure 4.4 (c) and (d). The distances and angles determined for four H-F interactions of molecules in adjacent lines are listed in Table 4.3.

Table 4.3: Distances and angles of the H-F interactions of molecules in adjacent molecule lines in the alternative crystal structure (see Figure 4.4 (d)).

	1	**2**	**3**	**4**
Distance [pm]	224	233	224	233
$\boldsymbol{\varphi_1}$ [°]	155	152	158	155
$\boldsymbol{\varphi_2}$ [°]	212	214	215	217
$\boldsymbol{\theta_{\text{eff}}}$ [°]	123	119	123	119

While the distances between the fluorine and hydrogen atoms (224 - 233 pm, mean = 229 pm, σ_d = 5) differ by only about 20 pm compared to Type B of the neighboring conformation shown in Figure 4.3 (d), the angles φ_1, φ_2 and θ_{eff} exhibit significant deviations. These range between 152 - 217 ° (mean = 185 °, σ_φ = 30), exhibiting effective angles of about 120 °. Therefore, this structure may not be classified as quasi-type I halogen bond. Hence, compared to the crystal structure shown in Figure 4.3, a distinctly different bonding pattern is observed. In the following, this bonding pattern is referred to as H-F interaction Type C. Interestingly, bonding pattern Type C is exclusively observed at lower temperatures up to 89 K. At elevated temperatures, all molecules in the monolayers align in such a way that the fluorine atoms point in the same direction. This suggests that the structure depicted in Figure 4.3 (d), in which one molecule interacts with two molecules from an adjacent line, appears to be energetically more favorable than the structure presented in Figure 4.4 (d), where only one molecule interacts with another molecule in a neighboring row.

4.2.2 Self-Assembly Process of F_6PEN on Cu(111)

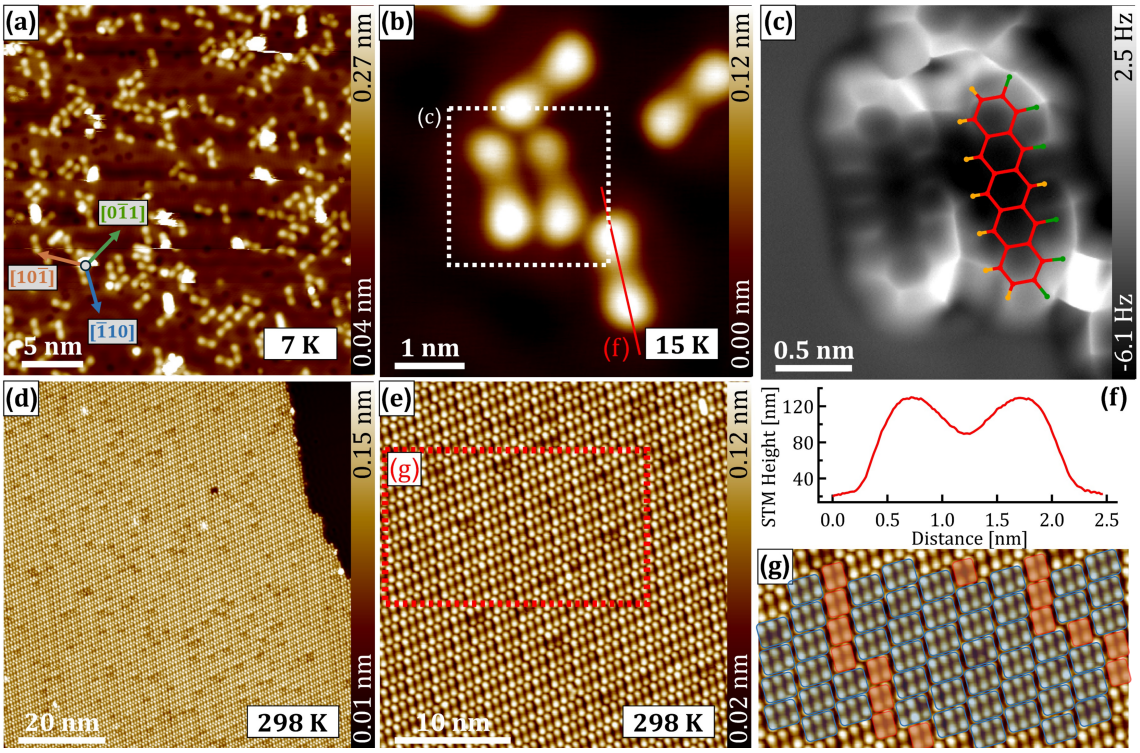


Figure 4.5: Overview of the self-assembly process and adsorption configuration of F_6PEN on Cu(111). The STM images reveal a transition from single molecules to layers at elevated temperatures. STM images are recorded at (a) $T = 7\,\mathrm{K}$ (as deposited) and after annealing to (b) $T = 15\,\mathrm{K}$. (c) cc-AFM image of a F_6PEN dimer. (d) and (e) A transition to seemingly densely packed layers is observed after annealing to $T = 298\,\mathrm{K}$. (f) STM height profile of a F_6PEN monomer. (g) Section of Figure (e) with colored overlaid dimer (orange) and trimer (blue) assemblies. Imaging parameters: (a) $V_g = 100\,\mathrm{mV}$, $I_t = 10\,\mathrm{pA}$, (b) $V_g = 100\,\mathrm{mV}$, $I_t = 10\,\mathrm{pA}$, (c) $V_g = 20\,\mathrm{mV}$, $I_t = 200\,\mathrm{pA}$, (d) $V_g = 100\,\mathrm{mV}$, $I_t = 10\,\mathrm{pA}$ and (e) $V_g = 100\,\mathrm{mV}$, $I_t = 30\,\mathrm{pA}$.

Now we focus on the self-assembly process of F_6PEN molecules on a more reactive Cu(111) substrate. Figure 4.5 (a) shows a STM overview image of the as deposited F_6PEN molecules on the Cu(111) surface. The STM image reveals distinct differences in the adsorption behavior of the as deposited F_6PEN molecules in comparison to these on the Au(111) substrate. This is evidenced by the lower number of formed dimers and clusters on Cu(111). If two molecules are adsorbed in close proximity, a recognizable gap is visible between them, indicating a substrate-modulated snap-in effect. Another remarkable difference, compared to F_6PEN on Au(111), is the mere appearance of the molecules in the STM image. While the molecules on the Au(111) surface exhibit a nearly planar adsorption conformation, a noticeable bending occurs on Cu(111). The bending is characterized by two distinct bright elevations at the edges of the molecule, while the central region exhibits a darker contrast, as can be seen in Figure 4.5 (b). This is additionally verified by the STM line profile illustrated in Figure 4.5 (f). The unique adsorption configuration of F_6PEN will

be further analyzed in Figure 4.7 by means of three-dimensional AFM spectroscopy. As for Au(111), the exact orientation of the molecules on Cu(111) was determined, revealing alignments along the densely packed $[0\bar{1}1]$, $[10\bar{1}]$ or $[\bar{1}10]$ directions. For more information see Figure A.9. While on Au(111) approximately ten percent of the molecules are not oriented along one of the three crystal directions after deposition, the stronger molecule-substrate interaction on Cu(111) results in a snap-in of all adsorbed molecules with an equal distribution along the three $[0\bar{1}1]$, $[10\bar{1}]$ or $[\bar{1}10]$ directions. For more information see Figure A.10 and Table A.7. An orientation along the same directions can also be observed for regular pentacenes adsorbed on Cu(111) [197].

Figure 4.5 (c) shows a magnified cc-AFM image of a F_6PEN dimer after annealing the sample at 15 K. A single molecular structure is superimposed on the AFM image to indicate the adsorption orientation of the molecules. The distances and angles of the analyzed bonds are 233 - 275 pm (mean = 256 pm, $\sigma_d = 13$) and 142 - 160 ° (mean = 152 °, $\sigma_\varphi = 5$), corresponding well with these of the dimers in varying cluster sizes determined on Au(111). Therefore, they can be also classified as H-F interaction Type A. However, it might be important to notice that stable dimer assemblies on Cu(111) may not exist, as the only dimers that can be imaged using AFM are stabilized by other molecules, as in the case of Figure 4.5 (c). If dimer structures are imaged that are not stabilized by surrounding molecules, one of the molecules jumps back and forth in consecutive AFM scans. Figure A.11 (a) and (b) reveal that, similar to the adsorbed monomer on Cu(111) (see Figure A.9), one of the molecules snaps into a stable position with the centers of the phenyl rings placed above hcp hollow sites. This molecule can be imaged without manipulation. However, the second molecule does change the position between two bridge sites, indicating a less stable adsorption conformation. Nevertheless, the close proximity of the two molecules suggests a significant intermolecular interaction between them.

Despite the high reactivity of the Cu(111) substrate, the molecules form large, apparently ordered molecular sheets comprising widths of at least 100 nm after annealing the sample at RT (see Figure 4.5 (d)). In the literature, two different results are found for the adsorption behavior of regular pentacenes on Cu(111) after molecule deposition on a sample held at RT. On the one hand, it is reported that the molecules do not form sheets. Consequently, the overview STM image of pentacenes on Cu(111) at RT resembles the one in Figure 4.5 (a) of the as deposited F_6PEN molecules [197]. On the other hand, the formation of pentacene clusters is observed when depositing at RT, whereas similar arrangement patterns as for F_6PEN can be observed in certain domains [198]. At low coverage, the fully fluorinated perfluoropentacene forms no ordered structure on Cu(111) at RT and upon annealing to 423 K [141], whereby a densely packed structure is observed for monolayer and higher coverage [141, 199].

The determined lattice parameters using STM are $\vec{a} = 16.7\pm0.1$ Å, $\vec{b} = 7.5\pm0.1$ Å and $\gamma = 69.3\pm1$ ° (see Figure A.12), exhibiting an oblique unit cell. This matches relatively well with the lattice parameters determined in the same way for F_6PEN on Au(111) ($\vec{a} = 16.6\pm0.1$ Å, $\vec{b} = 7.5\pm0.1$ Å and $\gamma = 71.5\pm1$ °). However, upon examining the magnified, high-resolution STM image of the monolayer on Cu(111), shown in Figure 4.5 (e), it becomes evident that the molecules do not form a consistently uniform monolayer. Instead, they are positioned at defined distances with offsets across the surface. These offsets lead to a different packing motif of F_6PEN layers on Cu(111). The molecules form stacks

comprising two and three molecules with visible gaps between the stacks. These dimer and trimer structures are exemplified as orange and blue rectangles in Figure 4.5 (g). With the knowledge gained about the snap-in and the instability of the F_6PEN dimers, this suggests that individual molecules adsorb in a fixed position within the monolayer. Consequently, there may not be sufficient space for all molecules to rest in a stable position. Instead, some molecules may snap-in at a stable lattice site farther away, leading to a gap between the molecules. The F_6PEN monolayer on Cu(111) is additionally investigated using the chemical bond imaging method, as shown in Figure 4.6.

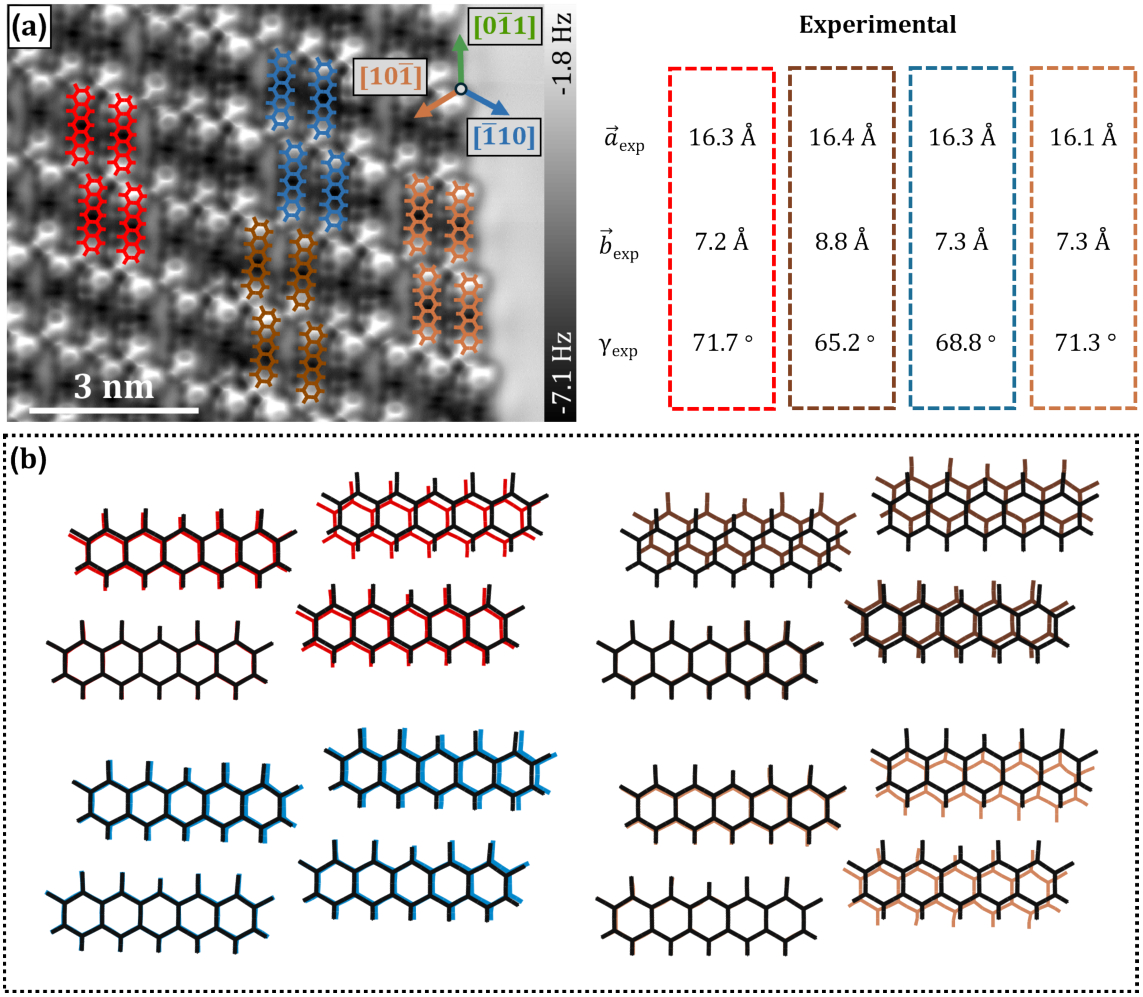


Figure 4.6: (a) cc-AFM image at the edge of a F_6PEN layer on Cu(111) ($T = 298\,\mathrm{K}$). Four tetramer structures are overlaid in red, brown, blue and orange color, respectively. The experimental lattice parameters are shown in dashed boxes with the same color code. (b) Superposition of the experimentally determined tetramer structures with the calculated crystal structure (black), presented in Figure 4.3 (a). Imaging parameters: (a) $V_g = 20\,\mathrm{mV}$, $I_t = 280\,\mathrm{pA}$.

Figure 4.6 (a) shows a high-resolution cc-AFM image of the F_6PEN monolayer on Cu(111), elucidating the sub-molecular structure and the precise packing motif of the molecules. Similar to Figure 4.5 (e), the image illustrates molecular stacking characterized by stack sizes of two and three molecules. Regions of brighter contrast, in comparison to the darker

regions observed at the center of the bent molecules, reveal the gaps between the molecule stacks. Four molecule tetramers (colored orange, blue, brown and red) are overlaid with the experimental AFM image, whereas orange, blue and red tetramers represent tetramers without visible gaps between them. The distances and angles determined for the respective dimer structures within the monolayer without gaps are 213 - 274 pm (mean = 243 pm, σ_d = 16) and 136 - 162 ° (mean = 148 °, σ_φ = 6). These are in the same order of magnitude compared to the dimers in different clusters on Au(111) and the dimer on Cu(111). Consequently, the H-F interactions for dimers in monolayers without gaps between them can be classified as Type A. In Figure 4.6 (a), a brown structure represents a tetramer in which the horizontally superimposed molecules have been fitted between one of the gaps. The length of the H-F interactions within the two dimer structures that compose the tetramer can be utilized to estimate the gap distance, which is found to range between 297 - 412 pm (mean = 353 pm, σ_d = 39). The angles of 142 - 179 ° (mean = 157 °, σ_φ = 13) follow the quasi-type I halogen bond with $\varphi_1 \approx \varphi_2$. However, compared to H-F interaction Type A, the distances differ by about 100 pm. Therefore, for molecules with gaps between them, a new H-F interaction type can be classified. In the following, this is referred to as Type D. In Figure 4.6 (b), experimental tetramer structures were aligned with the calculated structure (represented by the black tetramer) in such a way that the lower left molecules of the tetramers exactly match. The corresponding lattice parameters are highlighted by dashed boxes using the same color code, respectively. Upon examining the superimposed structures, it becomes evident that the orange, brown and red structures do not align well with the calculated structure. Obviously, this is particularly apparent in the case of the brown structure, in which the horizontally positioned molecules are separated by the gap between the molecule stacks. However, also structures which align almost perfectly with the calculated tetramer, such as the one represented in blue, can be observed. It is important to note that, unlike on Au(111), this does not imply that the molecules on the Cu(111) surface assimilate with the calculated structure within the monolayer, as the alignment of the structures does not follow a trend. The fact that the F_6PEN molecules do not interact without disturbance on the Cu(111) surface was discussed on the basis of several examples. This therefore indicates that the blue structure is a randomly matching superposition with the calculated structure.

4.2.3 Comparison of Molecular Bending on Au(111) and Cu(111)

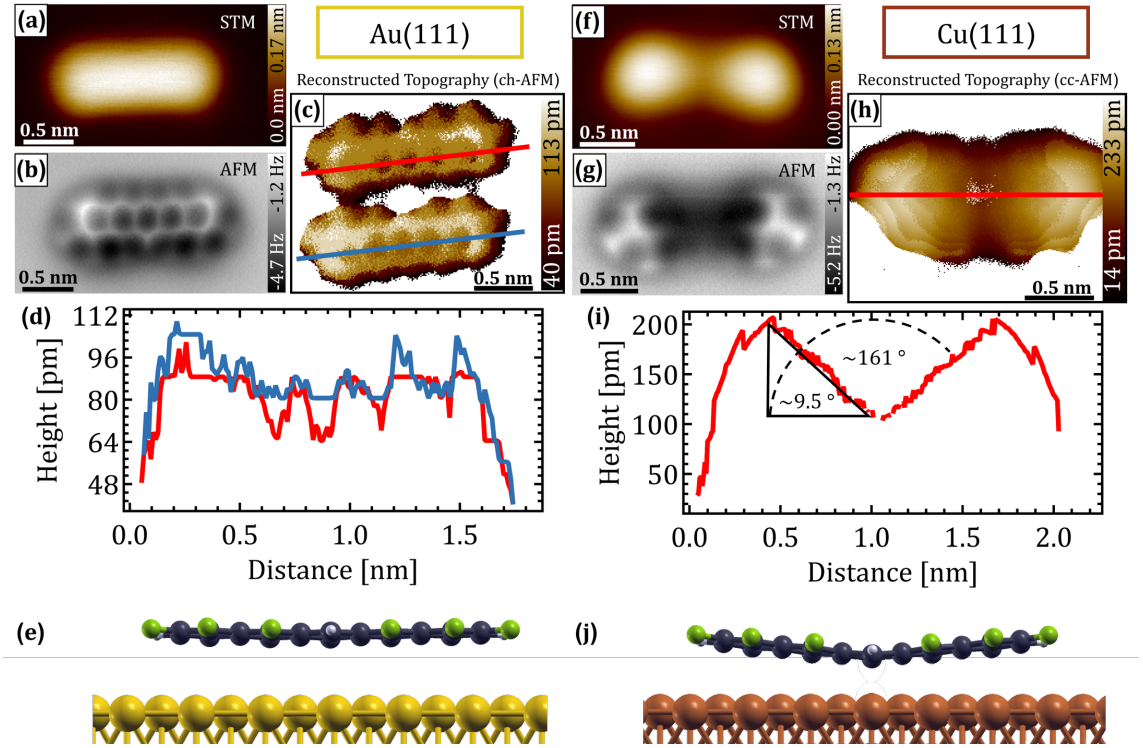


Figure 4.7: Comparison of the bending of F_6PEN on Au(111) and Cu(111). (a) STM and (b) ch-AFM image of a F_6PEN monomer on Au(111) ($T = 7\,\mathrm{K}$). (c) Reconstructed topography image of a F_6PEN dimer (ch-AFM) on Au(111). (d) Corresponding line profiles of the extracted topography image. (e) Sketch of a F_6PEN molecule adsorbing planar on the Au(111) surface. (f) STM and (g) ch-AFM image of a F_6PEN monomer on Cu(111) ($T = 7\,\mathrm{K}$). (h) Reconstructed topography image of a F_6PEN monomer (cc-AFM) on Cu(111). (i) Corresponding line profile of the extracted topography image. (j) Sketch of a F_6PEN molecule adsorbing non-planar on the Cu(111) surface. Imaging parameters: (a) $V_g = 100\,\mathrm{mV}$, $I_t = 10\,\mathrm{pA}$, (b) $\Delta z = -43\,\mathrm{pm}$ with respect to the STM setpoint of $V_g = -0.57\,\mathrm{mV}$, $I_t = 10\,\mathrm{pA}$, (f) $V_g = 100\,\mathrm{mV}$, $I_t = 10\,\mathrm{pA}$ and (g) $\Delta z = -100\,\mathrm{pm}$ with respect to the STM setpoint of $V_g = -0.57\,\mathrm{mV}$, $I_t = 10\,\mathrm{pA}$. Thanks to Daniel Martin-Jimenez for performing the data analysis on the molecular bending on Au(111) and Cu(111) and to Marvin Krenz for providing the molecular structures in Figure (e) and (j).

Finally, the bending of the F_6PEN molecules on Au(111) and Cu(111) is comparatively discussed. Figure 4.7 (a) and (b) show STM and ch-AFM images of a single F_6PEN molecule adsorbed nearly planar on Au(111), whereas Figure 4.7 (f) and (g) depict the adsorption structure of a monomer on Cu(111) using the same methods. A direct comparison of the ch-AFM images of the molecules distinctly reveals the bending of the molecule on Cu(111). While all five phenyl rings of F_6PEN are clearly resolved on the Au(111) surface due to the molecule's flat adsorption conformation, only the outer two rings are visible on Cu(111), leaving the central portion of the molecule unresolved.

An accurate determination of the adsorption geometry of molecules on surfaces can be either obtained by a grid-based approach, i.e. taking a force curve over each image pixel [119], or by acquiring a series of $\Delta f(x, y)$ images above the molecule at varying tip-sample separations Δz through sequential imaging [104]. The latter described method was performed in Figure 4.7. The adsorption conformation is determined from the reconstructed topography at the minimum of the experimental frequency shift versus distance curve, which corresponds to the transition from the attractive to the repulsive regime (see Figure 2.7 (d)) [108, 119]. For F_6PEN on Au(111), a sequence of images was recorded in constant height mode, whereby the frequency shift is acquired at a constant z-position, respectively. For the topography reconstruction on Au(111), a F_6PEN dimer was used, because individual molecules exhibit considerable mobility during scanning, due to the weak molecule-substrate interaction. The complete set of images recorded at different heights to generate the reconstructed topography image (see Figure 4.7 (c)) is shown in Figure A.13. The white areas in the reconstructed topography images correspond to image sections where the transition point of the force curve was not reached due to large tip-sample distances. The line profiles associated with the two molecules, which are presented in the reconstructed topography image, are plotted in Figure 4.7 (d). These reveal only marginal height differences of the F_6PEN molecules adsorbed on Au(111), therewith confirming the nearly planar adsorption geometry. A side view of the molecule on the Au(111) surface is sketched in Figure 4.7 (e).

For F_6PEN on Cu(111), imaging in constant height mode poses a challenge due to the concave bending of the molecule, whereby the center cannot be fully resolved, because of the large tip-sample separations. However, close tip-sample distances can lead to tip damages (e.g. loss of the CO tip) or lateral manipulation of the molecule. Therefore, in the case of F_6PEN on Cu(111), the constant current AFM mode was utilized to get access to the reconstructed topography data. Unlike the sequence of images gathered in constant height mode, it needs to be taken into account that the constant current mode does not yield equidistant z-values for each x- and y-position, because the tip follows the topography of the molecule [104]. The STM and frequency shift images used to reconstruct the topography image (see Figure 4.7 (h)) are gathered in Figure A.14. The corresponding line profile is presented in Figure 4.7 (i), further revealing that the molecule is adsorbing in a v-shape on the surface with a determined angle of about 161 °. This configuration exhibits a height difference of around 90 pm from the lower center to the higher sides of the molecule. A side view of the bent structure on Cu(111) is depicted in Figure 4.7 (j). As derived by density functional theory, the interaction of the Cu(111) substrate with pentacene and fully fluorinated pentacene leads to bending angles of approximately 177 ° and 167 °, respectively [200].

The bending of the center of the molecule is also commonly observed for regular pentacene molecules on reactive metal substrates such as Cu(111) [16, 119, 197, 200, 201], Cu(110) [202, 203], Al(001) [204] and Pt(111) [205]. The adsorption geometry of molecules on metal surfaces is thereby in general closely linked to the electronic properties of the adsorbate and the molecule-substrate interaction [119, 206]. For example, in the case of regular pentacenes, a transition from physisorption to chemisorption is observed when comparing the adsorption behavior of the molecules on Au(111) with that on more reactive Ag(111) and Cu(111) surfaces [207]. Ugolotti et al. explain the bending of the pentacene with a chemisorption of the molecule to the highly reactive Pt(111) substrate [205]. The exact lattice

adsorption site of the molecules on the respective surface also appears to play a significant role. Baby et al. report a direct anchoring of the central carbon atoms of the pentacene to the perfectly matching bridge sites of the Al(001) surface. For pentacene on Al(001), this leads to an opening angle of approximately 155 °, as derived from density functional theory calculations [204]. The anchoring of the molecule is thereby usually observed in the center of the pentacene structures, since the central phenyl rings have proven to be the most reactive ones in acene structures [208, 209]. This leads to the commonly observed concave v-shape of the adsorbed molecules on reactive surfaces, as depicted in Figure 4.7. However, not only the substrate, but also the functionalization of the molecules affects the exact adsorption geometry. In the specific case of the substitution of hydrogen by fluorine atoms in pentacene molecules, the stronger repulsion between the fluorine and the copper surface atoms results in an increased adsorption height of the fluorine atoms compared to the hydrogen atoms [193, 201]. In case of the pentacene molecule on Cu(111), a transition from gentle bending to sharp bending is therefore observed upon full fluorination [200].

4.3 Summary

In summary, the unique self-assembly mechanism of unilaterally fluorinated F_6PEN was used to investigate H-F interactions on inert Au(111) and reactive Cu(111) substrates. On Au(111), the molecules gradually form larger clusters and dense layers upon sample annealing. The cluster formation was exploited to investigate H-F interactions in different interaction environments. The chemical bond imaging measurements reveal that the arrangements of H-F interactions in the changing interaction environments mainly remain the same, whereas differences are observable inside of densely packed layers. In contrast, the interaction of the molecules on Cu(111) is not mainly dominated by the intermolecular attraction, but significantly influenced by the molecule-substrate interaction. As a result, dimer and trimer stacks with noticeable gaps between them can be observed in packed layers of molecules on Cu(111). Additionally, the stronger interaction of F_6PEN with the Cu(111) surface leads to a noticeable bending in the center of the molecules. In total, four different H-F interaction types could be revealed by chemical bond imaging. These include interactions of dimers in varying cluster sizes and layers on Au(111) as well as dimers and packed layers on Cu(111) (Type A) and interactions of neighboring molecules in densely packed layers on Au(111) that show in the same direction (Type B). Further, interactions of neighboring molecules on Au(111) that point in different directions (Type C) and H-F interactions of molecules in layers on Cu(111) with a gap between them (Type D) are observed. In conclusion, our results reveal that the attractive H-F interaction is a powerful tool to steer self-assembly processes in the sub-monolayer regime. While on Cu(111), an interaction of the precursors with the underlying substrate has to be taken into account, the self-assembly on Au(111) is mainly driven by intermolecular interactions.

5 Temperature Induced On-Surface Ring-Opening Polymerization Reaction for the Synthesis of Nanoribbons: Strain Influence of Cycloparaphenylenes

5.1 Introduction

Due to the unique electronic properties of tailored non-benzenoid and benzenoid carbon nanoribbons, they are promising candidates for the integration into electronic devices. However, given that the electronic properties of such nanoribbons depend on their width, along with the challenges associated with synthesizing non-benzenoid carbon nanostructures, there is a need for reliable on-surface synthetic strategies to produce benzenoid and non-benzenoid carbon nanoribbons of defined sizes (see Section 2.5). A promising intermediate for the synthesis of carbon nanoribbons are poly(*para*-phenylene) (PPP) chains, which consist of covalently linked phenyl units in para-position. In recent studies, it was demonstrated that benzenoid armchair graphene nanoribbons of different widths can be synthesized on-surface by the fusion of PPP intermediate species. However, in these studies, the PPP chains were synthesized using a halogenated 4,4"-dibromo-p-terphenyl precursor via an Ullmann coupling reaction step [210, 211, 212]. As explained in Section 2.5.1, the outcome of the Ullmann reaction using halogenated precursors can be difficult to predict, since the self-assembly mechanism as well as the formed products can depend on the halogen functionalization and the surface on which the reaction is performed. This can also be observed when PPP chains are synthesized on different surfaces using halogenated precursors. On reactive substrates, such as Cu(111) [213] and Ag(111) [212, 214], cleaved halogen atoms adsorb on the surface and might inhibit the precursor interaction and PPP chain growth. For example, using 4,4"-dibromo-p-terphenyl as a precursor on a less reactive Au(111) substrate will result in mostly 70 nm long PPP chains [211]. However, when using the same precursor on a reactive Cu(111) surface, significantly shorter PPP chains are observed [213, 215]. The decreased length of the PPP chains on Cu(111) might be attributed to the disturbing interaction of adsorbed halogen atoms on the surface. As explained in Section 2.4, the self-assembly process of molecules on surfaces is governed by the complex interplay of molecule-substrate and molecule-molecule interactions, making it difficult to predict the outcome of self-assembly as well as nanoribbon formation processes. For example, for the same 4,4"-dibromo-p-terphenyl precursor, different self-assembly patterns are observed on Cu(111) [213] and Au(111) [211] substrates. To address the complexities of the Ullmann coupling, as well as the challenges associated with the prediction of self-assembly mechanisms of halogenated precursors, there is an increasing demand for halogen-free precursors in on-surface reactions.

One example for such halogen-free precursors are cycloparaphenylenes ((*n*)CPP, $[C_6H_4]_n$), which represent single units of an armchair carbon nanotube (CNT). CPPs belong to a class of aromatic hydrocarbon belts with a number of *n* phenyl rings connected via covalent bonds in para-position, forming a closed hoop [216, 217]. The first set of (*n*)CPPs (*n* = 9, 12, 18) was synthesized in 2008 by Jasti et al. [218]. To date, the synthesis of many different ring sizes was achieved using various synthetic strategies [219, 220, 221]. One of the key parameters that distinguishes CPPs of different sizes is their ring internal strain energy, which generally decreases with increasing ring sizes ((6)CPP: 401.7 kJ mol^{-1} vs. (20)CPP: 118.8 kJ mol^{-1}) [222]. In a recent study of our group, it was demonstrated that ultra-long PPP chains with lengths of 0.9 µm can be synthesized on Cu(111) using a halogen-free (6)Cycloparaphenylene precursor by exploiting the ring internal strain of the highly strained circular molecule in a ring-opening polymerization (ROP) reaction. The fusion of adjacent PPP chains upon annealing leads to the formation of graphene (GNR) and biphenylene (BNR) nanoribbons [131].

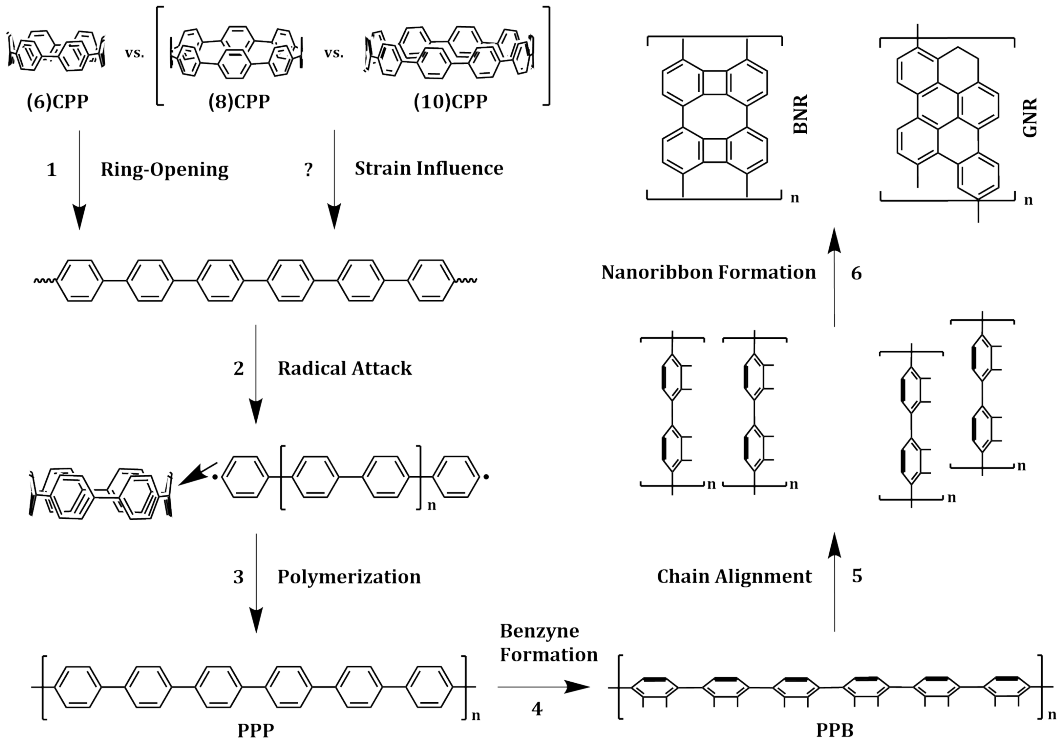


Figure 5.1: Overview of the temperature induced reaction mechanism of (6)Cycloparaphenylene on a Cu(111) surface.

An overview of the reaction using (6)CPP, established in Ref. [131], is shown in Figure 5.1. The temperature induced ring-opening of (6)CPP defines the start of the ROP (Step **1**). Radicals formed at the ends of the opened CPPs attack intact molecules (Step **2**) and subsequently form long poly(*para*-phenylene) chains on the surface (Step **3**). Upon further annealing, the PPP chains convert into poly(*para*-benzyne) (PPB) chains, forming covalent bonds to the copper substrate after (partly) dehydrogenation of the phenyl units (Step **4**). The pre-step of the nanoribbon formation (Step **6**), the chain alignment (Step **5**), determines if a graphene nanoribbon or biphenylene nanoribbon is formed.

However, this newly introduced reaction of the halogen-free (6)CPP precursor is generally not well understood yet and needs to undergo further investigation. Additionally, as the OSS is a new field of research, general comprehensive studies of reaction mechanisms are required to build a solid fundamental knowledge. Therefore, in this chapter, we systematically investigate the influence of the ring size and strain on the feasibility of the on-surface synthesis of carbon nanoribbons by utilizing a set of different sizes of cycloparaphenylenes ((6)CPP vs. (8)CPP vs. (10)CPP). The subsequently heated samples are analyzed using low temperature scanning tunneling microscopy. Intermediates as well as products are resolved by chemical bond imaging with CO-functionalized tips. Our investigations show that the feasibility of the reaction strongly depends on the ring size and ring strain. While an almost complete polymerization of precursors is observed for (6)CPP, only partial or no polymerization occurs for the larger counterparts (8)CPP and (10)CPP. The ring-opening, being the decisive step of the polymerization reaction, is found to strongly depend on the ring size and strain of the CPP molecules, whereby the ratio of unopened rings on the surface increases for less strained, larger rings. For (8)CPP, this leads to a lower yield of nanoribbons compared to (6)CPP, because unopened, immobile (8)CPP molecules disturb the chain alignment and nanoribbon formation and cannot contribute to the ROP. For (10)CPP, almost no ring-opening is observed, leading to no ordered product.

5.2 Results and Discussion

5.2.1 (6)CPP - Overview

A brief overview of the experimental results from the reaction of (6)CPP on Cu(111) is presented in the STM images in Figure 5.2 for three representative temperatures. Additional information on further temperatures can be found in Figure B.1. Note that all STM and AFM images were taken at cryogenic temperatures of approximately 5.2 K. At room temperature (see Figure 5.2 (a)), the (6)CPP molecules remain intact and form large layers with upright standing molecules on the Cu(111) surface. At 353 K, the first (6)CPPs start to open (see Figure 5.1, Step **1**), leading to a formation of radicals at the opened chain ends, which can attack intact molecules (see Figure 5.1, Step **2**). This results in a formation of poly(*para*-phenylene) chains of lengths of over 80 nm (see Figure B.1 (a) and (b)). Upon sample annealing to 523 K (see Figure 5.2 (b)), the ring-opening polymerization continues, which results in long and ordered PPP chains (see Figure 5.1, Step **3**) of lengths up to 0.9 µm [131]. Large islands of unreacted (6)CPP can still be found at temperatures of up to 523 K (see Figure B.1 (c) and (d)). Figure 5.2 (b) shows an overview STM image of the highly ordered, separated PPP chains. No interconnections between PPP chains can be observed at temperatures of up to 523 K (see Figure 5.2 (b), zoom-in).

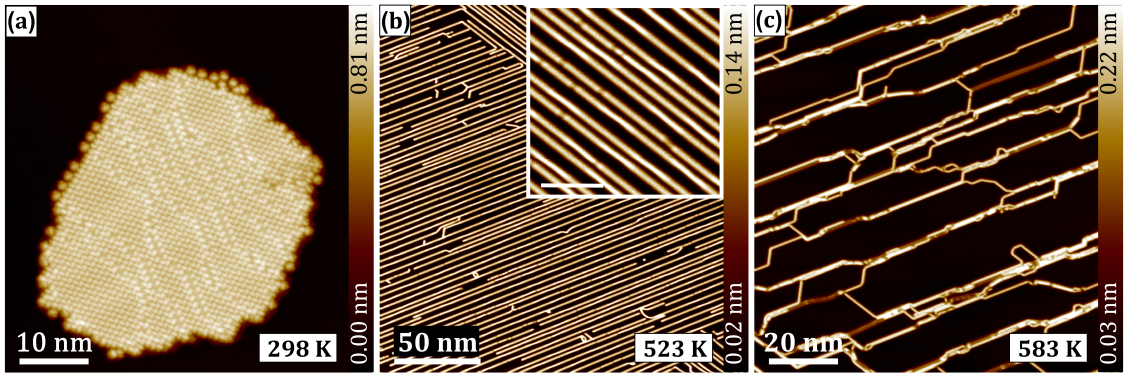


Figure 5.2: Overview of the reaction of (6)CPP on Cu(111). STM images are taken after subsequent sample annealing to (a) $T = 298$ K, (b) $T = 523$ K and (c) $T = 583$ K. Imaging parameters: (a) $V_g = 100$ mV, $I_t = 5$ pA, (b) $V_g = 100$ mV, $I_t = 5$ pA (scale bar in zoom-in: 12.5 nm) and (c) $V_g = 100$ mV, $I_t = 5$ pA. Thanks to Qigang Zhong for conducting the experiments of (6)CPP on Cu(111).

Further annealing of the surface leads to a dehydrogenation reaction of the phenyl units in the PPP chains, resulting in PPB chains that form covalent bonds between the phenyl rings and the Cu(111) surface (see Figure B.1 (e) and Figure 5.1, Step **4**). The fusion of single adjacent PPB chains results in the formation of biphenylene and graphene nanoribbons (see Figure 5.2 (c) and Figure 5.1, Step **6**). Which of the two products is formed depends on the respective arrangement of individual neighboring PPB chains (see Figure 5.1, Step **5**). A face-to-face orientation of the benzynes will result in the formation of biphenylene nanoribbons, whereas a shift of one PPB chain by 0.5 unit cells leads to

the formation of graphene nanoribbons. Usually, two neighboring chains will react with each other, forming six atom wide armchair graphene nanoribbons (6-AGNR) and six atom wide biphenylene nanoribbons (6-BNR). For simplicity, throughout this results section the ribbons are referred to as biphenylene (BNR) and graphene (GNR) nanoribbons. When the sample is further heated to 633 K (see Figure B.1 (f)), the portion of neighboring PPB chains transforming into nanoribbons increases [131].

5.2.2 (8)CPP - Overview

Now we focus on the effect of the ring strain by performing similar studies with (8)CPP and (10)CPP and compare the results to those of (6)CPP. The overview of the on-surface reaction process of (8)CPP on Cu(111) is shown in Figure 5.3. At RT, (8)CPP forms multilayers on the Cu(111) surface. Single (8)CPP molecules within the layers seem to be highly mobile, leading to tip changes and image contrast distortions in the STM images (see Figure B.2 (a)). The multilayers are stable up to temperatures of at least 383 K (see Figure B.2 (b)) and consist of up to three (8)CPP molecule layers (see Figure B.3).

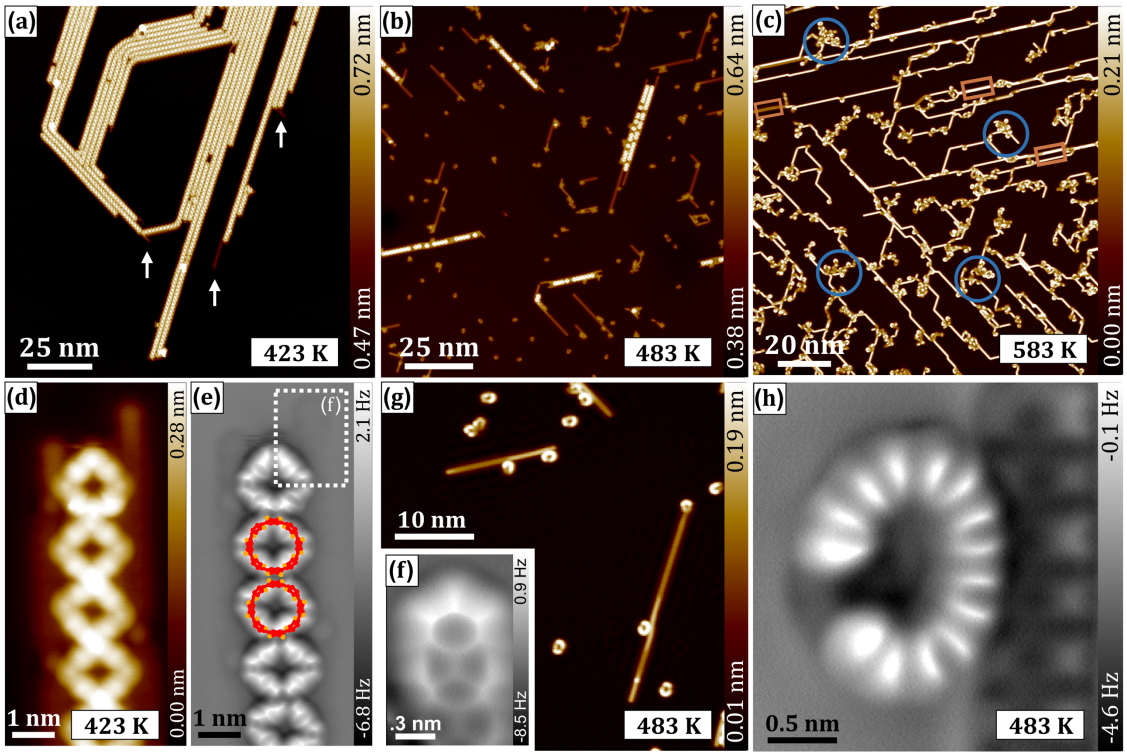


Figure 5.3: Overview of the reaction of (8)CPP on Cu(111). Upper row: STM images taken after subsequent sample annealing to (a) $T = 423\,\mathrm{K}$, (b) $T = 483\,\mathrm{K}$ and (c) $T = 583\,\mathrm{K}$. Lower row: Magnified STM and cc-AFM images to further describe the reaction mechanism. (d) STM and (e) cc-AFM image of five (8)CPP molecules enclosed by PPP chains ($T = 423\,\mathrm{K}$). (f) cc-AFM image of a PPP chain termination (see box in subfigure (e)). (g) STM image of PPP chains and separated (8)CPP molecules ($T = 483\,\mathrm{K}$). (h) cc-AFM image of an (8)CPP aligning to a PPP chain ($T = 483\,\mathrm{K}$). Imaging parameters: (a) $V_\mathrm{g} = 100\,\mathrm{mV}$, $I_\mathrm{t} = 10\,\mathrm{pA}$; the sample was annealed for 50 min instead of 30 min, (b) $V_\mathrm{g} = 100\,\mathrm{mV}$, $I_\mathrm{t} = 10\,\mathrm{pA}$, (c) $V_\mathrm{g} = 100\,\mathrm{mV}$, $I_\mathrm{t} = 10\,\mathrm{pA}$; molecules were evaporated for 2.5 min instead of 2 min, (d) $V_\mathrm{g} = 100\,\mathrm{mV}$, $I_\mathrm{t} = 10\,\mathrm{pA}$, (e) $V_\mathrm{g} = 50\,\mathrm{mV}$, $I_\mathrm{t} = 12\,\mathrm{pA}$, (f) $V_\mathrm{g} = 20\,\mathrm{mV}$, $I_\mathrm{t} = 200\,\mathrm{pA}$, (g) $V_\mathrm{g} = 100\,\mathrm{mV}$, $I_\mathrm{t} = 10\,\mathrm{pA}$ and (h) $V_\mathrm{g} = 50\,\mathrm{mV}$, $I_\mathrm{t} = 100\,\mathrm{pA}$.

The observation of multilayers on Cu(111) is in contrast to findings for (8)CPP on Au(111) and Ag(111) surfaces, where monolayers of flat-lying molecules were reported [223]. This indicates a different molecule-substrate interaction compared to Cu(111). For a less reactive graphite substrate, as predicted by calculations, the flat-lying adsorption conformation also seems to be the energetically most favorable one [224]. For additional discussion on multilayers of (8)CPP on Cu(111) see Figure B.3. Annealing the sample to 423 K results in two important events: The multilayers on the surface convert to monolayers, with (8)CPP molecules adsorbing in a flat-lying configuration with molecule openings pointing upwards. In addition, the ring-opening reaction starts and some PPP chains can be found next to rows of intact (8)CPP molecules, highlighted by white arrows in Figure 5.3 (a). Upon further sample annealing to 483 K (see Figure 5.3 (b)), the molecular layers will segregate, forming smaller clusters with intact (8)CPP molecules. Also, single separated PPP chains with lengths of up to 25 nm as well as, for the first time, single (8)CPP molecules can be observed, which either adsorb fully separated or next to PPP chains. This finding is in stark contrast compared to the reaction pathway of (6)CPP, where the great majority of molecules at 523 K can either be found in islands of intact molecules or in the form of opened, ordered PPP chains. For (8)CPP, some PPP chains with lengths of at least 80 nm can be found as well at temperatures of 523 K, but the number of chains is lower compared to (6)CPP. Furthermore, some single unopened molecules are adsorbed between the PPP chains (compare Figure 5.2 (b) vs. Figure B.2 (d)). First benzyne formation in PPP chains occurs at 543 K (see Figure B.2 (e)), corresponding well with the temperature for the benzyne formation in PPP chains observed for (6)CPP. The benzyne formation is indicated by bright protrusions appearing within PPP chains in STM images. For more information see Figure B.4. Figure 5.3 (c) shows the sample after annealing to 583 K. A distinction can generally be made between three different species: 1. PPB chains which did not fuse with neighboring chains to form nanoribbons, 2. Randomly reacted, unopened (8)CPPs, which disturb the PPB chain alignment and fusion (highlighted by blue circles) and 3. Some nanoribbons consisting of two fused PPB chains (highlighted by orange rectangles). The products of the chain fusion will be discussed later in Figure 5.8.

The origin of the unreacted species disturbing the alignment of the PPP chains in the case of the on-surface reaction of (8)CPP will be discussed in the following, by comparing some remarkable differences in the reaction pathways of (6)CPP and (8)CPP. While in the case of (6)CPP almost only intact precursors within islands and opened molecules (PPP chains) can be found, (8)CPP molecules do also form chains and narrow sheets of flat-lying molecules upon annealing to 423 K (see Figure 5.3 (a)). Further insight into the adsorption conformation of an (8)CPP molecule chain is given in Figure 5.3 (d). The STM image shows a row of five flat-lying (8)CPP molecules, characterized by a bright contrast, that are surrounded by PPP chains. The structure is further investigated using constant current AFM measurements (see Figure 5.3 (e)). Two (8)CPP structures are overlaid in the AFM image to indicate the orientation of the molecules. Carbon atoms are shown in red, whereas hydrogen atoms are shown in orange color. The chain termination of a PPP chain surrounding the (8)CPP molecules is resolved in Figure 5.3 (f). The determined size of the adsorbed (8)CPP molecules in Figure 5.3 (e) matches well with the size of the molecule in the gas phase (see Figure B.5). However, instead of having a circular shape, the intact (8)CPP molecules have a square-shaped appearance in the AFM image. This can be rationalized by the alternate twisting of the phenyl units, as discussed in Figure 5.5.

As already observed in Figure 5.3 (b), some single separated (8)CPP molecules can be found on the surface after annealing to 483 K. The STM image in Figure 5.3 (g) reveals that the single rings can adsorb fully separated on the Cu(111) surface or attach next to opened PPP chains. To further elucidate the adsorbed structures, an (8)CPP molecule aligning to a PPP chain is investigated by constant current AFM imaging. The structure of the (8)CPP as well as the PPP chain can be resolved in a single constant current AFM image (see Figure 5.3 (h)). When comparing the (8)CPP molecules in Figure 5.3 (e) and (h), two significant differences in the appearance of the structures can be observed: 1. The (8)CPP ring in Figure 5.3 (h) is not square-shaped, but appears as an oval molecule and 2. The ring contains a dark spot at the left side. The difference in the appearance of the molecules is presumably caused by dehydrogenation of the phenyl rings at the bottom side, leading to benzyne formation and bonding to surface atoms, which is accompanied by a strong reduction of the twisting angles of the phenyl units (see discussion in Figure 5.5). The dark spot can be rationalized by a single twisted phenyl ring, which has not lost its hydrogens. In case of (6)CPP, where the ring-opening already starts at approximately 350 K, a loss of hydrogens in intact rings is not observed and does not seem to hamper the ROP. Even at high temperatures between 543 - 633 K (see Figure B.2 (e) and (f)), unopened (8)CPPs can be found. These unopened rings randomly react with each other as well as with PPP chains, forming unordered structures (blue circles in Figure 5.3 (c)). The unordered structures partly hinder the nanoribbon formation and lead to a lower yield compared to (6)CPP (compare Figure 5.2 (c) vs. Figure 5.3 (c)).

5.2.3 (10)CPP - Overview

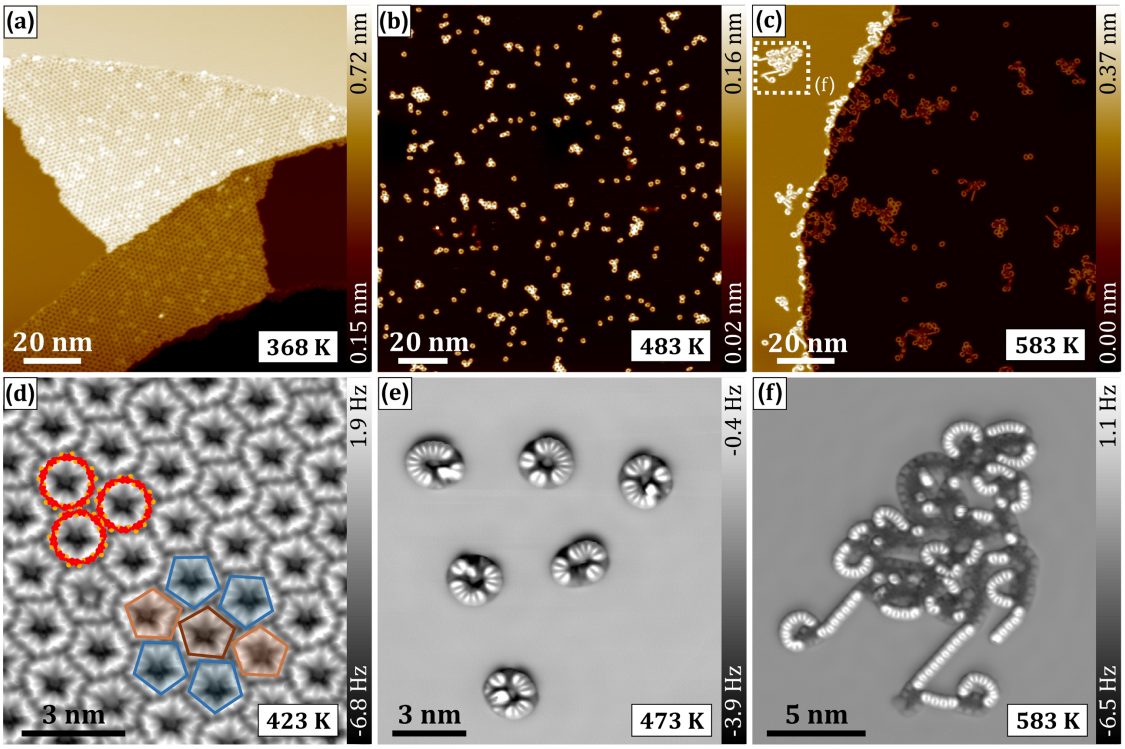


Figure 5.4: Overview of the reaction of (10)CPP on Cu(111). Upper row: STM images taken after subsequent sample annealing to (a) $T = 368\,\mathrm{K}$, (b) $T = 483\,\mathrm{K}$ and (c) $T = 583\,\mathrm{K}$. Lower row: cc-AFM images that further describe the reaction mechanism: (d) (10)CPP molecules forming a monolayer on the surface ($T = 423\,\mathrm{K}$). (e) Six separated (10)CPP molecules with round shapes ($T = 473\,\mathrm{K}$). (f) Unopened (10)CPP rings forming unordered agglomerates ($T = 583\,\mathrm{K}$). Imaging parameters: (a) $V_\mathrm{g} = 100\,\mathrm{mV}$, $I_\mathrm{t} = 5\,\mathrm{pA}$, (b) $V_\mathrm{g} = 100\,\mathrm{mV}$, $I_\mathrm{t} = 10\,\mathrm{pA}$, (c) $V_\mathrm{g} = 100\,\mathrm{mV}$, $I_\mathrm{t} = 10\,\mathrm{pA}$, (d) $V_\mathrm{g} = 100\,\mathrm{mV}$, $I_\mathrm{t} = 23\,\mathrm{pA}$, (e) $V_\mathrm{g} = 100\,\mathrm{mV}$, $I_\mathrm{t} = 150\,\mathrm{pA}$ and (f) $V_\mathrm{g} = 50\,\mathrm{mV}$, $I_\mathrm{t} = 140\,\mathrm{pA}$.

Further explanation on the strain influence of the CPPs can be derived when comparing the on-surface polymerization of (6)CPP and (8)CPP to an even larger (10)CPP molecule. An overview of the on-surface reaction of (10)CPP is given in Figure 5.4. Compared to (8)CPP, (10)CPP exclusively forms layers with flat-lying molecules (see Figure 5.4 (a)). These layers can be observed after annealing to room temperature (see Figure B.6 (a)). No significant change in the molecule configuration can be found up to temperatures of 423 K (see Figure B.6 (b)). The (10)CPP molecules will start to separate from the monolayers at temperatures between 423 K and 473 K (see Figure B.6 (c)). An overview STM image of single (10)CPP molecules and small molecular clusters is shown in Figure 5.4 (b). These single molecules and clusters are stable up to temperatures of at least 553 K (see Figure B.6 (d) and (e)) and will form unordered structures when further annealing the sample to 583 K, as shown in Figure 5.4 (c). The constant current AFM images in Figure 5.4 (d) - (f) give additional insight into the reaction process of (10)CPP. Figure 5.4 (d) shows

a (10)CPP molecule layer with flat-lying molecules appearing in a pentagonal shape. The determined size of the molecule on the surface matches well with the molecule in the gas phase (see Figure B.7). As for the (8)CPP molecules, the pentagonal shape of the (10)CPP molecules can be explained using AFM image simulations derived from the probe particle model (see discussion in Figure 5.5).

The (10)CPP rings form an ordered, quasi-hexagonal lattice. An example of a hexagonal lattice subunit formed by six pentagon-like structures is shown in Figure 5.4 (d). Four of the molecules are edge-edge linked (blue pentagons) to the central molecule (brown pentagon), whereas two molecules are edge-corner linked (orange pentagons), respectively. Further, three molecular structures are overlaid in the experimental AFM image to indicate the orientation of the orange hydrogen atoms. Figure 5.4 (e) shows a cc-AFM overview image of six (10)CPP molecules after annealing to 473 K. Compared to the (10)CPP molecules in Figure 5.4 (d), all imaged molecules have circular to oval shapes and resemble the simulated AFM image contrast of the structure without tilted phenyl rings. For more information see Figure 5.5. As in the case of (8)CPP, this indicates that most of the phenyl rings undergo a dehydrogenation reaction starting at a temperature between 423 - 473 K (compare Figure B.6 (b) and (c)). It seems like none of the six (10)CPP molecules fully lost their hydrogen atoms at the bottom side, as each of the rings show some bright features stemming from hydrogens pointing upwards and darker spots that are caused by intact phenyl rings that are considerably twisted. At this point, it is also noteworthy that opened (10)CPP rings cannot be found on the surface up to temperatures of 483 K and that most of the carbon rings of the adsorbed unopened (10)CPP molecules are found in an upright standing position (i.e. partially lost their hydrogen atoms). One exemplary structure that forms after annealing the sample to 583 K is resolved in the cc-AFM image in Figure 5.4 (f). The image shows a disordered aggregation of opened and unopened molecules, forming covalent bonds to adjacent adsorbed structures. The opened CPPs are randomly integrated into the structure, but do not form ordered nanoribbons.

5.2.4 Probe Particle Model Simulations of (8)CPP and (10)CPP

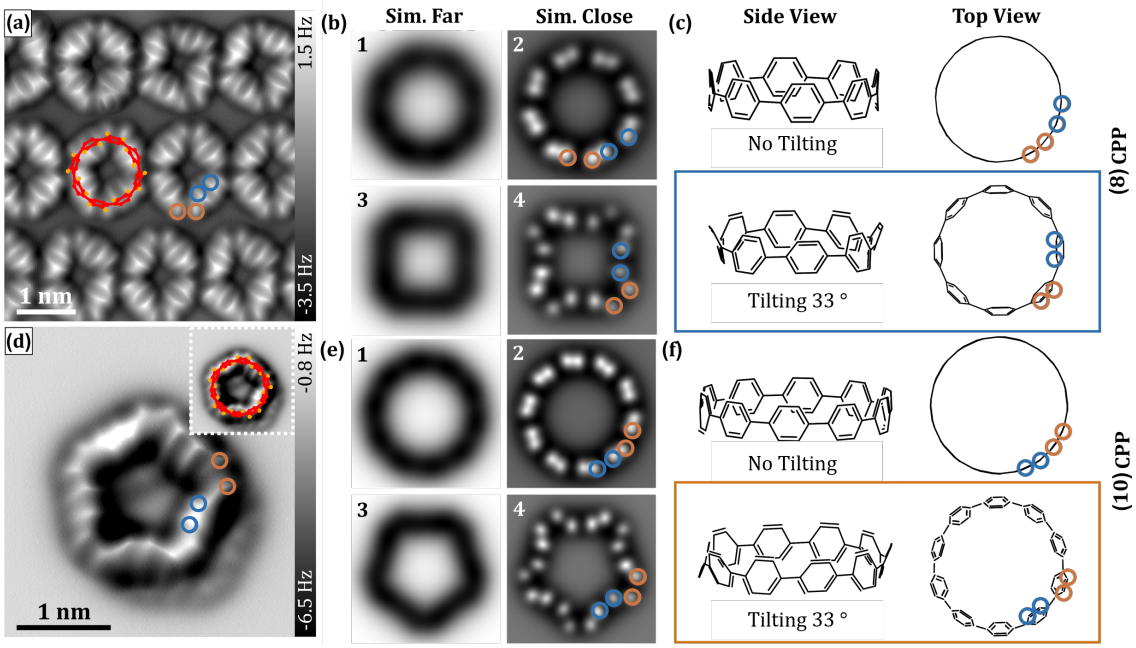


Figure 5.5: Probe particle model ch-AFM image simulation to decipher the adsorption geometry of (8)CPP and (10)CPP on Cu(111). (a) cc-AFM image of flat-lying (8)CPP molecules forming a layer ($T = 463\,\mathrm{K}$). (b) Simulated ch-AFM images for the structures shown in section (c). Left column: Far tip-sample distances. Right column: Close tip-sample distances. (c) Upper structure: (8)CPP without tilted phenyl rings (simulation b1, b2). Lower structure: (8)CPP with alternately tilted (∼33 °) phenyl rings (simulation b3, b4). Left column: Side view. Right column: Top view. (d) ch-AFM image of an isolated (10)CPP molecule ($T = 7\,\mathrm{K}$). The inset shows the same image with an overlaid molecule structure. (e) Simulated ch-AFM images for the structures shown in section (f). Left column: Far tip-sample distances. Right column: Close tip-sample distances. (f) Upper structure: (10)CPP without tilted phenyl rings (simulation e1, e2). Lower structure: (10)CPP with alternately tilted (∼33 °) phenyl rings (simulation e3, e4). Left column: Side view. Right column: Top view. Imaging parameters: (a) $V_\mathrm{g} = 50\,\mathrm{mV}$, $I_\mathrm{t} = 8\,\mathrm{pA}$ and (d) $\Delta z = +105\,\mathrm{pm}$ with respect to the STM setpoint of $V_\mathrm{g} = -0.57\,\mathrm{mV}$, $I_\mathrm{t} = 15\,\mathrm{pA}$.

To explain the unexpected shape of the (8)CPP and (10)CPP molecules on the surface and rule out the possibility that the investigated structures are molecules that have decayed in an unintended manner, constant height AFM images were simulated using the probe particle model [108, 225]. Figure 5.5 (a) shows the constant current AFM image of (8)CPP at higher temperatures of 463 K and in larger islands. Compared to Figure 5.3 (e) (T = 423 K), the molecules have the same square-shaped appearance, excluding that the unexpected shape is only occurring at certain temperatures or in particular interaction environments. To determine the reason for the square-shaped appearance of the (8)CPP molecules in the AFM images, two different molecular configurations were simulated using the probe particle model. Initially, the constant height AFM images were simulated with

an (8)CPP molecule structure with non-tilted phenyl rings. In the simulated images for far and close tip-sample distances (see Figure 5.5 (b1) and (b2)), the molecules show an expected circular-shaped appearance with eight hydrogen pairs pointing upwards (two pairs are highlighted by two blue and orange circles, respectively). When AFM images are simulated with phenyl rings that are tilted alternately (dihedral angles of $\sim$33 °), the appearance of the simulated molecule changes. The squared shape can already be anticipated at far tip-sample distances (see Figure 5.5 (b3)) and becomes more prominent at closer tip-sample distances, with four hydrogen pairs pointing towards the center of the molecule and four hydrogen pairs pointing outwards, correspondingly (see Figure 5.5 (b4)). These results suggest that the molecules on the surface behave similarly to molecules in the gas phase, where neighboring hydrogens repel each other, causing phenyl rings to be tilted alternately. Note that a tilt of $\sim$33 ° in an all-alternating conformation was chosen for simulations, because by density functional theory calculations it was determined to be the most stable structure of (12)CPP. Further, all-alternating conformations were in general determined to be the most stable ones for even number (n)CPPs (n = 6 - 12) [222].

The oval appearance of the molecules that begins to emerge at higher temperatures can also be explained with the aid of the probe particle model. For intact (8)CPP, the repulsion of the hydrogen atoms leads to tilted phenyl rings and a squared appearance in the experimental and simulated AFM images. However, the tilt is no longer present after annealing the surface at a temperature between 423 K and 473 K (first separated, round rings can be spotted at 473 K (see Figure B.2 (c))). Since the tilting of the phenyl rings, which has been associated with the hydrogen repulsion, can no longer be observed, it indicates that a dehydrogenation reaction may have taken place. Consequently, the (8)CPP molecules without tilted phenyl rings lead to a molecule appearance in the experimental AFM image that resembles the one of the probe particle model simulations in Figure 5.5 (b1) and (b2). This suggests that benzyne formation occurs within intact (8)CPP molecules and phenyl rings will form covalent bonds to the sample surface, leading to upright standing benzyne rings. Note that only seven of the eight phenyl rings of the (8)CPP molecule in Figure 5.3 (h) have lost their hydrogen atoms at the bottom side, whereas one hydrogenated ring seems to be rotated parallel to the surface and cannot be seen in the AFM image. The contrast of the AFM images of the benzyne rings within the (8)CPP molecule also matches that of the PPB chains [131] (compare to Figure 5.8 (d)). In the constant current AFM images, the single benzynes have a halo-like appearance. In contrast, in the constant height AFM image, two bright protrusions show up per benzyne ring (see Figure B.8), matching well with the appearance of the simulated and experimental constant height AFM images [226]. As for (8)CPP, a simulated (10)CPP molecule structure without tilting appears as a circular molecule in the probe particle model simulations in Figure 5.5 (e1) and (e2). When tilting the phenyl rings alternately in the simulated structure by $\sim$33 °, the appearance of the molecule in the simulated AFM image will change. As marked by blue and orange circles, two hydrogens per phenyl ring will alternately point towards and outwards the center, leading to the pentagonal appearance. The square-shaped and pentagonal adsorption geometries of (8)CPP and (10)CPP, due to the alternate tilting of the phenyl rings, correspond well with the observation that (12)CPP adsorbs in an apparent hexagonal structure on Cu(100), as derived by combined STM and tip-enhanced Raman spectroscopy investigations. However, the substrate type and orientation seems to have a major influence on the adsorption geometry of CPPs, because (12)CPP shows a twisted arrangement on Ag(110) [227].

5.2.5 Investigation of Intermediates and Products

As explained in the previous section, although the two processes of ring-opening and hydrogen loss in intact molecules compete in the on-surface synthesis using (8)CPP, long PPP chains can be found, which can react with each other to form nanoribbons. In the following, PPP chains formed by opened (8)CPP molecules and their formation process will be further investigated using high-resolution AFM imaging. Figure 5.6 (a) shows a 13 nm long section of a poly(*para*-phenylene) chain on the Cu(111) substrate. The two different contrasts in the upper and lower sections of the PPP chain in the STM image indicate that the PPP chain under investigation is present in two different configurations.

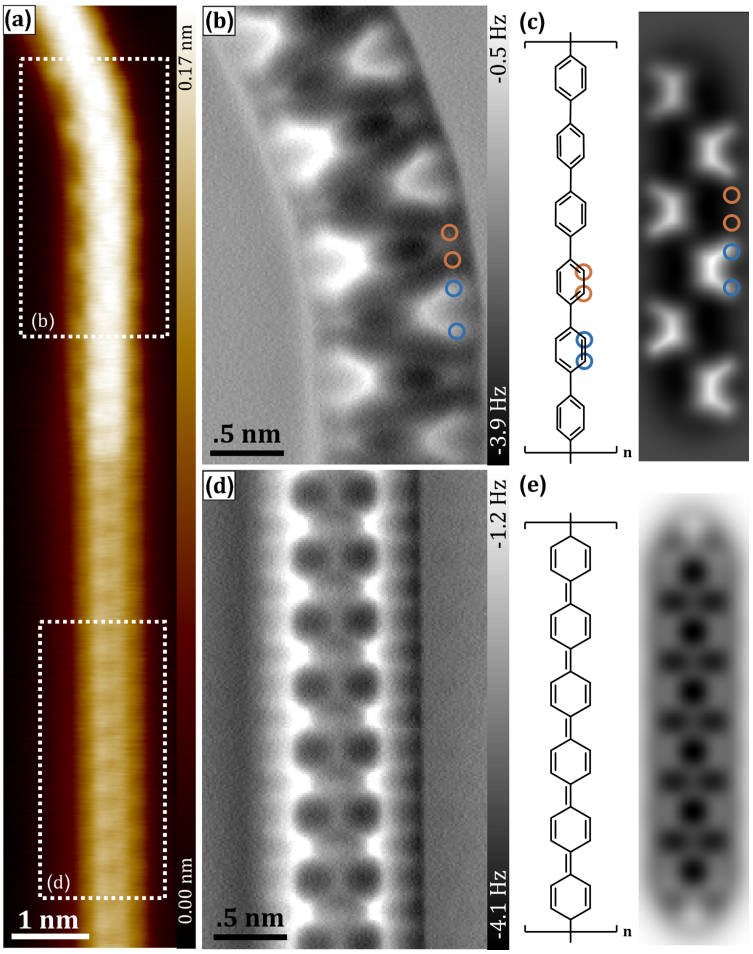


Figure 5.6: Detailed investigation of PPP chains ($T = 523\,\mathrm{K}$). (a) STM image of a PPP chain exhibiting two distinct image contrasts and (b) cc-AFM image of a benzenoid-type PPP chain. (c) Left: Structure of benzenoid-type chain. Right: Corresponding simulated ch-AFM image using the probe particle model. (d) cc-AFM image of a quinoid-type PPP chain. (e) Left: Structure of quinoid-type chain. Right: Corresponding simulated ch-AFM image using the probe particle model. Imaging parameters: (a) $V_\mathrm{g} = 100\,\mathrm{mV}$, $I_\mathrm{t} = 10\,\mathrm{pA}$, (b) $V_\mathrm{g} = 50\,\mathrm{mV}$, $I_\mathrm{t} = 35\,\mathrm{pA}$ and (d) $V_\mathrm{g} = 20\,\mathrm{mV}$, $I_\mathrm{t} = 140\,\mathrm{pA}$.

The cc-AFM image taken of a section in the upper part of the PPP chain, which exhibits a brighter contrast (higher apparent height), is shown in Figure 5.6 (b). The image shows two bright features per phenyl ring alternately showing up on the left and right side of the chain, indicating that one side of the phenyl rings is alternately tilted towards the sample. The probe particle model simulation of a chain with alternate tilts of $\sim 33\,^{\circ}$ per phenyl ring indicates that the chain is a PPP chain in benzenoid conformation (see Figure 5.6 (c)). In Figure 5.6 (d), the darker (lower apparent height) part of the PPP chain is resolved by cc-AFM. The AFM image shows a chain with a flat adsorption geometry. The measurements support the assumption that PPP exists in another stable quinoid-type structure, which also matches well with simulations using the probe particle model (see Figure 5.6 (e)). Note that tilts of $\sim 33\,^{\circ}$ were chosen for the simulation of the benzenoid-type PPP chain in accordance with the simulations of the intact CPP rings. The real tilts of para-linked phenyls are dependent on the molecules and the molecule-substrate interaction and can be as low as e.g. $\sim 3\,^{\circ}$ in case of a terphenyl molecule on Cu(111) [117]. A detailed study on the different adsorption configurations of PPP chains was performed by Yuan and Li et al. [215]. Quinoid- and benzenoid-type PPP chains were also observed when synthesizing the chains with a 4,4"-dibromo-p-terphenyl precursor using an Ullmann-type reaction on Cu(111). Since the phenyl units are connected by freely rotatable single bonds in para-position, the benzenoid chains adsorb in a non-planar configuration. However, the non-rotatable double bonds between phenyl rings in the quinoid-type chains force them into a coplanar adsorption configuration. Figure 5.6 (a) reveals that quinoid-type and benzenoid-type chains can transform into each other in a single PPP chain. Yuan and Li et al. also report that no quinoid-type chains can be found on Au(111), which has been attributed to the weaker molecule-substrate interaction and lower charge transfer compared to Cu(111) [215].

The results of the on-surface reactions of (6)CPP, (8)CPP and (10)CPP are summarized in Figure 5.7 as a function of the reaction temperature. Please note that the temperatures displayed in Figure 5.7 were recorded for certain fixed temperatures, the exact start of the events cannot be determined this way and may happen in between recorded temperatures. The reaction pathway of the on-surface synthesis of carbon nanoribbons by (6)CPP can essentially be divided into four steps. Initially, islands of unopened (6)CPPs (monolayers) form on the Cu(111) surface, which can be observed up to a temperature of at least 523 K. The islands coexist with PPP chains starting at a temperature of 353 K, which marks the start of the ring-opening polymerization. At 543 K, benzyne formation within PPP chains arises, whereby nanoribbons are formed by the fusion of neighboring PPB chains starting at approximately 583 K. In the case of (8)CPP, a different pathway is observed. The intact CPPs form multilayers, which are stable up to about 423 K and transform into monolayers with flat-lying molecules (up to approximately 473 K). Ring-opening of (8)CPP begins at 423 K, which coincides with the onset of benzyne formation within intact (8)CPP molecules (starting between 423 K and 473 K). As for (6)CPP, the benzyne formation within chains starts at 543 K and the nanoribbon formation at 583 K. The degradation of the products starts at around 633 K, which would most likely also be the case for the ribbons formed by (6)CPP, but for (6)CPP no data was recorded at such high temperatures.

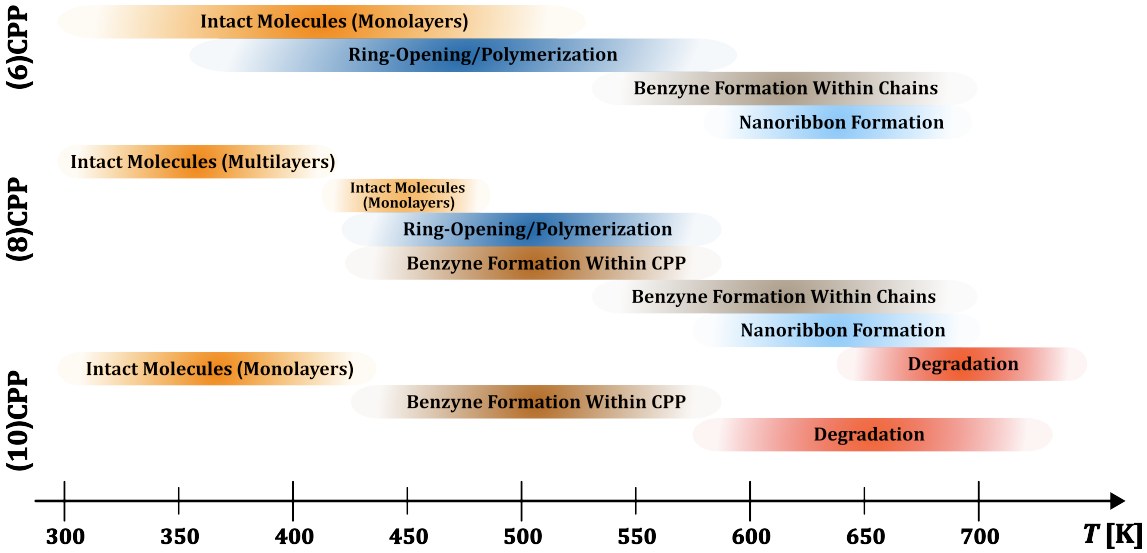


Figure 5.7: Overview of the reaction temperatures derived from the on-surface reactions of (6)CPP, (8)CPP and (10)CPP on Cu(111).

For (10)CPP, only three events can be determined when the sample is annealed. Monolayers with intact, flat-lying CPPs can be found on the surface up to a temperature of 423 K. As for (8)CPP, the benzyne formation within unopened (10)CPP molecules starts between 423 K and 473 K. Finally, structure degradation of the CPP rings begins at 583 K, but no PPP chains are formed.

As rationalized by the experimental data, the loss of the hydrogen atoms within hitherto intact (8)CPP and (10)CPP molecules starts between 423 K and 473 K. For (8)CPP, the ring-opening temperature between 423 K and 473 K coincides with the temperature for the hydrogen loss within intact rings. For (10)CPP, the first opened rings can be found in agglomerated structures at 583 K (see Figure 5.4 (f)). As the ring-opening temperature of 353 K for (6)CPP is far below this temperature and a full polymerization occurs, this suggests a rather strong effect of the ring strain on the ring-opening process. The observed competing reaction, i.e., the loss of hydrogen atoms in intact (8)CPP and (10)CPP molecules, along with the associated stronger interaction with the surface atoms, will certainly influence the mobility of the molecules on the surface and might hamper the reaction pathway. Figure B.9 shows STM images of the sample annealing of (8)CPP in a temperature range of 388 - 425 K for 19 hours. The long annealing of (8)CPP does not lead to an increase in opened molecules and long PPP chains. However, the same mix of unopened, intact (8)CPPs, PPP chains and separated, dehydrogenated (8)CPPs can be observed. This again indicates that the ring-opening process and the dehydrogenation reaction within (8)CPPs start in the same temperature range. PPP chains and unopened rings binding to the sample coexist in the case of (8)CPP. As a result, the ROP reaction can take place and nanoribbons are formed, but the unopened rings between PPP chains disturb the interaction and form unordered structures between chains, leading to a lower yield compared to (6)CPP. The ring-opening temperature of (10)CPP could not be determined experimentally, since only a few opened molecules can be observed in agglomerated structures at high temperatures of 583 K (see Figure 5.4 (f)). While both processes compete for (8)CPP, the reaction equilibrium for (10)CPP is completely on the side of the

benzyne formation within intact (10)CPP rings. For (10)CPP, no ROP takes place, which makes the molecule unsuitable for the on-surface synthesis of nanoribbons.

The varying ring-opening temperatures for CPPs of different sizes should be related to the different internal strain energy, which decreases as the ring size increases. While (6)CPP is a highly strained molecule with a strain energy of 401.7 kJ mol^{-1}, the strain energy of (10)CPP decreases to almost half (241.4 kJ mol^{-1}) [222]. In the gas phase, this results in energy barriers for the direct ring-opening process ranging from 352 kJ mol^{-1} ((6)CPP) [131] to 394 kJ mol^{-1} ((8)CPP) and 416 kJ mol^{-1} ((10)CPP) (see Figure B.10). However, on the Cu(111) surface, the barrier for the opening process can be strongly influenced by the precise adsorption conformation of the molecule, which makes it difficult to reliably estimate this value by theoretical approaches. Interestingly, our gas phase calculations suggest that the radical attack (see Figure 5.1, Step **2**) can also be strongly influenced by the ring size and strain (also favoring smaller ring sizes, see Figure B.10). This will, however, also be affected by the surface, which makes it difficult to unambiguously identify the reaction mechanisms that determine the pathway.

As already discussed in Figure 5.3, in the case of (8)CPP, PPP chains and unopened molecules including benzyne units are simultaneously present on the surface. In the case of (6)CPP, only opened rings or intact molecules can be found. Therefore, the intermediate state of a radical attaching to an intact molecule (see Figure 5.1, Step **2**) can most likely not be observed. Due to the slower ring-opening compared to (6)CPP, this intermediate state might be found for (8)CPP. For more information see STM and AFM images in Figure B.11.

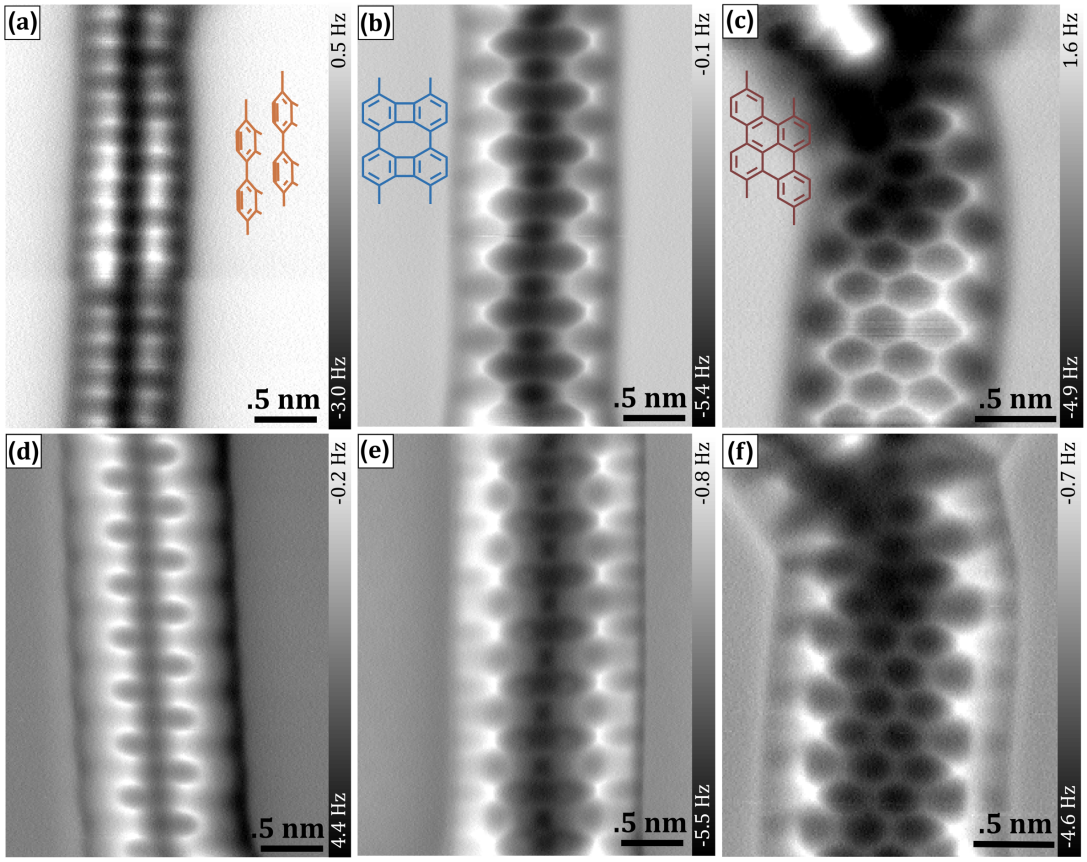


Figure 5.8: AFM images of the products formed by the on-surface reaction of (8)CPP (T = 583 K). Upper row: ch-AFM images. Lower row: cc-AFM images. (a) and (d) Poly(*para*-benzyne) chain, (b) and (e) biphenylene nanoribbon and (c) and (f) graphene nanoribbon. Imaging parameters: (a) $\Delta z = +150$ pm, (b) $\Delta z = -35$ pm and (c) $\Delta z = +5$ pm. All scanning heights are given with respect to the STM setpoint of $V_g = -0.57$ mV, $I_t = 10$ pA. (d) $V_g = 20$ mV, $I_t = 20$ pA, (e) $V_g = 20$ mV, $I_t = 120$ pA and (f) $V_g = 20$ mV, $I_t = 45$ pA.

Benzyne formation within PPP chains (see Figure 5.1, Step **4**) starts between 523 K and 543 K. The corresponding ch-AFM and cc-AFM images of a PPB chain are shown in Figure 5.8 (a) and (d). The different image features in AFM images (ch: dots, cc: halo-like) of PPB chains match well with their appearance within (10)CPP rings (see Figure B.8), supporting the assumption that benzyne formation within CPPs occurs during sample annealing (see Figure 5.3 (h) and Figure 5.4 (e)). Despite disruption of the ROP by unopened molecules, the two products found for (6)CPP, GNRs and BNRs, can also be observed using (8)CPP as a precursor. Figure 5.8 (b) and (e) (BNR) and Figure 5.8 (c) and (f) (GNR) show the corresponding AFM images. Note that the formation of the two different nanoribbons depends on the chain alignment of the PPB chains (see Figure 5.1, Step **5**). When benzynes are facing each other, BNR is obtained, whereas shifting one chain by 0.5 unit cells will lead to the formation of a GNR. For example, in the case of the PPB chain in Figure 5.8 (a) and (d), due to non-facing benzyne units, a GNR would be formed upon chain fusion. Although the ROP is inhibited by unopened (8)CPP molecules, rather long BNRs can also be found using (8)CPP on Cu(111) (see Figure B.12).

5.2.6 Discussion

Compared to the fusion of PPP chains on Cu(111), two major differences can be observed for experiments on Au(111) and Ag(111). In our case, the formation of two different products, BNRs and GNRs, is observed. However, the chain fusion of PPP chains on Au(111) and Ag(111) has been found to exclusively lead to the formation of graphene nanoribbons [210, 211, 212]. While in rare cases, three PPB chains can fuse to form a nine atom wide armchair graphene nanoribbon (9-AGNR, see Figure B.13), the PPB fusion on Cu(111) mainly leads to 6-AGNR by the reaction of two adjacent PPB chains. This is in stark contrast to observations on Au(111), where the fusion of five PPP chains leading to 15-AGNRs has been reported [210]. These results indicate a different molecule-substrate interaction of PPP and PPB chains for the two metal substrates. Note that in the three mentioned examples for synthesizing graphene nanoribbons via PPP chains, 4,4"-dibromo-p-terphenyl was used as a precursor to fabricate the PPP chains via an Ullmann coupling reaction [210, 211, 212]. Therefore, an interaction of the PPP chains with cleaved bromine atoms, at least for reactive surfaces, cannot be excluded either. For the synthesis of PPP chains on Ag(111) and Cu(111) via halogenated precursors, an interference of the PPP chains with cleaved halogen atoms has been reported [212, 213, 214]. Furthermore, when using the aforementioned 4,4"-dibromo-p-terphenyl precursor on Au(111) [211] and Cu(111) [213], two different self-assembly patterns form due to the different molecule-substrate interaction. This further supports the assumption that on-surface synthesis processes with halogenated precursors on metal surfaces are difficult to predict. This indicates that the halogen-free approach when fabricating PPP chains, as presented in this work, is a more reliable way for synthesizing PPP chains and nanoribbons, since the interaction of the atoms through the halogen bonds and the intermediate step of the Ullmann coupling are absent. Furthermore, it can be ruled out that halogen adatoms influence the PPP chain growth. Consequently, long PPP chains and nanoribbons can form when using halogen-free (6)CPP as a precursor. As introduced in Section 2.5, the electronic properties of graphene nanoribbons depend on their width, therefore the synthesis of ribbons of confined sizes is favorable. The synthesis presented in this work leads almost exclusively to six atom wide graphene and biphenylene nanoribbons, which makes the electronic properties of the synthesized products more predicable.

We observe that the ROP is facilitated when using smaller, highly strained cycloparaphenylenes for the on-surface synthesis of nanoribbons on Cu(111). For (6)CPP, this leads to a full ROP reaction on the surface and a high yield of GNRs and BNRs. For (8)CPP, only partial polymerization is observed, whereas unopened agglomerates of molecules are located next to the nanoribbons, which form with a lower yield compared to (6)CPP. In case of (10)CPP, the biggest counterpart of investigated cycloparaphenylenes, no nanoribbon formation is observed, because the great majority of the molecules adsorbed on the surface do not open. Consequently, at high temperatures, only unordered agglomerates of randomly reacted molecules can be found on the surface. This may be linked to the lower strain energy of (8)CPP and (10)CPP, because the initial ring-opening and radical formation, which marks the start of the ROP, is hampered. (6)CPP can only be found as intact rings and opened PPP chains on the surface. However, for (8)CPP and (10)CPP, also large amounts of unopened CPPs that partially lost their hydrogens are observed, whereas the ratio is larger in the case of (10)CPP. These unopened molecules do not contribute to the

ROP, which is the reason why the yield decreases with increasing ring sizes. The onset of this hydrogen loss was determined to be between 423 - 473 K for the (8)CPP and (10)CPP molecules. For (8)CPP, this coincides with the initial ring-opening of the molecules at 423 K, whereby the initial ring-opening temperature of (10)CPP could not be determined experimentally. At 353 K, the ring-opening temperature of (6)CPP is far below the temperature for the hydrogen loss within intact rings. As the ring-opening temperature for (8)CPP coincides with the temperature for the hydrogen loss inside intact molecules and for (10)CPP is most likely above, one could conclude that these two processes might be competing processes in the ROP of cycloparaphenylenes. However, if molecules that lost their hydrogens could still contribute to the ROP by a radical attack or remain unopened on the surface, cannot be rationalized by our experimental data. Possibly, due to the fixed position on the surface upon formation of covalent bonds to the copper substrate, the on-surface mobility of the molecules could be limited, which makes it more unlikely to randomly meet a radical.

However, a finding that is not explained when comparing the data for (6)CPP, (8)CPP and (10)CPP is the observation that (6)CPP molecules stay intact in larger islands at higher temperatures than (8)CPPs and (10)CPPs. Intact islands of (6)CPP molecules can still be found up to temperatures of at least 523 K (see Figure B.1 (d)), whereas only opened or dehydrogenated CPPs are observed in the case of (8)CPP and (10)CPP (see Figure B.2 and Figure B.6) at the same and higher temperatures. This finding contradicts the observation that smaller CPPs should open at lower temperatures due to increased ring strains. Interestingly, the on-surface configuration of the molecules in intact monolayers changes for the different ring sizes. (6)CPP forms monolayers with standing molecules. At low temperatures, (8)CPP forms multilayers with standing molecules on top of flat-lying molecules, which transform into layers with flat-lying molecules upon sample annealing. For (10)CPP, monolayers with exclusively flat-lying molecules can be observed (see Figure 5.4 (a)). The flat-lying configuration for larger molecules might be explained by increased van der Waals interactions with the substrate. For (6)CPP, no dehydrogenated flat-lying, but intact, standing molecules can be found at temperatures that exceed the dehydrogenation temperature determined for (8)CPP and (10)CPP. This indicates that the adsorption configuration influences the dehydrogenation and ring-opening process. The dehydrogenation process of carbon atoms depends on the precise adsorption conformation of the hydrogen atoms on the catalyzing Cu(111) surface and has been reported to take place in a relatively wide temperature range of 413 - 620 K [14, 24, 164, 228]. The presence of intact, standing (6)CPPs at high temperatures might therefore be linked to the standing configuration, in which hydrogen atoms are situated farther away from the copper substrate. For flat-lying (8)CPP and (10)CPP molecules, a larger number of hydrogen atoms is in close proximity to the substrate, which may increase the probability of a catalyzed dehydrogenation reaction. Please note that these assumptions require further experimental and computational investigations, which exceed the scope of this work.

5.3 Summary

In summary, the on-surface synthesis of graphene and biphenylene nanoribbons via halogen-free cycloparaphenylene precursors is presented. In general, it was shown that CPP molecules are suited to form longer PPP chains on the surface, compared to the synthesis via conventional Ullmann-type reaction steps with halogenated precursors. This may be attributed to the elimination of complex self-assembly mechanisms and interference-free chain growth due to the absence of halogen adatoms. The results indicate that halogen-free precursors are promising candidates for future applications in the OSS.

Further, the influence of the ring size and strain was systematically investigated, by presenting a comprehensive overview of the temperature induced on-surface reaction of a set of cycloparaphenylenes ((6)CPP vs. (8)CPP vs. (10)CPP). From the herein presented results, it can be rationalized that the ROP is facilitated by high ring strains (fewer number n of phenyls units). Our experiments reveal that (6)CPP almost exclusively forms PPP chains on the Cu(111) surface, whereas for (8)CPP, the formation of PPP chains and leftovers of unopened molecules can be observed. For the biggest investigated counterpart (10)CPP however, almost only unopened rings can be found on the surface, through which the PPP chain growth is suppressed. Our findings indicate that the altered ring strain of the CPPs might be the origin of the distinct reaction pathways. This leads to different ratios of opened rings for the CPPs, resulting in lower yields of nanoribbons for larger CPPs. Additionally, there might be a competition between the initial ring-opening and ring internal dehydrogenation reaction. The dehydrogenation of phenyl units in intact CPPs may be linked to the precise adsorption configuration of the molecules and is only observed for (8)CPPs and (10)CPPs. Due to the formation of covalent bonds to the substrate, the surface diffusion of (8)CPP and (10)CPP molecules may be inhibited, which could further hinder the ring-opening polymerization.

6 Conclusion and Outlook

The on-surface synthesis is a novel field of research, opening up almost unlimited possibilities for constructing low-dimensional, tailored carbon nanostructures. However, owing to its nascent state, there remain numerous challenges and unresolved questions, making it an intriguing and vibrant area of research. This results from the multitude of parameters that can be adjusted to influence on-surface reactions, including the utilized precursors as well as their functionalization, the substrate and the type of molecular manipulation method (e.g. temperature, tip manipulation). All of the aforementioned variables impact not only the on-surface reaction itself, but also the precise arrangement of atoms and bonds in neighboring precursors, which is dictated by the self-assembly process. Thereby, the self-assembly can often be regarded as the pre-step to the on-surface reaction.

In the first results part of this thesis (see Chapter 4), the self-assembly process of unilaterally fluorinated 1,2,10,11,12,14-hexafluoropentacene was comparatively investigated on inert Au(111) and reactive Cu(111) substrates. The presented results on Au(111) reveal an unique self-assembly pattern, in which the molecules gradually arrange themselves in larger clusters with increasing temperatures, finally resulting in a formation of densely packed layers. Using the chemical bond imaging method, the examination of intermolecular bond distances and angles of hydrogen and fluorine atoms in clusters of different sizes reveals that these hardly change within clusters and densely packed layers. This suggests that the self-assembly on Au(111) is mainly driven by intermolecular interactions. Only when comparing the arrangement of the molecules at the edge and within closed layers, slightly different bonding patterns are observed. For the molecules inside the layer, these align closely with the calculated bulk crystal structure. However, the stronger interaction of the molecules with the reactive Cu(111) substrate leads to changed adsorption geometries, which are characterized by a bending in the center of the molecule. In addition, packed layers on Cu(111) exhibit stacks of molecular dimers and trimers with discernible gaps between them, which may be attributed to the molecule's snap-in on the reactive surface. The highly precise self-assembly study suggests that the H-F interaction has a directional character. Despite the molecular bending, suggesting a strong interaction with the reactive Cu(111) surface, the intermolecular H-F interactions enable the molecules to arrange themselves into ordered layers. This characteristic enhances their potential as a useful tool in on-surface synthesis processes on inert and reactive surfaces.

In addition, there are numerous opportunities to use the knowledge gained in future experiments. For example, hydrogen and fluorine atoms could be incorporated into other, symmetrical precursors to control their molecular alignment and induce on-surface reactions to produce novel, confined carbon nanostructures. Furthermore, fluorine atoms might be integrated to cycloparaphenylene molecules, which are investigated in the second part of this thesis, in order to examine whether the chain growth of the opened rings can be precisely controlled to selectively produce specific nanoribbons.

In the second results part of this thesis (see Chapter 5), a set of cycloparaphenylenes was investigated in order to gain a deeper understanding of the remarkable ring-opening polymerization reaction of (6)CPP, with particular emphasis on the influence of the ring strain. While the smallest counterpart (6)CPP forms highly ordered chains after ring-opening, the decreased ring strain leads to ring-opening in only a small portion of (8)CPP and virtually no ring-opening for (10)CPP. In addition, dehydrogenation of phenyl units in intact CPPs was observed for (8)CPP and (10)CPP, which may have an additional influence on the diffusivity and ring-opening of the molecules. In conclusion, the herein presented results demonstrate that the ring-opening polymerization is facilitated when using smaller, highly strained cycloparaphenylenes. For larger molecules with lower strain energies, the initial ring-opening is hampered, leading to only partial polymerization for (8)CPP and no polymerization in case of (10)CPP.

The presented results open up versatile opportunities to progress in the research of hydrocarbon belts on surfaces. For example, hydrocarbon belts with varying attachments, such as methylene-bridged cycloparaphenylenes, could be investigated for their use in on-surface synthesis. For the herein investigated cycloparaphenylenes, molecules with less than eight phenyl units and differently substituted phenyl groups (e.g. partial substitution of hydrogen by fluorine atoms) could be used to investigate their effect on ring-opening and chain growth. Further, the effect of the ring strain in the ring-opening process could be analyzed more intensely. While all phenyl units in the herein studied cycloparaphenylenes are connected in para-position, the symmetry of the rings can be broken by changing the substitution pattern (e.g. connecting one phenyl unit in ortho- or meta-position). This way, it might be possible to reduce the energy barrier for the initial ring-opening, whereas inducing a ring-opening polymerization may eventually also be possible for larger molecules like (8)CPP and (10)CPP. Further, larger (8)CPP and (10)CPP molecules could be investigated on Ag(111) to evaluate whether the dehydrogenation of phenyl units is inhibited and if ring-opening is preferred on a surface with less catalytic activity.

In general, two fundamental aspects of the research in the field of molecules on surfaces, namely the self-assembly of organic molecules and the on-surface synthesis of carbon nanostructures, were investigated. This work demonstrates that combined STM and chemical bond imaging measurements are powerful tools for investigating these processes on surfaces. The STM is suitable for imaging large surface areas of self-assembled molecules and localize adsorption positions of precursors and products in OSS. In contrast, the chemical bond imaging method unfolds its potential in the precise investigation of adsorption structures and geometries, as well as in deciphering molecular structures of precursors, intermediates and reaction products. This work provides a brief insight into the extremely diverse research field of molecules on metal substrates, thereby highlighting the versatile possibilities for further research projects in this flourishing field.

Appendix A

Supplementary Information on Chapter 4

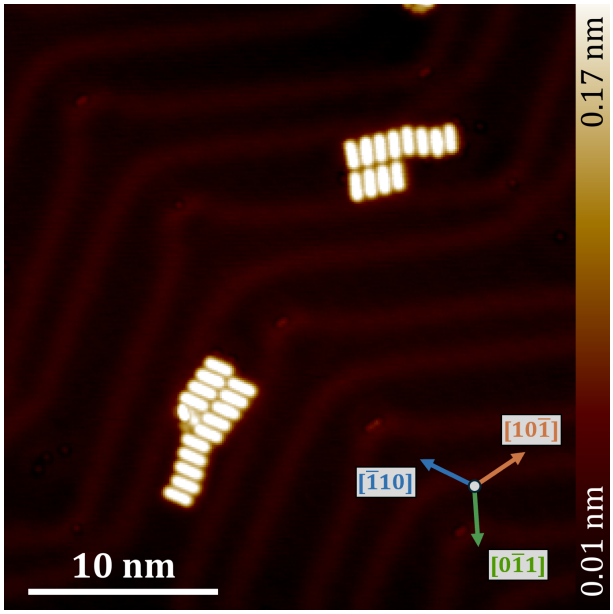


Figure A.1: STM overview image of the surface after annealing the sample at $T = 89\,\mathrm{K}$ with a minimal coverage of molecules. Some larger clusters, but no dimers are observed. Imaging parameters: $V_\mathrm{g} = 100\,\mathrm{mV}$, $I_\mathrm{t} = 10\,\mathrm{pA}$.

Figure A.1 shows a STM overview image of the surface after annealing the sample at $T = 89\,\mathrm{K}$ with a minimal coverage of molecules. In the STM image, only larger clusters of more than ten molecules, but no dimers and small clusters can be observed. This confirms that the dimers and small clusters present in Figure 4.1 (a) are a result of the intermolecular interaction of F_6PEN.

Figure A.2 (a) shows a high-resolution ch-AFM image of a F_6PEN monomer on Au(111). Two different scanning heights with respect to the molecule and substrate were chosen to resolve the underlying substrate as well as the molecule in the same image. A lattice fit of the Au(111) surface atoms (bright blue markers) in Figure A.2 (b) reveals that the molecule is aligning along the densely packed $[0\bar{1}1]$ direction.

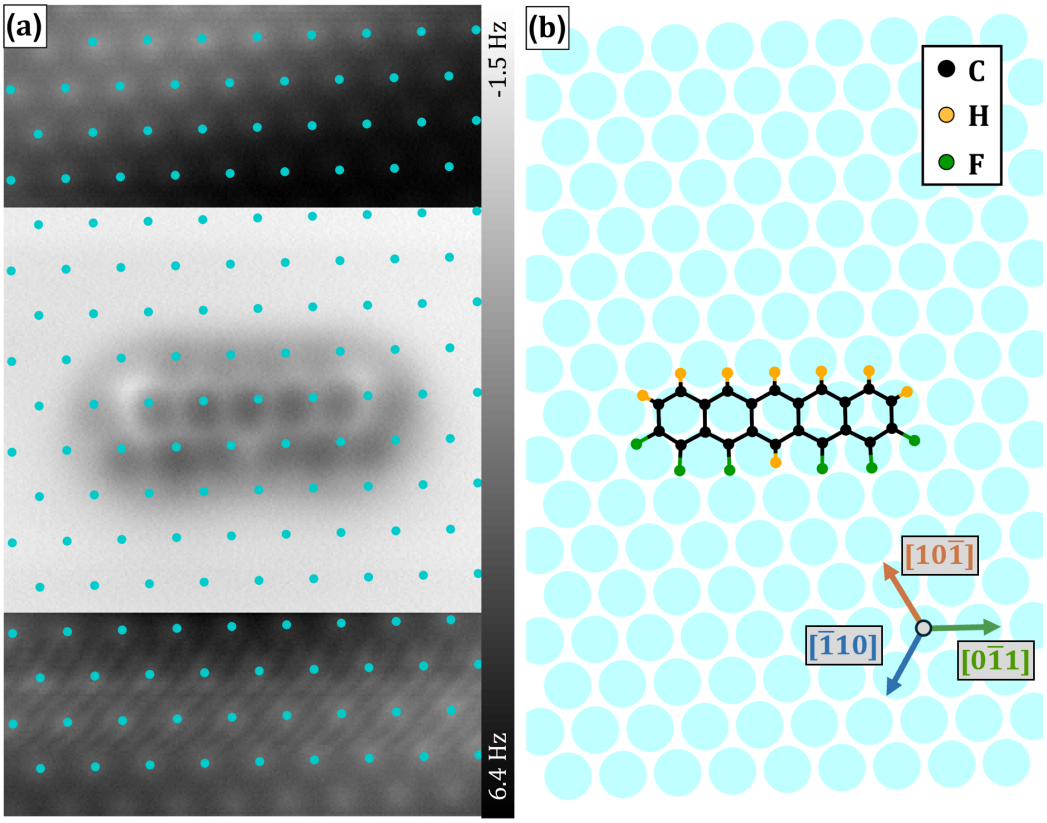


Figure A.2: (a) The high-resolution ch-AFM image reveals the adsorption site of a single F_6PEN molecule on the Au(111) surface ($T = 7\,\mathrm{K}$). The image is divided into three sections with different relative scanning heights, allowing for the simultaneous resolution of the underlying atomic structure of the surface as well as the molecular structure in a single image. Imaging parameters: $\Delta z_{\mathrm{surface}} = -330\,\mathrm{pm}$, $\Delta z_{\mathrm{molecule}} = -30\,\mathrm{pm}$ with respect to the STM setpoint of $V_{\mathrm{g}} = -0.57\,\mathrm{mV}$, $I_{\mathrm{t}} = 10\,\mathrm{pA}$. (b) Sketch of the F_6PEN molecule on the Au(111) surface. The fitted gold atoms are displayed in bright blue color. Orange, green and blue arrows indicate the respective directions of the Au(111) crystal.

A statistic on how many molecules align along a respective crystal direction was performed, showing an exemplary STM image in Figure A.3. A cursor was used to assign the respective $[0\bar{1}1]$, $[10\bar{1}]$ or $[\bar{1}10]$ crystal directions, with molecules encircled in the corresponding colors of the cursor, as shown in Figure A.3 (b). When a molecule did not align in accordance with one of the given directions, it was marked with a white circle ("No direction assigned"). For simplicity, the exemplary image was divided into four quarters, labeled Q1, Q2, Q3 and Q4. This analysis was conducted for a total of 586 molecules across four STM overview images, resulting in an expected ratio of approximately one third per crystal direction. However, about ten percent of the molecules could not be assigned to a specific direction. The results of the example in Figure A.3 as well as the gathered results are listed in Table A.1 and A.2, respectively.

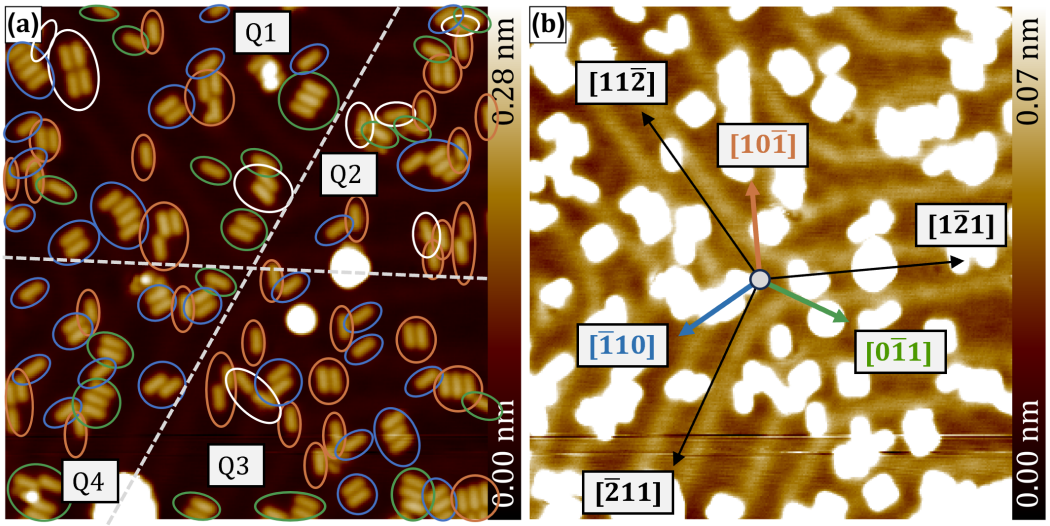


Figure A.3: (a) Exemplary STM image that shows how the crystal direction was assigned to the molecules ($T = 7\,\mathrm{K}$). The image was divided into four quarters to count the molecules aligning along a respective direction. (b) Same STM image with modified contrast to reveal the herringbone reconstruction. The respective lattice directions are depicted by black, orange, blue and green arrows. Imaging parameters: $V_\mathrm{g} = 100\,\mathrm{mV}$, $I_\mathrm{t} = 10\,\mathrm{pA}$. The results for the statistic of this image are listed in Table A.1.

Table A.1: Determination of the number of molecules aligning along each respective crystal direction (see Figure A.3).

	[0$\bar{1}$1] Direction	[10$\bar{1}$] Direction	[$\bar{1}$10] Direction	No Direction Assigned
Q1	10	12	18	7
Q2	4	11	6	4
Q3	9	18	15	2
Q4	10	6	12	0
Total	33	47	51	13

Table A.2: Determination of the number of molecules aligning along each respective crystal direction in a total of four STM images on Au(111).

	Total	[0$\bar{1}$1] Direction	[10$\bar{1}$] Direction	[$\bar{1}$10] Direction	No Direction Assigned
Number of Molecules	586	169	189	172	56
Percentage	100	28.8	32.3	29.4	9.6

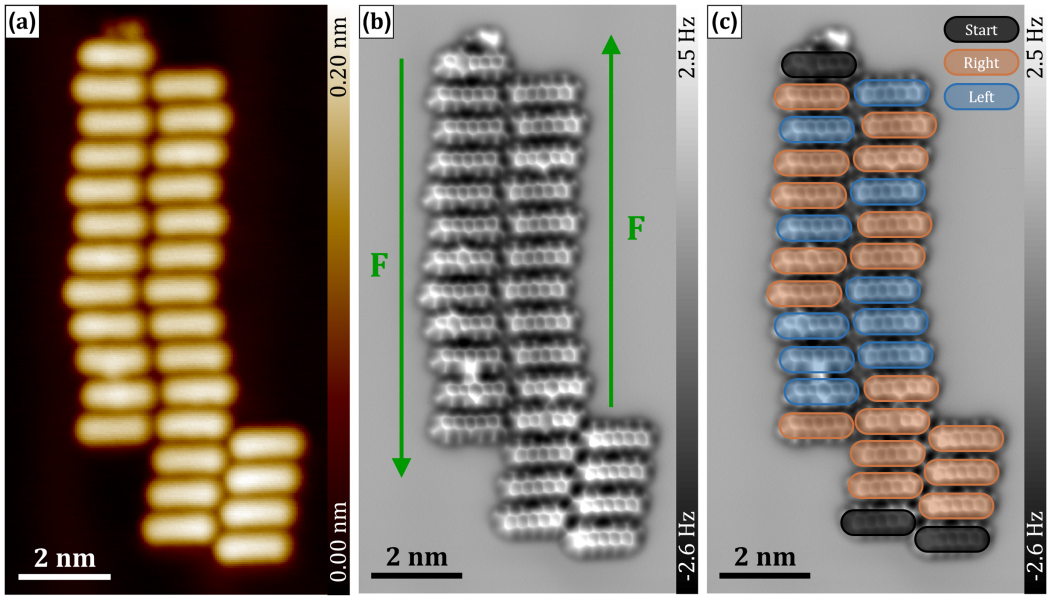


Figure A.4: (a) STM image of Cluster 2. (b) High-resolution ch-AFM image of (a), which enables the determination of the absolute orientation of the F_6PEN molecules. The direction towards which the fluorine atoms point is indicated by green arrows. (c) Example illustrating how the alignment of the molecules was determined. The start of the molecule chain is marked with a black oval, while molecules that are shifted to the right and left are highlighted as orange and blue ovals, respectively. Imaging parameters: (a) $V_g = 100\,\mathrm{mV}$, $I_t = 10\,\mathrm{pA}$ and (b) $\Delta z = -20\,\mathrm{pm}$ with respect to the STM setpoint of $V_g = -0.57\,\mathrm{mV}$, $I_t = 10\,\mathrm{pA}$.

Figure A.4 shows STM and AFM images of Cluster 2. To determine whether a molecule positioned on top of another is aligned to the left or right of the lower molecule, a starting point must be defined for each line. For the analysis presented here, the direction in which the fluorine atoms point was chosen as the starting point of the chain. However, in a conventional STM image (see Figure A.4 (a)), with the chosen imaging parameters it is not possible to define a chain start, as hydrogen and fluorine atoms cannot be distinguished. The AFM image in Figure A.4 (b), recorded using the chemical bond imaging method, clearly reveals the positions of the fluorine atoms. Figure A.4 (c) illustrates an example of how the direction of the molecules on top was determined relative to the molecule below. The origin of a chain is marked with a black oval, whereas molecules that are shifted to the right and left are highlighted as orange and blue ovals. This was done for a total of ten AFM images and 139 molecules, leading to an expected ratio of almost 50:50. For further information see Table A.3.

Table A.3: Assigned molecule displacements (see example in Figure A.4) for a total of ten images and 139 molecules.

	Number of Molecules	Percentage
Shifted Right	67	48.2
Shifted Left	72	51.8
In total	139	100

Figure A.5 (a) shows a cloud diagram of the angles φ_1 and φ_2, determined in the dimer structures in the different cluster sizes, whereas Figure A.5 (b) presents their angle α (see Figure 4.3 (a)). A sketch of the effective angle θ_{eff} that was determined for the H-F interactions is shown in Figure A.5 (c). The effective angle describes the head-on angle of both atoms that results when one of the atoms is shifted perpendicular to result in a parallel arrangement (light-colored atom on the right side). Correspondingly, for ideal type I halogen bonds ($\varphi_1 = \varphi_2$), effective angles θ_{eff} of 180 ° are obtained.

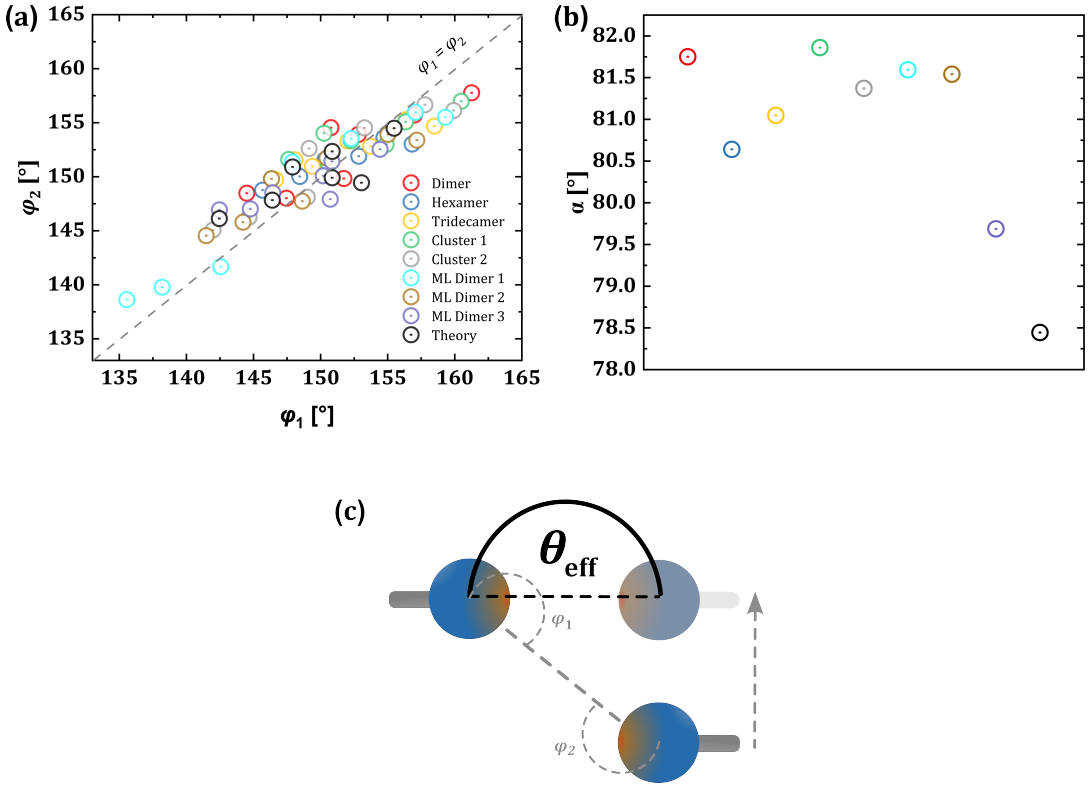


Figure A.5: (a) Cloud diagram of the angles φ_1 and φ_2 determined in the dimer structures in the different cluster sizes. The dashed gray line corresponds to the ideal type I halogen bond ($\varphi_1 = \varphi_2$). (b) Angle α (see Figure 4.3 (a)) for the dimer structures in the different cluster sizes. (c) Sketch that explains the geometry of the effective angle θ_{eff}.

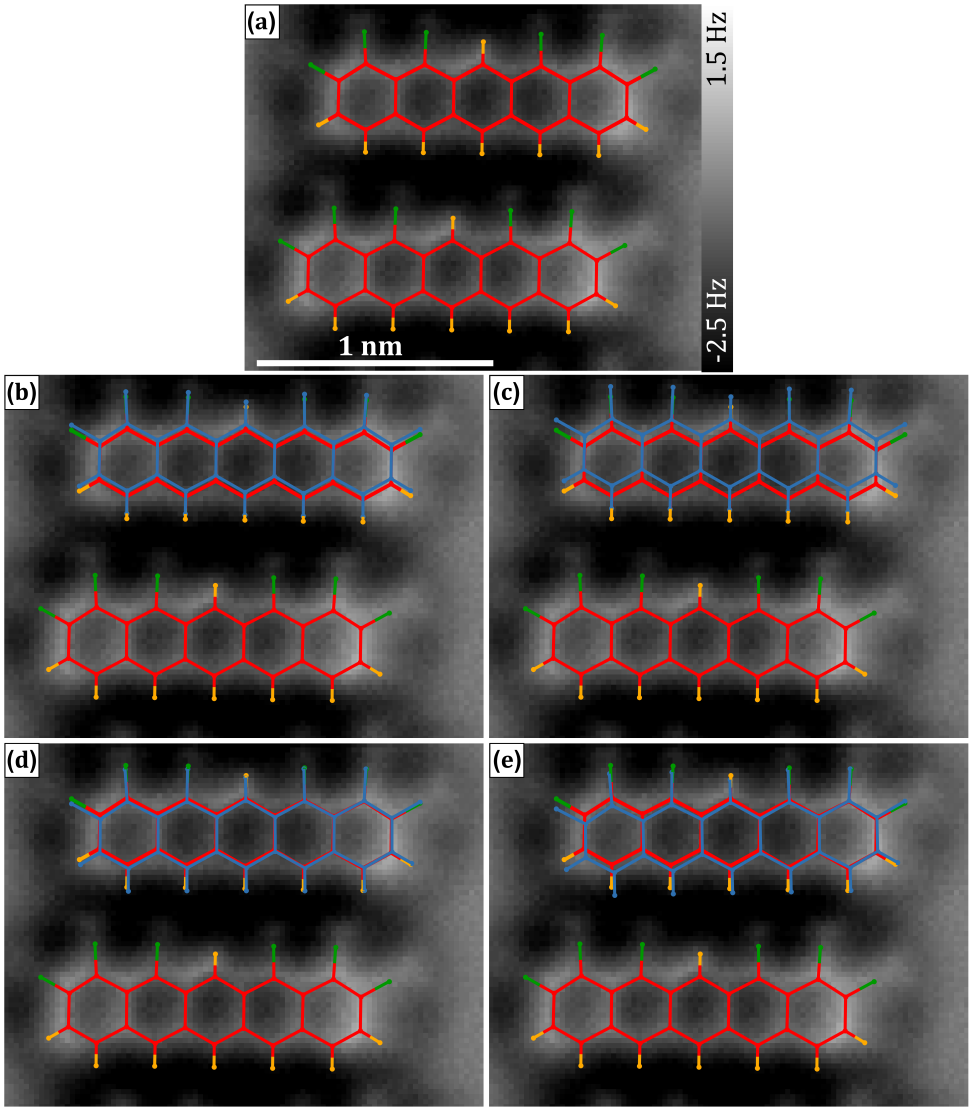


Figure A.6: Set of fits of the molecular structures that was used to estimate the error resulting from inaccurate fitting. The red structures represent the original fit of two F_6PEN molecules in the Tridecamer shown in Figure 4.2 (d), whereas the blue structures show alternative fits of the top molecule. (a) Original fit that was used for data processing of the Tridecamer structure. The molecule in the alternative structures is (b) shifted vertically by one pixel, (c) shifted vertically by two pixels, (d) rotated by one degree and (e) rotated by two degrees. The distances and angles were determined in the same way as in Figure 4.2 (c). The errors were calculated according to Equation A.1.

Figure A.6 was used to estimate the errors that result from inaccurate fitting of the corresponding molecule structures. Therefore, the original fit of the Tridecamer structure (see Figure A.6 (a)) was compared to the same structure with varying fits for the upper molecule, which are represented in blue color. For comparison, the upper structure was displaced vertically by one pixel and two pixels (see Figure A.6 (b) and (c)) and rotated by one degree and two degrees (see Figure A.6 (d) and (e)). The minimum and maximum

absolute deviations of the distances and angles of the alternative fits were calculated in relation to the original fit. The corresponding relative percentage deviation from the original fit was calculated using Equation A.1:

$$\sigma_{\mathrm{rel}} = \left(1 - \frac{ValueOriginalFit}{ValueShiftedFit}\right) \cdot 100. \tag{A.1}$$

In addition to the structures displayed in Figure A.6, the errors were also determined for shifting the fitted molecule on top by one and two pixels horizontally. The errors for the structures were calculated for all seven bonds per dimer. Corresponding angles and distances are exemplified in Figure 4.2 (b) and (c). The respective lowest and highest absolute errors and relative deviations of the bond distances and angles are listed in Table A.4 and A.5.

Table A.4: Absolute errors and relative deviations of the bond distances when changing the position or rotation of the fitted molecule on top. Relative deviations are always given in positive values.

Molecule Position	Absolute Errors [pm]		Relative Deviation [%]	
	Min. Value	Max. Value	Min. Value	Max. Value
Shifted 1 pixel ver/hor	9.8	19.4	3.3	7.4
Shifted 2 pixels ver/hor	16.3	39.0	6.0	14.8
Rotated by 1 °	0.8	18.2	0.3	6.7
Rotated by 2 °	1.1	36.5	0.4	13.4

Table A.5: Absolute errors and relative deviations of the bond angles when changing the position or rotation of the fitted molecule on top. Relative deviations are always given in positive values.

Molecule Position	Absolute Errors [°]		Relative Deviation [%]	
	Min. Value	Max. Value	Min. Value	Max. Value
Shifted 1 pixel ver/hor	1.9	4.1	1.2	2.8
Shifted 2 pixels ver/hor	3.5	8.5	2.2	5.7
Rotated by 1 °	0.4	4.1	0.3	2.7
Rotated by 2 °	0.9	8.5	0.6	5.6

In general, displacing the fitted molecules by two pixels or rotating them by 2 ° results in an error approximately twice as large as that observed when shifting by one pixel or rotating by 1 °. However, as illustrated in Figure A.6 (c) and (e), such adjustments by two pixels or 2 ° lead to unreasonably poor fits that are visible to the naked eye. Consequently, for the estimation of errors, only the values corresponding to molecules shifted by one pixel or rotated by 1° were considered. The maximum values yield estimated errors of ± 20 pm for the distances and ± 5 ° for the angles φ_1 and φ_2. Note that the error associated with a displacement by a specific number of pixels is highly dependent on the image

resolution. For instance, the image depicting the Dimer structure (see Figure 4.2 (b)) has a higher resolution compared to the Tridecamer image used for the error estimation. When the same error estimation approach is applied to the Dimer structure, the errors for the distances and angles are significantly smaller, ranging from 1.73 - 10.87 pm and 0.33 - 1.08 °, respectively.

A similar error estimation was performed for the angle α and the distance of two atoms in two molecules placed on top of each other (see dashed blue lines in Figure 4.3 (a)), leading to estimated errors in the order of magnitude of ± 20 pm and ± 1.5 °. The results are gathered in Table A.6.

Table A.6: Absolute errors and relative deviations for the distance and angle α between two molecules, presented for changes in the position and rotation of the upper molecule. Relative deviations are always given in positive values.

Molecule Position	Distance		Angle	
	Absolute Errors [pm]	Max. Rel. Deviation [%]	Absolute Errors [°]	Max. Rel. Deviation [%]
Shifted 1 pixel ver/hor	21.0	2.7	1.6	2.0
Rotated by 1 °	16.1	2.2	0.6	0.7

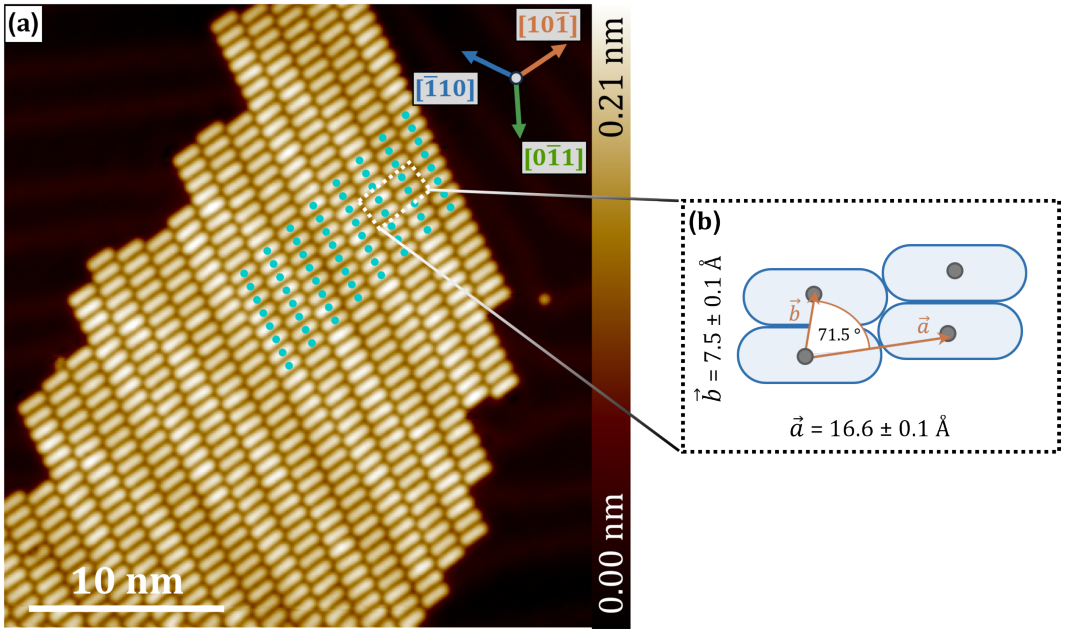


Figure A.7: STM overview image of a F_6PEN layer on Au(111) (T = 298 K). The fitted lattice, represented as bright blue dots, is used to determine the lattice parameters. Imaging parameters: V_g = 100 mV, I_t = 10 pA. (b) Sketch of a crystal structure subunit showing the determined lattice parameters. The error for the angle is ± 1 °.

Figure A.8 depicts a sketch of the Au(111) lattice, indicated by blue circles. The $\sqrt{31} \times \sqrt{7}$ R70 superstructure is highlighted by orange circles. The corresponding vectors $\vec{a}$ and $\vec{b}$ have lengths of 1606 pm and 763 pm with an angle of 70 °. The vectors $\vec{a}$ and $\vec{b}$ are tilted by 9 ° and 19 ° with respect to the densely packed $[10\bar{1}]$ and $[0\bar{1}1]$ directions along which the F_6PEN molecules align.

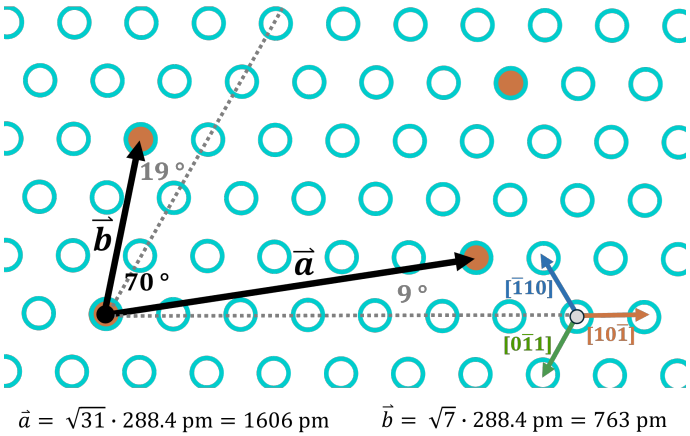


Figure A.8: Sketch of the Au(111) lattice (blue circles) with the corresponding vectors of the $\sqrt{31} \times \sqrt{7}$ R70 superstructure (orange circles).

Figure A.9 (a) shows a high-resolution ch-AFM image of a F_6PEN monomer on Cu(111). Two different scanning heights with respect to the molecule and substrate were chosen to resolve the underlying substrate as well as the molecule in the same image. A lattice fit of the Cu(111) surface atoms (bright blue markers) in Figure A.9 (b) reveals that the molecule is aligning along the densely packed $[10\bar{1}]$ direction. Thus, the centers of the phenyl rings align with the hcp hollow sites of the underlying Cu(111) substrate. A statistic on how many of the molecules align along a respective direction is provided in Figure A.10 and Table A.7.

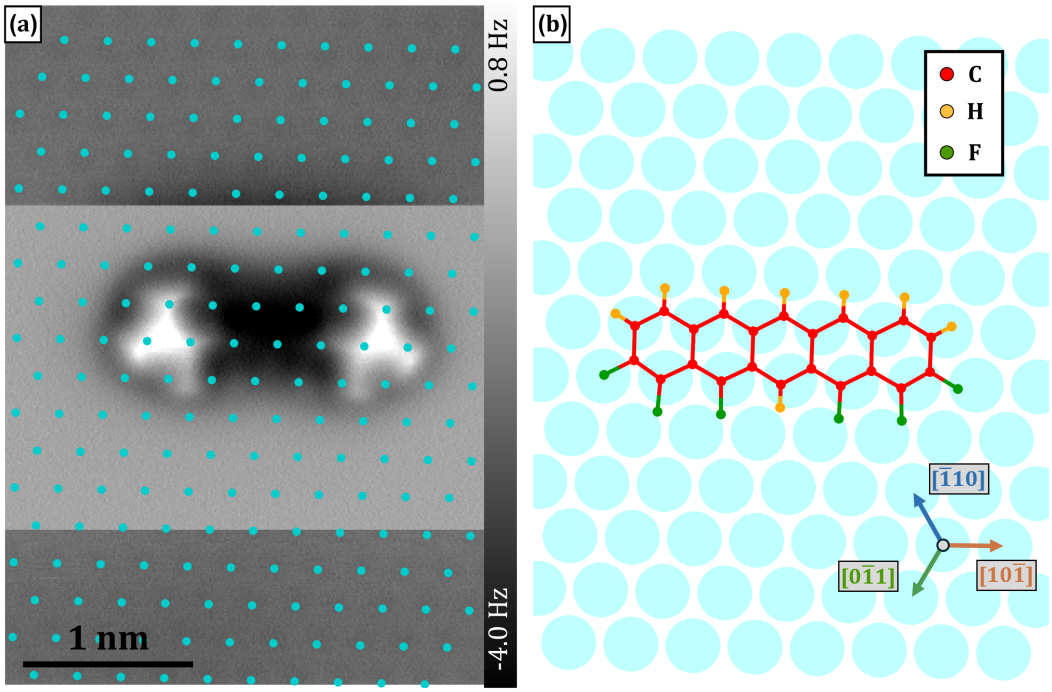


Figure A.9: High-resolution ch-AFM image of a F_6PEN monomer on Cu(111) ($T = 7\,\mathrm{K}$). The image is divided into three sections with different relative scanning heights, allowing for simultaneous resolution of the molecule as well as the underlying substrate. Imaging parameters: $\Delta z_{\mathrm{surface}} = -340\,\mathrm{pm}$, $\Delta z_{\mathrm{molecule}} = -90\,\mathrm{pm}$ with respect to the STM setpoint of $V_g = -0.57\,\mathrm{mV}$, $I_t = 10\,\mathrm{pA}$. (b) Sketch of the F_6PEN molecule on the Cu(111) surface. The fitted copper atoms are displayed in bright blue color. Orange, green and blue arrows indicate the respective directions of the Cu(111) crystal.

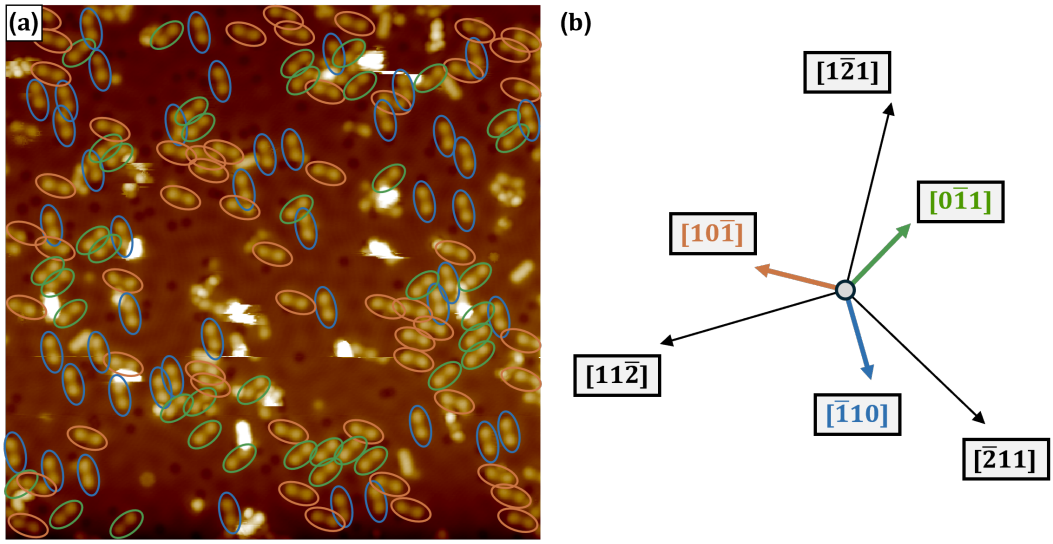


Figure A.10: (a) Exemplary STM image that shows how the crystal direction was assigned to the molecules ($T = 7\,\mathrm{K}$). (b) Cursor indicating the crystal directions of the Cu(111) surface. Imaging parameters: (a) $V_\mathrm{g} = 100\,\mathrm{mV}$, $I_\mathrm{t} = 10\,\mathrm{pA}$.

In the same fashion as for Au(111) (see Figure A.3), a statistic on how many molecules align along a respective crystal direction was performed for Cu(111). This is exemplified for one image in Figure A.10 (a), whereas the cursor in Figure A.10 (b) was used to determine the crystal direction of the molecules. Only structures that could be, due to the molecular bending, identified beyond doubt as F_6PEN and were not enclosed by dirt, were taken into account. This was done for a total of 487 molecules, resulting in an expected ratio of approximately one third per crystal direction. Unlike Au(111), there are no molecules on Cu(111) that do not align along one of the designated [0$\bar{1}$1], [10$\bar{1}$] or [$\bar{1}$10] crystal directions. For further information see Table A.7.

Table A.7: Determination of how many molecules align along a respective crystal direction on Cu(111).

	Total	[0$\bar{1}$1] Direction	[10$\bar{1}$] Direction	[$\bar{1}$10] Direction	No Direction Assigned
Number of Molecules	487	137	186	164	0
Percentage	100	28.1	38.2	33.7	0

Figure A.11 displays consecutive upward (see Figure A.11 (a)) and downward (see Figure A.11 (b)) scans of a F_6PEN dimer on Cu(111). As indicated by white arrows, the upper molecule transitions between two adsorption positions in the consecutive scans, while the lower molecule remains in a stable position. A sketch of the dimer structure adsorbed on the Cu(111) surface (see Figure A.11 (c)) reveals that the lower, stably adsorbed molecule aligns with the centers of the phenyl rings above the hcp hollow sites of the Cu(111) surface. This is in correspondence with the stably adsorbed monomer (see Figure A.9). However, the upper molecule jumps back and forth between two bridge sites of the Cu(111) lattice, indicating an energetically less favorable adsorption position. The two adsorption positions of the upper molecule are displayed as red and blue F_6PEN structures, respectively.

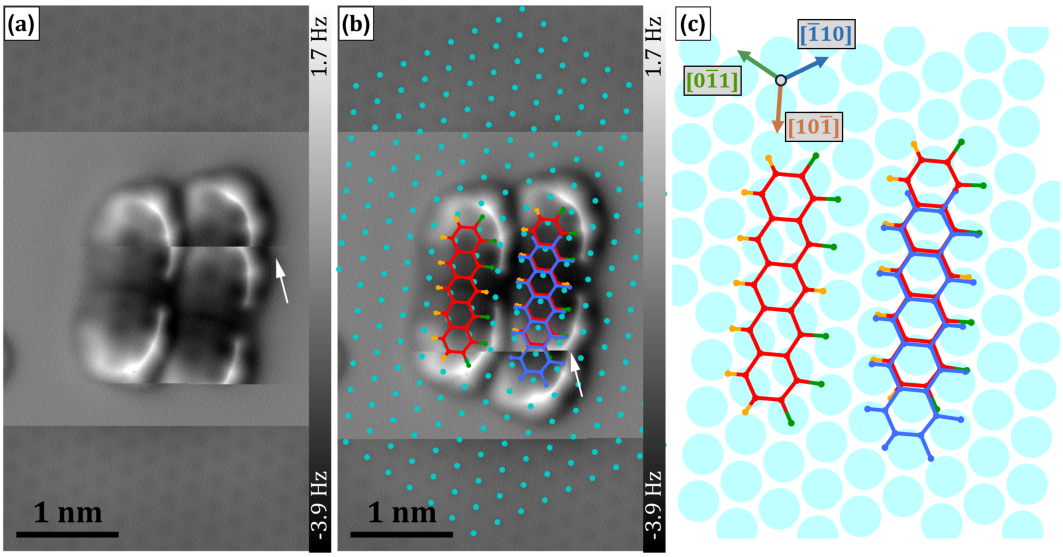


Figure A.11: High-resolution cc-AFM image of a F_6PEN dimer adsorbed on Cu(111) (T = 35 K). (a) Scan in upward direction and (b) consecutive scan in downward direction. Two different current setpoints were chosen to resolve the molecules as well as the underlying surface in the same image. The distorted image lines indicate a jump of one of the molecules and are highlighted by white arrows. (c) Sketch of the F_6PEN dimer on the Cu(111) surface. The fitted copper atoms are displayed in bright blue color. The two positions of the upper molecule are overlaid as red and blue F_6PEN structures, respectively. Imaging parameters: (a) and (b) $V_{g,surface}$ = 15 mV, $I_{t,surface}$ = 1050 pA and $V_{g,molecule}$ = 15 mV, $I_{t,molecule}$ = 45 pA.

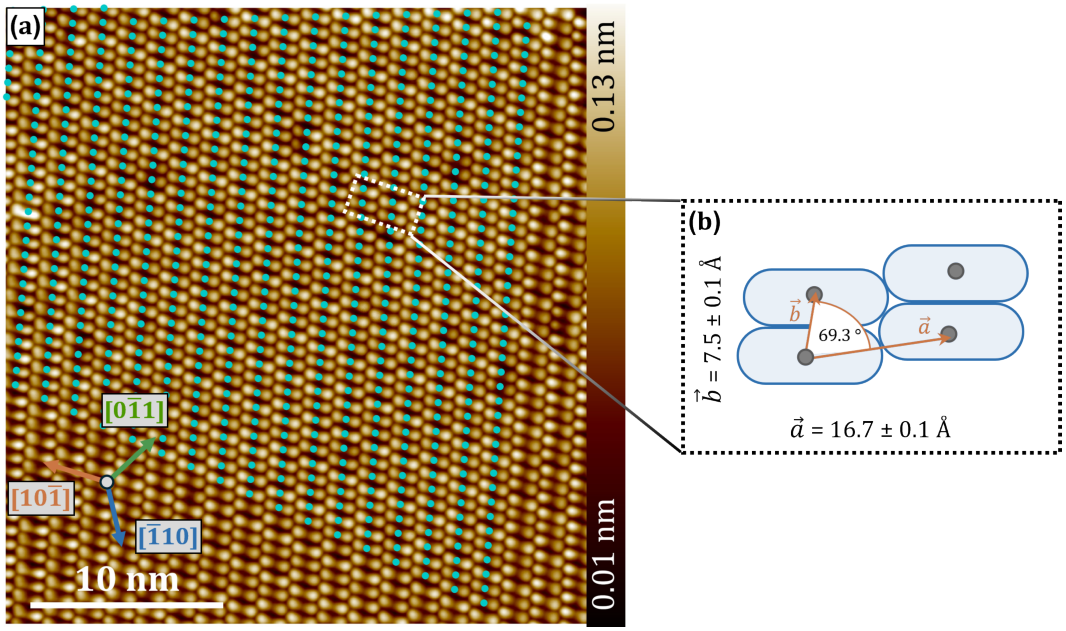


Figure A.12: STM overview image of a F_6PEN layer on Cu(111) ($T = 298\,\mathrm{K}$). The fitted lattice, represented as bright blue dots, is used to determine the lattice parameters. Imaging parameters: $V_g = 100\,\mathrm{mV}$, $I_t = 30\,\mathrm{pA}$. (b) Sketch of a crystal structure subunit showing the determined lattice parameters. The error for the angle is $\pm\,1\,^\circ$.

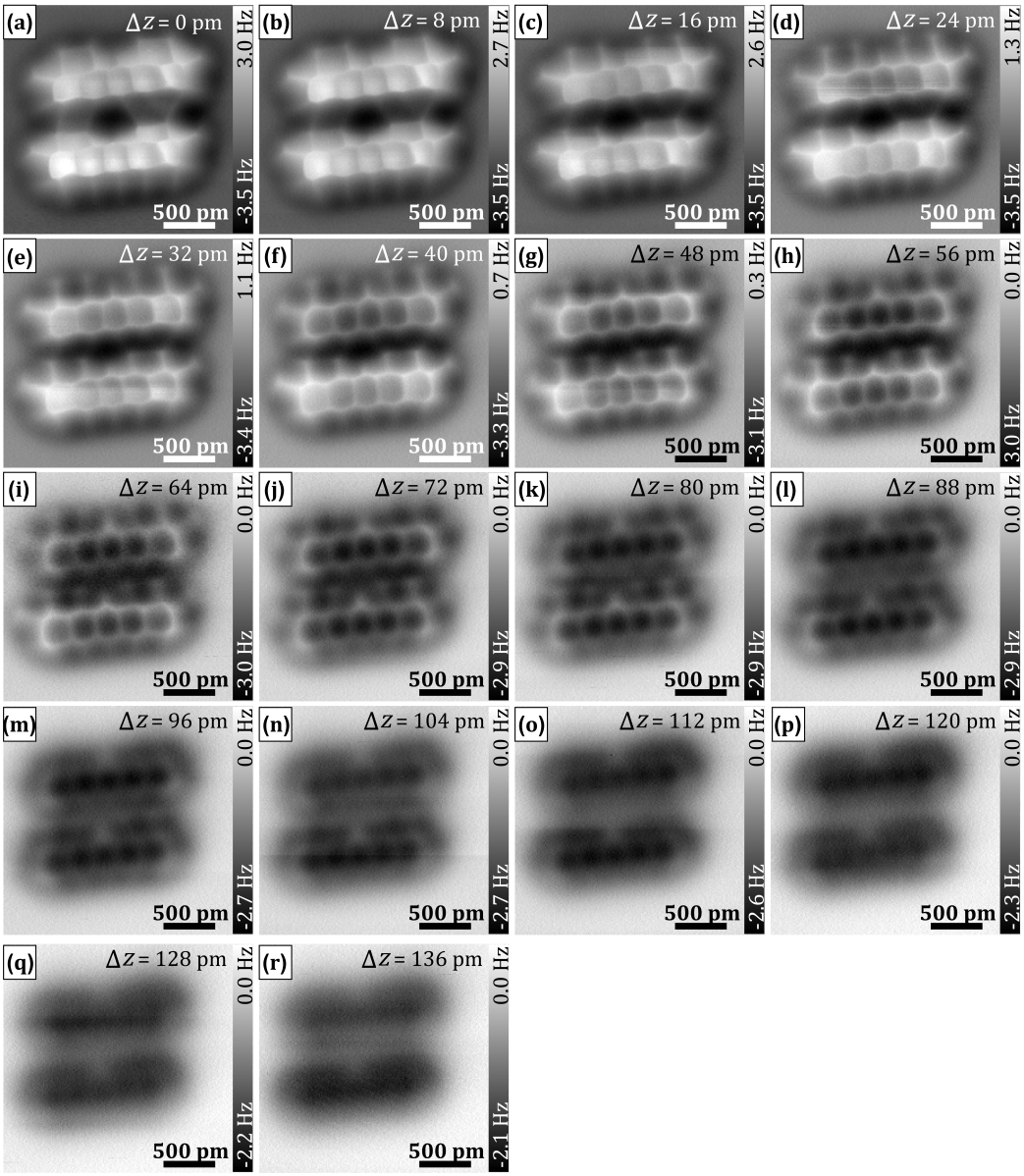


Figure A.13: Series of ch-AFM images used to generate the reconstructed topography image of the F_6PEN molecules on Au(111) ($T = 7\,\mathrm{K}$). The respective tip heights Δz displayed in the images are given with respect to the STM set-point of $V_\mathrm{g} = -0.57\,\mathrm{mV}$, $I_\mathrm{t} = 30\,\mathrm{pA}$. $\Delta z = 0\,\mathrm{pm}$ was set as minimum tip height.

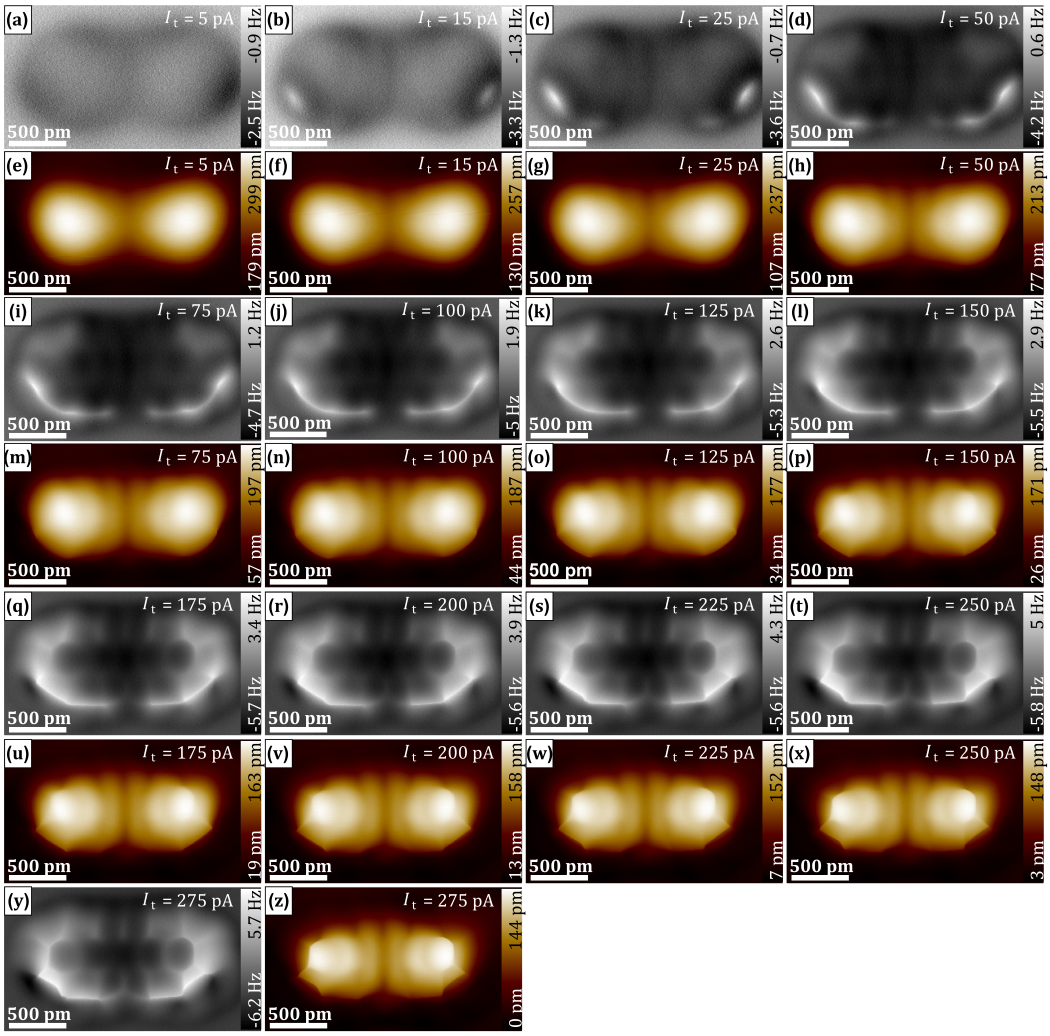


Figure A.14: Series of cc-AFM and simultaneously recorded STM images used to generate the reconstructed topography image of the F_6PEN molecule on Cu(111) (T = 7 K). The respective tunneling currents I_t displayed in the images are given with respect to a gap voltage of V_g = 20 mV.

Appendix B

Supplementary Information on Chapter 5

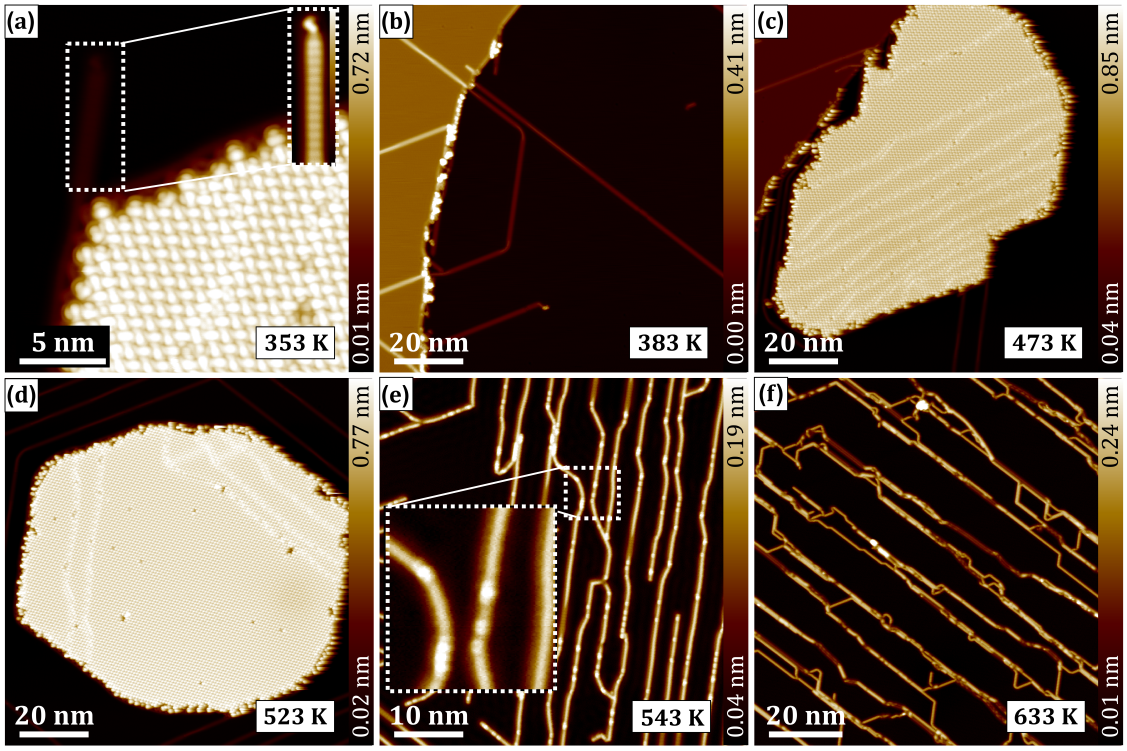


Figure B.1: Overview of further reaction temperatures of (6)CPP on Cu(111). STM images are taken after subsequent sample annealing to (a) $T = 353\,\mathrm{K}$, (b) $T = 383\,\mathrm{K}$, (c) $T = 473\,\mathrm{K}$, (d) $T = 523\,\mathrm{K}$, (e) $T = 543\,\mathrm{K}$ and (f) $T = 633\,\mathrm{K}$. Imaging parameters: (a) $V_\mathrm{g} = 100\,\mathrm{mV}$, $I_\mathrm{t} = 10\,\mathrm{pA}$; height bar inlet: Upper: 0.10 nm. Lower: 0.01 nm. (b) $V_\mathrm{g} = 500\,\mathrm{mV}$, $I_\mathrm{t} = 5\,\mathrm{pA}$, (c) $V_\mathrm{g} = 500\,\mathrm{mV}$, $I_\mathrm{t} = 5\,\mathrm{pA}$, (d) $V_\mathrm{g} = 500\,\mathrm{mV}$, $I_\mathrm{t} = 5\,\mathrm{pA}$, (e) $V_\mathrm{g} = 100\,\mathrm{mV}$, $I_\mathrm{t} = 5\,\mathrm{pA}$ and (f) $V_\mathrm{g} = 500\,\mathrm{mV}$, $I_\mathrm{t} = 5\,\mathrm{pA}$. Thanks to Qigang Zhong for conducting the experiments of (6)CPP on Cu(111).

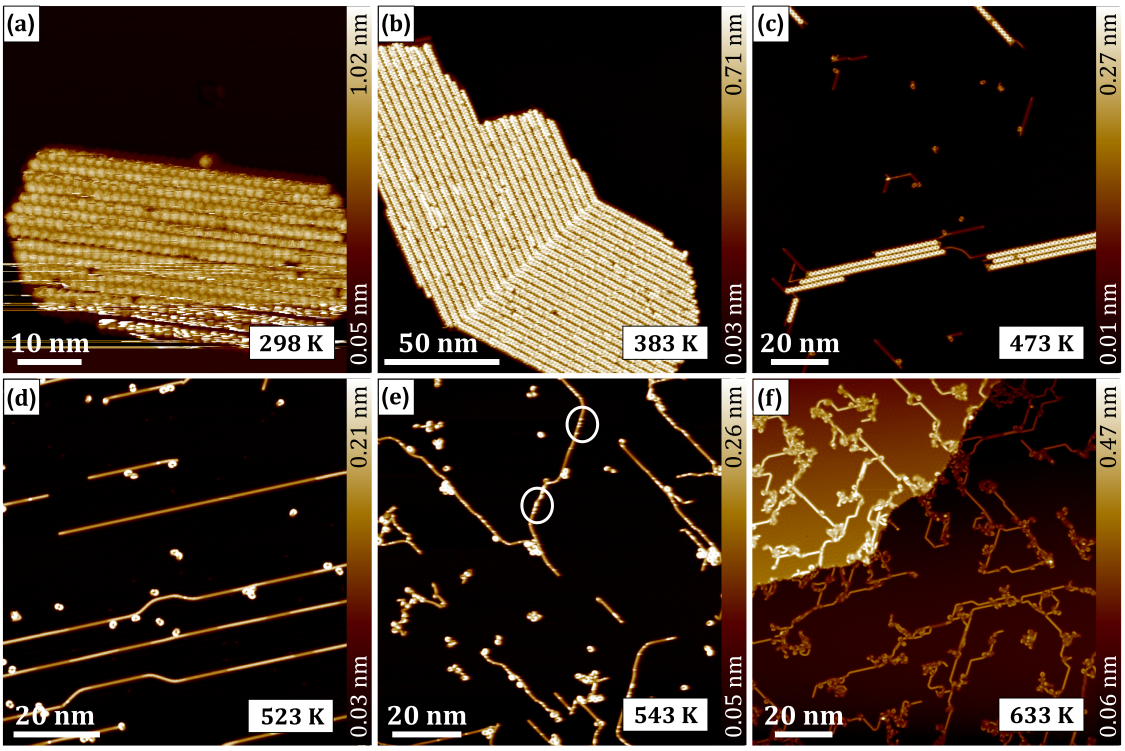


Figure B.2: Overview of further reaction temperatures of (8)CPP on Cu(111). STM images are taken after subsequent sample annealing to (a) $T = 298\,\mathrm{K}$, (b) $T = 383\,\mathrm{K}$, (c) $T = 473\,\mathrm{K}$, (d) $T = 523\,\mathrm{K}$, (e) $T = 543\,\mathrm{K}$ and (f) $T = 633\,\mathrm{K}$. Imaging parameters: (a) $V_\mathrm{g} = 100\,\mathrm{mV}$, $I_\mathrm{t} = 10\,\mathrm{pA}$, (b) $V_\mathrm{g} = 100\,\mathrm{mV}$, $I_\mathrm{t} = 10\,\mathrm{pA}$, (c) $V_\mathrm{g} = 100\,\mathrm{mV}$, $I_\mathrm{t} = 10\,\mathrm{pA}$; molecules were evaporated for 2.5 min instead of 2 min, (d) $V_\mathrm{g} = 100\,\mathrm{mV}$, $I_\mathrm{t} = 10\,\mathrm{pA}$, (e) $V_\mathrm{g} = 100\,\mathrm{mV}$, $I_\mathrm{t} = 10\,\mathrm{pA}$ and (f) $V_\mathrm{g} = 100\,\mathrm{mV}$, $I_\mathrm{t} = 10\,\mathrm{pA}$. The bright protrusions encircled in (e) indicate the onset of the benzyne formation within PPP chains. For comparison see Figure B.1 (e) and Figure B.4.

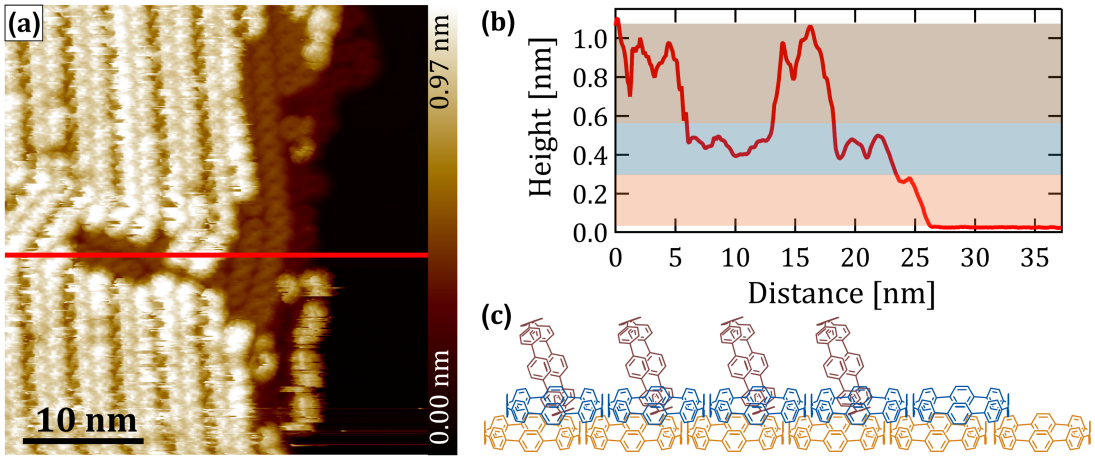


Figure B.3: (a) STM image of (8)CPP multilayers on Cu(111) ($T = 383\,\mathrm{K}$). Imaging parameters: $V_\mathrm{g} = 100\,\mathrm{mV}$, $I_\mathrm{t} = 10\,\mathrm{pA}$. (b) Corresponding line profile indicating three molecular layers of different heights. (c) Proposed arrangement of the (8)CPP multilayers on the Cu(111) substrate.

Figure B.3 (a) shows a STM overview image of at least three (8)CPP layers on the Cu(111) surface. The STM image clearly reveals that the first two layers consist of flat-lying (8)CPP molecules. This agrees well with the first two steps of the line profile highlighted in orange and blue in Figure B.3 (b), which both show an apparent height of approximately 0.25 nm. The third layer has a higher apparent height of about 0.5 nm (highlighted by a brown bar), indicating a different adsorption configuration compared to the first two layers. However, the determined height does not match the measured size of the molecules of 1.02 nm, as derived by the cc-AFM measurements in Figure B.5. This allows at least two different conclusions to be drawn when interpreting the conformation of the top layer. The molecules could stand (approximately) upright and sink into the openings of the flat-lying molecules (exemplified in Figure B.3 (c)) and therefore exhibit a lower height compared to the determined size of the molecules in Figure B.5. At this point, it needs to be emphasized that the apparent height derived by the STM does not correspond to the physical height of the molecules, because the measured current in STM is a function of the sample's local density of states [61]. Therefore, due to the two lower (8)CPP layers, which could potentially act as buffer layers, the upper (8)CPP layer could be partially electronically decoupled from the copper substrate. This could influence the layer's electronic properties, making it not possible to draw a conclusion about the exact adsorption geometry from the derived STM data.

Figure B.4 (a) shows a magnified STM image of a PPP chain with two bright protrusions, exemplified by white circles in the overview STM image in Figure B.2 (e). The cc-AFM image in Figure B.4 (b) reveals a benzenoid-type PPP chain with two bright, halo-like protrusions, which can be assigned to the formation of benzynes within the PPP chain. For comparison of AFM image contrasts of benzynes in constant height and constant current mode, see Figure 5.8 (a) and (d) and Figure B.8.

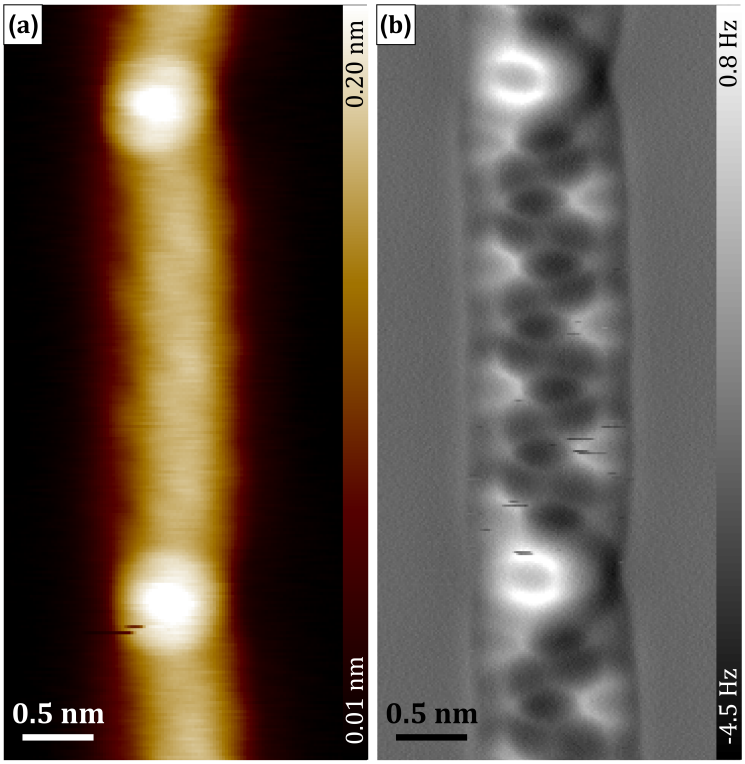


Figure B.4: Transition to benzyne formation within PPP chains ($T = 533\,\mathrm{K}$). (a) STM image of a PPP chain with two bright protrusions, indicating the formation of two benzyne units within the chain. (b) Corresponding cc-AFM image, resolving the two benzynes within the chain. Imaging parameters: (a) $V_\mathrm{g} = 100\,\mathrm{mV}$, $I_\mathrm{t} = 10\,\mathrm{pA}$ and (b) $V_\mathrm{g} = 20\,\mathrm{mV}$, $I_\mathrm{t} = 20\,\mathrm{pA}$.

As shown in Figure B.5, the size of an (8)CPP molecule adsorbed on the Cu(111) surface was determined to be approximately 1.023 nm. This corresponds well with the size of the free molecule (1.089 nm) [229].

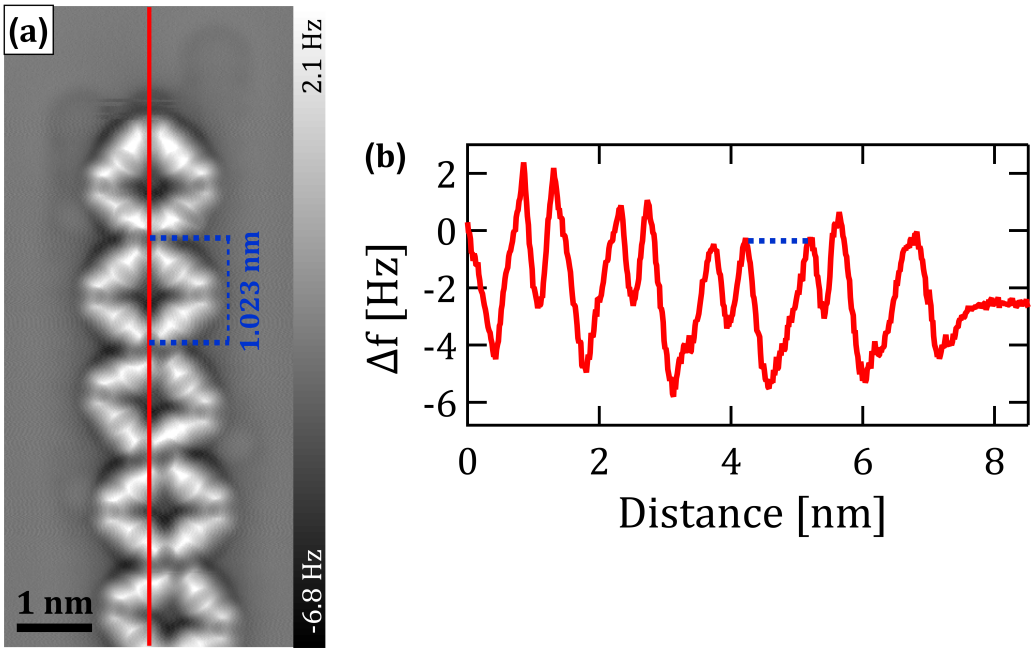


Figure B.5: (a) cc-AFM image of a row of five (8)CPP molecules ($T = 423\,\mathrm{K}$). Imaging parameters: $V_\mathrm{g} = 50\,\mathrm{mV}$, $I_\mathrm{t} = 12\,\mathrm{pA}$. (b) Corresponding line profile, highlighted by a red bar in (a).

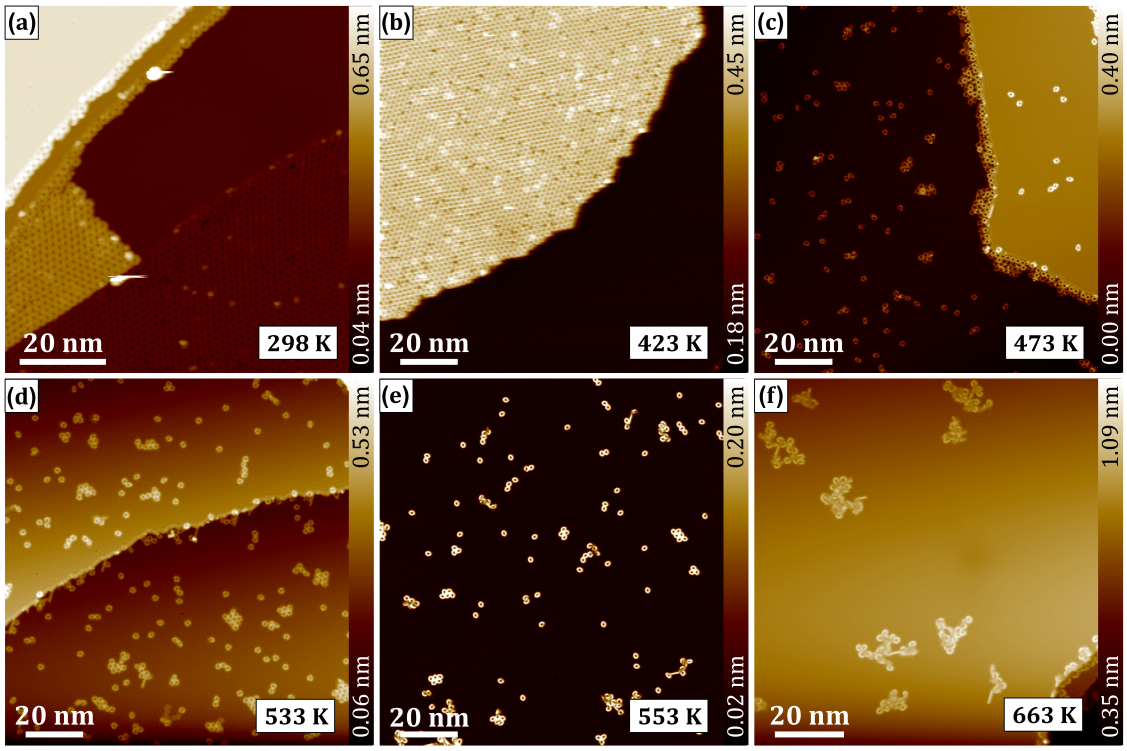


Figure B.6: Overview of further reaction temperatures of (10)CPP on Cu(111). STM images are taken after subsequent sample annealing to (a) $T = 298\,\mathrm{K}$, (b) $T = 423\,\mathrm{K}$, (c) $T = 473\,\mathrm{K}$, (d) $T = 533\,\mathrm{K}$, (e) $T = 553\,\mathrm{K}$ and (f) $T = 663\,\mathrm{K}$. Imaging parameters: (a) $V_\mathrm{g} = 100\,\mathrm{mV}$, $I_\mathrm{t} = 5\,\mathrm{pA}$, (b) $V_\mathrm{g} = 100\,\mathrm{mV}$, $I_\mathrm{t} = 10\,\mathrm{pA}$, (c) $V_\mathrm{g} = 100\,\mathrm{mV}$, $I_\mathrm{t} = 10\,\mathrm{pA}$, (d) $V_\mathrm{g} = 100\,\mathrm{mV}$, $I_\mathrm{t} = 10\,\mathrm{pA}$, (e) $V_\mathrm{g} = 100\,\mathrm{mV}$, $I_\mathrm{t} = 10\,\mathrm{pA}$ and (f) $V_\mathrm{g} = 100\,\mathrm{mV}$, $I_\mathrm{t} = 10\,\mathrm{pA}$.

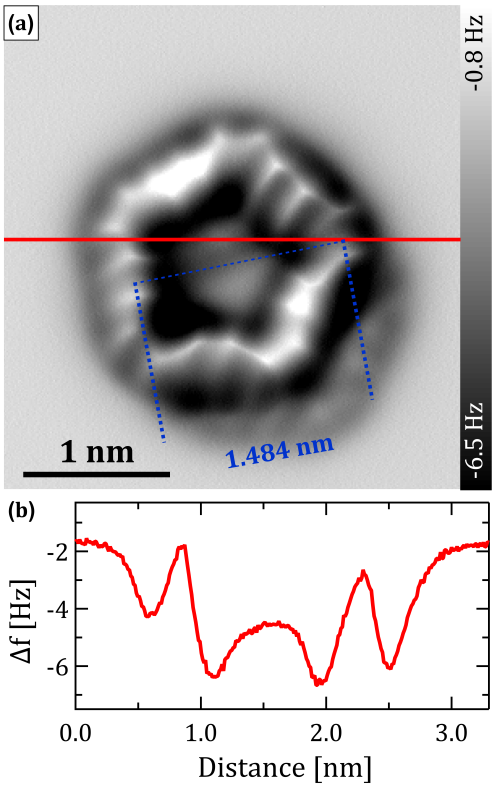


Figure B.7: (a) ch-AFM image of an isolated (10)CPP molecule on the Cu(111) surface after deposition ($T = 7\,\mathrm{K}$). Imaging parameters: $\Delta z = +105\,\mathrm{pm}$ with respect to the STM setpoint of $V_\mathrm{g} = -0.57\,\mathrm{mV}$, $I_\mathrm{t} = 15\,\mathrm{pA}$. (b) Corresponding line profile, highlighted by a red bar in (a).

As shown in Figure B.7, the size of a (10)CPP molecule adsorbed on the Cu(111) surface was determined to be approximately 1.484 nm. This corresponds well with the size of the free molecule (1.374 nm) [229].

Figure B.8 compares the appearance of benzynes in constant current and constant height AFM measurements. In cc-AFM measurements, the benzynes appear as a halo-like protrusion (see Figure B.8 (a)), whereas in the ch-AFM image, two dots per benzyne show up (see Figure B.8 (b)) [226]. Note that not all of the phenyl rings in Figure B.8 have transformed into benzynes yet, some hydrogenated rings seem to be rotated towards the Cu(111) surface.

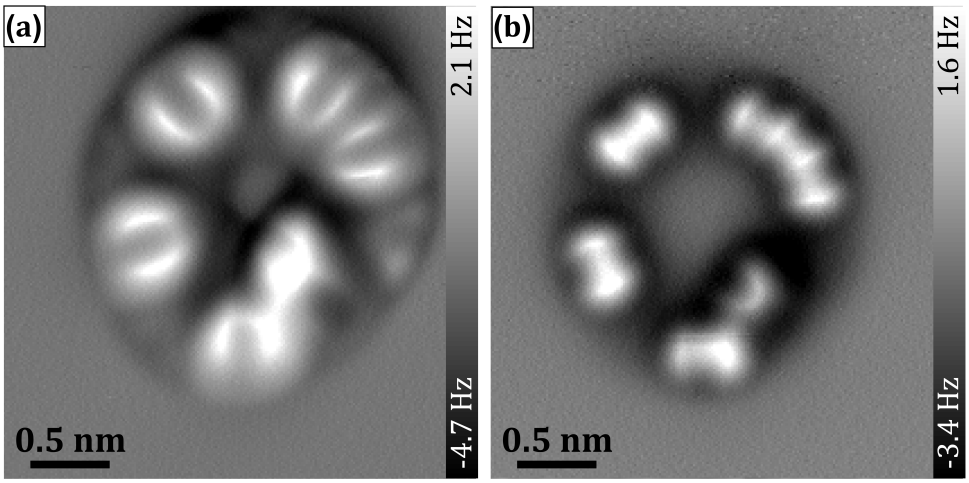


Figure B.8: (a) cc-AFM and (b) ch-AFM image of a (10)CPP molecule with benzynes formed within the cycloparaphenylene ($T = 473\,\mathrm{K}$). Imaging parameters: (a) $V_\mathrm{g} = 100\,\mathrm{mV}$, $I_\mathrm{t} = 200\,\mathrm{pA}$ and (b) $\Delta z = +10\,\mathrm{pm}$ with respect to the STM setpoint of $V_\mathrm{g} = -0.57\,\mathrm{mV}$, $I_\mathrm{t} = 10\,\mathrm{pA}$.

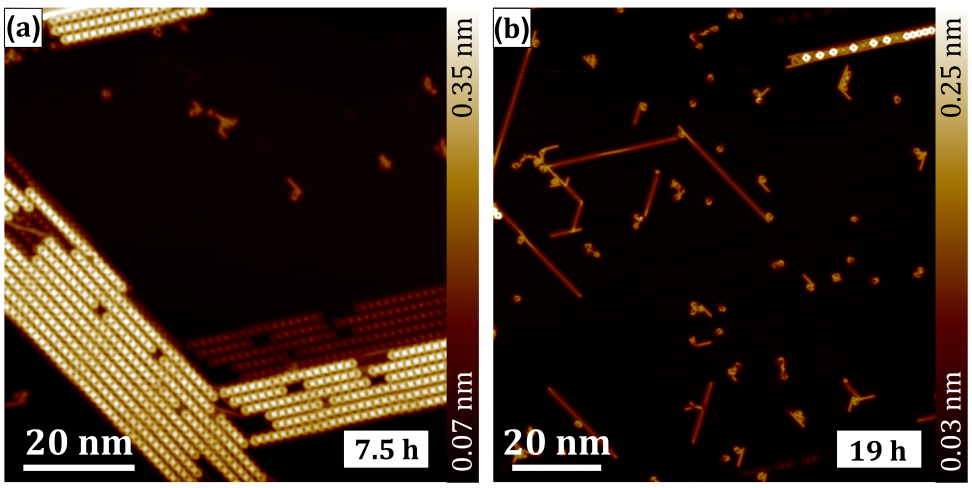


Figure B.9: STM images taken after long annealing at 388 K. Note that the temperature during annealing increased by approximately 37 K. (a) 7.5 hours annealing and (b) 19 hours annealing. Imaging parameters: (a) $V_\mathrm{g} = 100\,\mathrm{mV}$, $I_\mathrm{t} = 10\,\mathrm{pA}$ and (b) $V_\mathrm{g} = 100\,\mathrm{mV}$, $I_\mathrm{t} = 10\,\mathrm{pA}$.

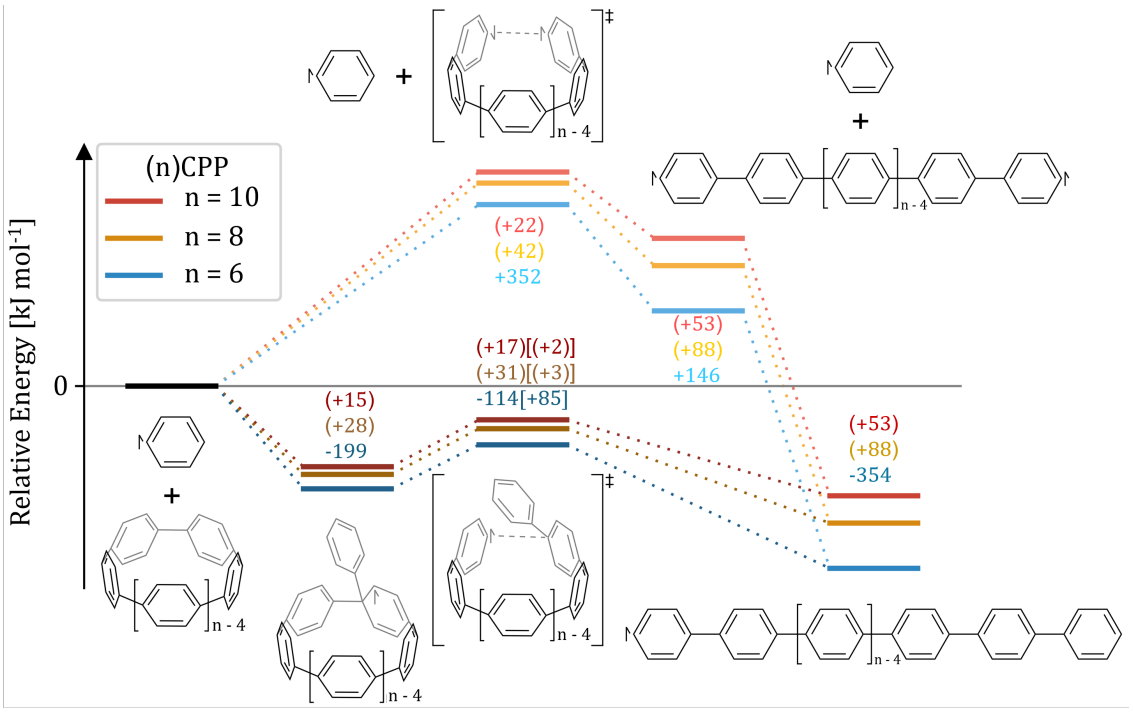


Figure B.10: Density functional theory calculated energy diagram for the cycloparaphenylenes in the gas phase, comparing the three different ring sizes. The upper path shows the direct unimolecular ring-opening, whereas the lower path shows the ring-opening by the attack of a phenyl radical. Thanks to Jakob Schramm and Ralf Tonner-Zech for the calculations.

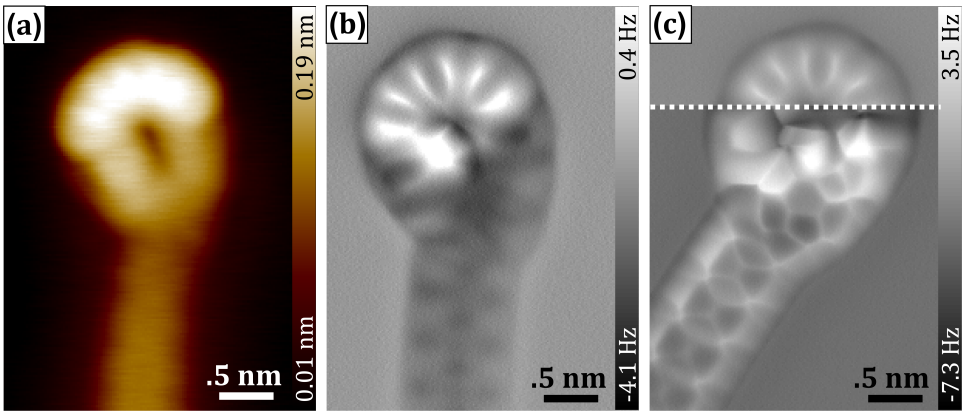


Figure B.11: Detailed investigation of a PPP chain with CPP terminated chain end (T = 483 K). (a) STM image of an (8)CPP fusing to a PPP chain. (b) and (c) cc-AFM images of the structure shown in the STM image. Setpoints were varied to resolve the whole structure. Imaging parameters: (a) V_g = 100 mV, I_t = 10 pA and (b) V_g = 50 mV, I_t = 55 pA. (c) Upper part: V_g = 20 mV, I_t = 30 pA. Lower part: V_g = 20 mV, I_t = 260 pA. The setpoint change is indicated by a white dashed line.

Figure B.11 shows STM and AFM images of an (8)CPP ring, which seems to be attached to the end of a PPP chain. Due to the height differences of the flat-lying and upright standing phenyl units, the structure is imaged in Figure B.11 (c) using two different current setpoints. The complex three-dimensional adsorption structure makes it difficult to determine an exact molecular structure, but a covalent bond between chain and ring can be anticipated. The observed structure might be an intermediate state, whereas a radical attacks an unopened ring (second structure in the lower path of Figure B.10), whereby the ring did not open yet. However, it might also indicate the termination of the on-surface reaction, as the experimental data do not clarify whether rings bound to the surface can still open and contribute to the ROP.

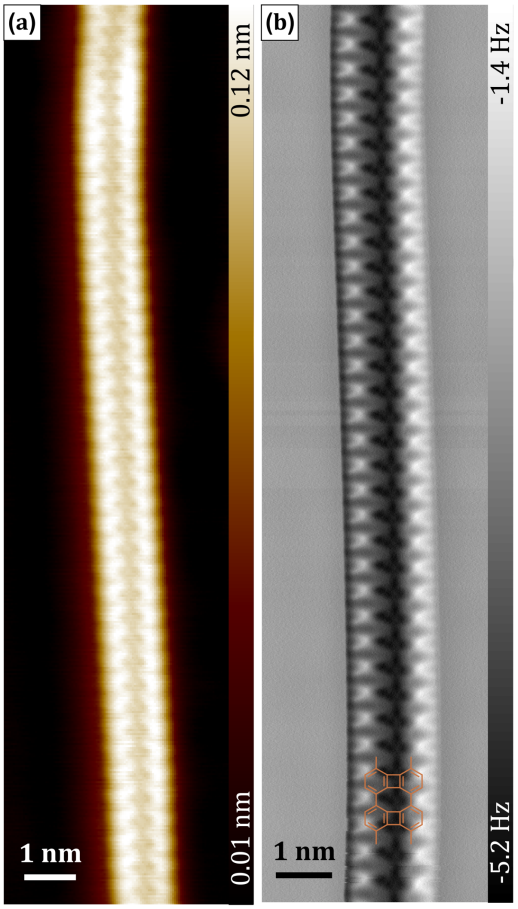


Figure B.12: (a) STM and (b) cc-AFM image of a long (at least 15.8 nm) BNR formed by the on-surface reaction of opened (8)CPP molecules ($T = 583\,\mathrm{K}$). Imaging parameters: (a) $V_\mathrm{g} = 100\,\mathrm{mV}$, $I_\mathrm{t} = 10\,\mathrm{pA}$ and (b) $V_\mathrm{g} = 20\,\mathrm{mV}$, $I_\mathrm{t} = 110\,\mathrm{pA}$.

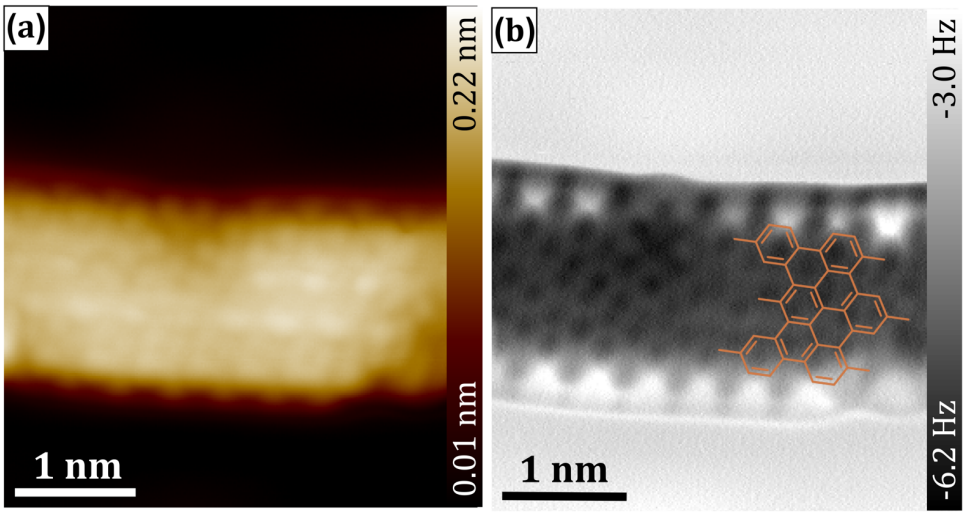


Figure B.13: (a) STM and (b) cc-AFM image of a 9-AGNR formed by the on-surface reaction of opened (8)CPP molecules ($T = 703\,\mathrm{K}$). Imaging parameters: (a) $V_\mathrm{g} = 50\,\mathrm{mV}$, $I_\mathrm{t} = 60\,\mathrm{pA}$ and (b) $V_\mathrm{g} = 50\,\mathrm{mV}$, $I_\mathrm{t} = 60\,\mathrm{pA}$.

List of Figures

2.1 General Scanning Probe Microscopy Setup and Working Principle 3
2.2 Schemes of Tunneling for a Simplified Vacuum Barrier and a Tunneling Junction in STM 5
2.3 Comparison of Constant Current and Constant Height Mode in STM 7
2.4 Sketch of the Lennard-Jones Potential, Including Attractive and Repulsive Components as well as the Resulting Force 9
2.5 General Setup of Atomic Force Microscopy 12
2.6 Amplitude and Phase Response of a Driven, Damped Harmonic Oscillator Under the Influence of Forces 15
2.7 Setup of the Chemical Bond Imaging Method, Exemplified for a F_6PEN Molecule Investigated Using Combined STM and AFM Measurements . . . 17
2.8 Sketch of the Thermally Induced Self-Assembly Process of Organic Molecules on a Metal Surface 20
2.9 Sketch of the Halogen Bond Featuring σ-hole and Types of Halogen Bonds 22
2.10 Sketch of the On-Surface Ullmann Reaction Involving Halogenated Benzene Molecules 25

3.1 Setup of the Low Temperature Scanning Probe Microscope 28

4.1 Overview of the Temperature Induced Self-Assembly Process of F_6PEN on Au(111) Investigated by STM 36
4.2 Overview of Different Sizes of F_6PEN Clusters on Au(111) Investigated by AFM 39
4.3 Comparison of Experimental AFM Data Recorded on Au(111) and Calculated Crystal Structure of F_6PEN 42
4.4 Investigation of an Alternative Crystal Structure by STM and AFM, in Which F_6PEN Molecules in Adjacent Lines Show in Different Directions . . 44
4.5 Overview of the Temperature Induced Self-Assembly Process of F_6PEN on Cu(111) Investigated by STM 46
4.6 Investigation of Tetramer Structures Inside the F_6PEN Monolayer on Cu(111) 48
4.7 Comparison of the Bending of F_6PEN on Au(111) and Cu(111) 50

5.1 Scheme of the Reaction Mechanism of Cycloparaphenylene Molecules on Cu(111) 56
5.2 Overview of the Reaction of (6)CPP on Cu(111) 58
5.3 Overview of the Reaction of (8)CPP on Cu(111) 60
5.4 Overview of the Reaction of (10)CPP on Cu(111) 63
5.5 Probe Particle Model Simulation: Comparison of Experimental and Simulated AFM Images for (8)CPP and (10)CPP 65

5.6 Comparison of the Benzenoid-Type and Quinoid-Type Poly(*Para*-Phenylene) Chains 67
5.7 Comparison of the Reaction Paths of (6)CPP, (8)CPP and (10)CPP as a Function of the Temperature 69
5.8 Constant Height and Constant Current AFM Images of Benzyne Chains, Biphenylene Nanoribbons and Graphene Nanoribbons 71

List of Tables

3.1 Parameters for Cleaning the Au(111) Single Crystal 29
3.2 Parameters for Cleaning the Cu(111) Single Crystal 29

4.1 Distances and Angles of H-F Interactions in the Dimer Structure 38
4.2 Distances and Angles of H-F Interactions of Molecules in Adjacent Molecule Lines 43
4.3 Distances and Angles of H-F Interactions of Molecules in the Alternative Crystal Structure 45

Bibliography

[1] R. P. Feynman, *There's Plenty of Room at the Bottom*, *Engineering and Science*, Vol. 23 (5) (**1960**) 22–36.

[2] G. Binnig et al., *Surface Studies by Scanning Tunneling Microscopy*, *Physical Review Letters*, Vol. 49(1) (**1982**) 57–61.

[3] G. Binnig & H. Rohrer, *Scanning tunneling microscopy*, *Surface Science*, Vol. 126(1–3) (**1983**) 236–244.

[4] G. Binnig et al., *7 × 7 Reconstruction on Si(111) Resolved in Real Space*, *Physical Review Letters*, Vol. 50(2) (**1983**) 120–123.

[5] A. M. Baró et al., *Real-Space Observation of the 2×1 Structure of Chemisorbed Oxygen on Ni(110) by Scanning Tunneling Microscopy*, *Physical Review Letters*, Vol. 52(15) (**1984**) 1304–1307.

[6] J. A. Stroscio & D. M. Eigler, *Atomic and Molecular Manipulation with the Scanning Tunneling Microscope*, *Science*, Vol. 254(5036) (**1991**) 1319–1326.

[7] G. Binnig et al., *Atomic Force Microscope*, *Physical Review Letters*, Vol. 56(9) (**1986**) 930–933.

[8] G. Binnig et al., *Atomic Resolution with Atomic Force Microscope*, *Europhysics Letters (EPL)*, Vol. 3(12) (**1987**) 1281–1286.

[9] H. Ohtani et al., *Scanning Tunneling Microscopy Observations of Benzene Molecules on the Rh(111)-(3 × 3) (C_6H_6+ 2CO) Surface*, *Physical Review Letters*, Vol. 60(23) (**1988**) 2398–2401.

[10] R. Otero et al., *Molecular Self-Assembly at Solid Surfaces*, *Advanced Materials*, Vol. 23(44) (**2011**) 5148–5176.

[11] A. Kühnle, *Self-assembly of organic molecules at metal surfaces*, *Current Opinion in Colloid and Interface Science*, Vol. 14(2) (**2009**) 157–168.

[12] M. Mas-Torrent & C. Rovira, *Role of Molecular Order and Solid-State Structure in Organic Field-Effect Transistors*, *Chemical Reviews*, Vol. 111(8) (**2011**) 4833–4856.

[13] L. Grill et al., *Nano-architectures by covalent assembly of molecular building blocks*, *Nature Nanotechnology*, Vol. 2(11) (**2007**) 687–691.

[14] Q. Zhong et al., *Benzo-Fused Periacenes or Double Helicenes? Different Cyclodehydrogenation Pathways on Surface and in Solution*, *Journal of the American Chemical Society*, Vol. 141(18) (**2019**) 7399–7406.

[15] M. Sarker et al., *Porous Nanographenes, Graphene Nanoribbons, and Nanoporous Graphene Selectively Synthesized from the Same Molecular Precursor*, *Journal of the American Chemical Society*, Vol. 146(21) (**2024**) 14453–14467.

[16] L. Gross et al., *The Chemical Structure of a Molecule Resolved by Atomic Force Microscopy*, *Science*, Vol. 325(5944) (**2009**) 1110–1114.

[17] D. G. de Oteyza et al., *Direct Imaging of Covalent Bond Structure in Single-Molecule Chemical Reactions*, *Science*, Vol. 340(6139) (**2013**) 1434–1437.

[18] P. Ruffieux et al., *On-surface synthesis of graphene nanoribbons with zigzag edge topology*, *Nature*, Vol. 531(7595) (**2016**) 489–492.

[19] C. Moreno et al., *Bottom-up synthesis of multifunctional nanoporous graphene*, *Science*, Vol. 360(6385) (**2018**) 199–203.

[20] O. Gröning et al., *Engineering of robust topological quantum phases in graphene nanoribbons*, *Nature*, Vol. 560(7717) (**2018**) 209–213.

[21] Q. Fan et al., *Biphenylene network: A nonbenzenoid carbon allotrope*, *Science*, Vol. 372(6544) (**2021**) 852–856.

[22] Q. Fan et al., *Nanoribbons with Nonalternant Topology from Fusion of Polyazulene: Carbon Allotropes beyond Graphene*, *Journal of the American Chemical Society*, Vol. 141(44) (**2019**) 17713–17720.

[23] B. Mallada et al., *On-Surface Strain-Driven Synthesis of Nonalternant Non-Benzenoid Aromatic Compounds Containing Four- to Eight-Membered Rings*, *Journal of the American Chemical Society*, Vol. 143(36) (**2021**) 14694–14702.

[24] Q. Fan et al., *Precise Monoselective Aromatic C–H Bond Activation by Chemisorption of Meta-Aryne on a Metal Surface*, *Journal of the American Chemical Society*, Vol. 140(24) (**2018**) 7526–7532.

[25] Q. Fan et al., *On-Surface Synthesis and Characterization of a Cycloarene: C108 Graphene Ring*, *Journal of the American Chemical Society*, Vol. 142(2) (**2019**) 894–899.

[26] K. Xu et al., *On-Surface Synthesis of a Nonplanar Porous Nanographene*, *Journal of the American Chemical Society*, Vol. 141(19) (**2019**) 7726–7730.

[27] F. Xiang et al., *Planar π-extended cycloparaphenylenes featuring an all-armchair edge topology*, *Nature Chemistry*, Vol. 14(8) (**2022**) 871–876.

[28] N. Pavliček et al., *On-surface generation and imaging of arynes by atomic force microscopy*, *Nature Chemistry*, Vol. 7(8) (**2015**) 623–628.

[29] N. Pavliček et al., *Synthesis and characterization of triangulene*, *Nature Nanotechnology*, Vol. 12(4) (**2017**) 308–311.

[30] K. Kaiser et al., *An sp-hybridized molecular carbon allotrope, cyclo[18]carbon*, *Science*, Vol. 365(6459) (**2019**) 1299–1301.

[31] X.-Y. Wang et al., *Precision synthesis versus bulk-scale fabrication of graphenes*, *Nature Reviews Chemistry*, Vol. 2(1) (**2017**).

[32] Z. Chen et al., *Graphene Nanoribbons: On-Surface Synthesis and Integration into Electronic Devices*, *Advanced Materials*, Vol. 32(45) (**2020**).

[33] Y. Gu et al., *Nanographenes and Graphene Nanoribbons as Multitalents of Present and Future Materials Science*, *Journal of the American Chemical Society*, Vol. 144(26) (**2022**) 11499–11524.

[34] M. Y. Han et al., *Energy Band-Gap Engineering of Graphene Nanoribbons*, *Physical Review Letters*, Vol. 98(20) (**2007**) 206805.

[35] Y.-C. Chen et al., *Tuning the Band Gap of Graphene Nanoribbons Synthesized from Molecular Precursors*, *ACS Nano*, Vol. 7(7) (**2013**) 6123–6128.

[36] S. Clair & D. G. de Oteyza, *Controlling a Chemical Coupling Reaction on a Surface: Tools and Strategies for On-Surface Synthesis*, *Chemical Reviews*, Vol. 119(7) (**2019**) 4717–4776.

[37] Q. Shen et al., *Frontiers of on-surface synthesis: From principles to applications*, *Nano Today*, Vol. 13 (**2017**) 77–96.

[38] B. Voigtländer, *Technical Aspects of Scanning Probe Microscopy*, Springer Berlin Heidelberg (**2015**), Pages 31–63.

[39] H. Bubert & H. Jenett, *Surface and thin film analysis*, Wiley-VCH, Weinheim (**2002**).

[40] S. N. Magonov, *Surface analysis with STM and AFM*, Wiley-VCH, Weinheim (**2008**).

[41] V. V. Tsukruk, *Scanning Probe Microscopy of Soft Matter*, Wiley-VCH, Weinheim, 1st Edition (**2012**).

[42] R. Howland & L. Benatar, *A Practical Guide: To Scanning Probe Microscopy*, *Park scientific instruments* (**1993**).

[43] F. Gołek et al., *AFM image artifacts*, *Applied Surface Science*, Vol. 304 (**2014**) 11–19.

[44] S. V. Kalinin & A. Gruverman, *Scanning Probe Microscopy*, SpringerLink, Springer, New York, (**2007**).

[45] G. Binnig & H. Rohrer, *Scanning tunneling microscopy—from birth to adolescence*, *Reviews of Modern Physics*, Vol. 59(3) (**1987**) 615–625.

[46] *Nobel Prize Outreach AB 2024. Mon. 14 Oct 2024. <https://www.nobelprize.org/prizes/physics/1986/press-release/>* (**1986**).

[47] B. Bhushan, *Springer Handbook of Nanotechnology*, Springer, Berlin, 2nd Edition (**2010**).

[48] Y. Hasegawa, *Scanning Tunneling Microscopy*, Springer Singapore (**2018**), Pages 599–604.

[49] D. J. O'Connor, *Surface Analysis Methods in Materials Science*, Springer Series in Surface Sciences, Springer, Berlin, Heidelberg, 1st Edition (**1992**).

[50] P. K. Hansma & J. Tersoff, *Scanning tunneling microscopy*, *Journal of Applied Physics*, Vol. 61(2) (**1987**) R1–R24.

[51] M. Bartelmann, *Theoretische Physik*, SpringerLink, Springer Spektrum, Berlin, Heidelberg (**2015**).

[52] B. Voigtländer, *Introduction*, Springer Berlin Heidelberg (**2015**), Pages 1–11.

[53] J.-F. Jia et al., *Scanning Tunneling Microscopy*, Kluwer Academic Publishers, Pages 55–112.

[54] B. Voigtländer, *Scanning Tunneling Microscopy*, Springer Berlin Heidelberg (**2015**), Pages 279–308.

[55] H. Reinhardt, *Quantenmechanik 1: Pfadintegralformulierung und Operatorformalismus*, Oldenbourg Wissenschaftsverlag (**2012**).

[56] J. C. Vickerman, *Surface analysis*, Wiley, Chichester, 2nd Edition (**2009**).

[57] M. Bowker, *Scanning Tunneling Microscopy in Surface Science, Nanoscience, and Catalysis*, John Wiley and Sons, Incorporated, Hoboken, 1st Edition (**2010**).

[58] G. Binnig et al., *Tunneling through a controllable vacuum gap*, *Applied Physics Letters*, Vol. 40(2) (**1982**) 178–180.

[59] D. M. Eigler & E. K. Schweizer, *Positioning single atoms with a scanning tunnelling microscope*, *Nature*, Vol. 344(6266) (**1990**) 524–526.

[60] J. Tersoff & D. R. Hamann, *Theory and Application for the Scanning Tunneling Microscope*, *Physical Review Letters*, Vol. 50(25) (**1983**) 1998–2001.

[61] J. Tersoff & D. R. Hamann, *Theory of the scanning tunneling microscope*, *Physical Review B*, Vol. 31(2) (**1985**) 805–813.

[62] R. J. Hamers et al., *Surface Electronic Structure of Si (111)-(7×7) Resolved in Real Space*, *Physical Review Letters*, Vol. 56(18) (**1986**) 1972–1975.

[63] L. Bartels et al., *Controlled vertical manipulation of single CO molecules with the scanning tunneling microscope: A route to chemical contrast*, *Applied Physics Letters*, Vol. 71(2) (**1997**) 213–215.

[64] R. Wiesendanger, *Scanning Probe Microscopy and Spectroscopy: Methods and Applications*, Cambridge University Press (**1994**).

[65] J. Wintterlin et al., *Real-time STM observations of atomic equilibrium fluctuations in an adsorbate system: O/Ru(0001)*, *Surface Science*, Vol. 394(1–3) (**1997**) 159–169.

[66] J. N. Israelachvili, *Intermolecular and surface forces*, Academic Press, Waltham, MA, 3rd Edition (**2011**).

[67] B. Voigtländer, *Forces Between Tip and Sample*, Springer Berlin Heidelberg (**2015**), Pages 145–155.

[68] X. Wang et al., *The Lennard-Jones potential: when (not) to use it*, *Physical Chemistry Chemical Physics*, Vol. 22(19) (**2020**) 10624–10633.

[69] S. Hunklinger, *Solid state physics*, Graduate, De Gruyter, Berlin (**2022**).

[70] H.-J. Butt, *Physics and chemistry of interfaces*, Wiley-VCH, Weinheim (**2003**).

[71] P. A. Tipler, *Tipler Physik*, Springer, Berlin, Heidelberg, 9th Edition (**2024**).

[72] H.-J. Butt, *Surface and interfacial forces*, Wiley-VCH, Weinheim, 2nd Edition (**2018**).

[73] V. A. Parsegian, *Van der Waals Forces: A Handbook for Biologists, Chemists, Engineers, and Physicists*, Cambridge University Press (**2005**).

[74] H.-J. Butt et al., *Force measurements with the atomic force microscope: Technique, interpretation and applications*, *Surface Science Reports*, Vol. 59(1–6) (**2005**) 1–152.

[75] C. J. Chen, *Atomic Forces*, Oxford University PressOxford (**2007**), Pages 93–122.

[76] J. Heintze & J. Pyrlik, *Lehrbuch zur Experimentalphysik Band 5: Quantenphysik*, Springer, Berlin, Heidelberg, 1st Edition (**2019**).

[77] L. Olsson et al., *A method for in situ characterization of tip shape in ac-mode atomic force microscopy using electrostatic interaction*, *Journal of Applied Physics*, Vol. 84(8) (**1998**) 4060–4064.

[78] Y. Seo & W. Jhe, *Atomic force microscopy and spectroscopy*, *Reports on Progress in Physics*, Vol. 71(1) (**2007**) 016101.

[79] F. J. Giessibl, *Advances in atomic force microscopy*, *Reviews of Modern Physics*, Vol. 75(3) (**2003**) 949–983.

[80] G. Meyer & N. M. Amer, *Novel optical approach to atomic force microscopy*, *Applied Physics Letters*, Vol. 53(12) (**1988**) 1045–1047.

[81] A. Schirmeisen et al., *Dynamic Modes of Atomic Force Microscopy*, Springer Berlin Heidelberg (**2011**), Pages 307–353.

[82] B. Voigtländer, *Static Atomic Force Microscopy*, Springer Berlin Heidelberg (**2015**), Pages 177–186.

[83] Y. Martin et al., *Atomic force microscope–force mapping and profiling on a sub 100-Å scale*, *Journal of Applied Physics*, Vol. 61(10) (**1987**) 4723–4729.

[84] B. Voigtländer, *Amplitude Modulation (AM) Mode in Dynamic Atomic Force Microscopy*, Springer Berlin Heidelberg (**2015**), Pages 187–204.

[85] B. Drake et al., *Imaging Crystals, Polymers, and Processes in Water with the Atomic Force Microscope*, *Science*, Vol. 243(4898) (**1989**) 1586–1589.

[86] T. Fukuma et al., *True atomic resolution in liquid by frequency-modulation atomic force microscopy*, *Applied Physics Letters*, Vol. 87(3) (**2005**).

[87] F. J. Giessibl, *Atomic Force Microscopy in Ultrahigh Vacuum*, *Japanese Journal of Applied Physics*, Vol. 33(6S) (**1994**) 3726.

[88] F. J. Giessibl, *Atomic Resolution of the Silicon (111)-(7×7) Surface by Atomic Force Microscopy*, *Science*, Vol. 267(5194) (**1995**) 68–71.

[89] D. Martin-Jimenez et al., *Bond-level imaging of organic molecules using Q-controlled amplitude modulation atomic force microscopy*, *Applied Physics Letters*, Vol. 117(13) (**2020**) 131601.

[90] C. A. J. Putman et al., *Tapping mode atomic force microscopy in liquid*, *Applied Physics Letters*, Vol. 64(18) (**1994**) 2454–2456.

[91] A. Schirmeisen et al., *Dynamic Modes of Atomic Force Microscopy*, Springer Berlin Heidelberg (**2007**), Pages 737–766.

[92] R. García, *Dynamic atomic force microscopy methods*, *Surface Science Reports*, Vol. 47(6–8) (**2002**) 197–301.

[93] T. R. Albrecht et al., *Frequency modulation detection using high-Q cantilevers for enhanced force microscope sensitivity*, *Journal of Applied Physics*, Vol. 69(2) (**1991**) 668–673.

[94] B. Voigtländer, *Harmonic Oscillator*, Springer Berlin Heidelberg (**2015**), Pages 15–29.

[95] C. Loppacher et al., *Fast digital electronics for application in dynamic force microscopy using high-Q cantilevers*, *Applied Physics A: Materials Science amp; Processing*, Vol. 66(7) (**1998**) 215–218.

[96] Y. Sugawara et al., *Defect Motion on an InP(110) Surface Observed with Noncontact Atomic Force Microscopy*, *Science*, Vol. 270(5242) (**1995**) 1646–1648.

[97] C. Sánchez-Sánchez et al., *Purely Armchair or Partially Chiral: Noncontact Atomic Force Microscopy Characterization of Dibromo-Bianthryl-Based Graphene Nanoribbons Grown on Cu(111)*, *ACS Nano*, Vol. 10(8) (**2016**) 8006–8011.

[98] L. Bartels et al., *The evolution of CO adsorption on Cu(111) as studied with bare and CO-functionalized scanning tunneling tips*, *Surface Science*, Vol. 432(3) (**1999**) L621–L626.

[99] Q. Zhong et al., *Noncontact atomic force microscopy: Bond imaging and beyond*, *Surface Science Reports*, Vol. 75(4) (**2020**) 100509.

[100] F. J. Giessibl, *High-speed force sensor for force microscopy and profilometry utilizing a quartz tuning fork*, *Applied Physics Letters*, Vol. 73(26) (**1998**) 3956–3958.

[101] F. J. Giessibl et al., *Stability considerations and implementation of cantilevers allowing dynamic force microscopy with optimal resolution: the qPlus sensor*, *Nanotechnology*, Vol. 15(2) (**2004**) S79–S86.

[102] L. Gross et al., *Atomic Force Microscopy for Molecular Structure Elucidation*, *Angewandte Chemie International Edition*, Vol. 57(15) (**2018**) 3888–3908.

[103] N. Moll et al., *The mechanisms underlying the enhanced resolution of atomic force microscopy with functionalized tips*, *New Journal of Physics*, Vol. 12(12) (**2010**) 125020.

[104] D. Martin-Jimenez et al., *Bond-Level Imaging of the 3D Conformation of Adsorbed Organic Molecules Using Atomic Force Microscopy with Simultaneous Tunneling Feedback*, *Physical Review Letters*, Vol. 122(19) (**2019**) 196101.

[105] Q. Zhong et al., *Constructing covalent organic nanoarchitectures molecule by molecule via scanning probe manipulation*, *Nature Chemistry*, Vol. 13(11) (**2021**) 1133–1139.

[106] H. Hölscher et al., *Quantitative analysis of dynamic-force-spectroscopy data on graphite(0001) in the contact and noncontact regimes*, *Physical Review B*, Vol. 61(19) (**2000**) 12678–12681.

[107] F. Giessibl, *Probing the Nature of Chemical Bonds by Atomic Force Microscopy*, *Molecules*, Vol. 26(13) (**2021**) 4068.

[108] P. Hapala et al., *Mechanism of high-resolution STM/AFM imaging with functionalized tips*, *Physical Review B*, Vol. 90(8) (**2014**) 085421.

[109] D. Ebeling et al., *London Dispersion Directs On-Surface Self-Assembly of [121]Tetramantane Molecules*, *ACS Nano*, Vol. 11(9) (**2017**) 9459–9466.

[110] D. Ebeling et al., *Assigning the absolute configuration of single aliphatic molecules by visual inspection*, *Nature Communications*, Vol. 9(1) (**2018**) 2420.

[111] F. Mohn et al., *Different tips for high-resolution atomic force microscopy and scanning tunneling microscopy of single molecules*, *Applied Physics Letters*, Vol. 102(7) (**2013**) 073109.

[112] J. van der Lit et al., *Submolecular Resolution Imaging of Molecules by Atomic Force Microscopy: The Influence of the Electrostatic Force*, *Physical Review Letters*, Vol. 116(9) (**2016**) 096102.

[113] B. Schuler et al., *Unraveling the Molecular Structures of Asphaltenes by Atomic Force Microscopy*, *Journal of the American Chemical Society*, Vol. 137(31) (**2015**) 9870–9876.

[114] B. Schuler et al., *Heavy Oil Based Mixtures of Different Origins and Treatments Studied by Atomic Force Microscopy*, *Energy and Fuels*, Vol. 31(7) (**2017**) 6856–6861.

[115] L. Gross et al., *Bond-Order Discrimination by Atomic Force Microscopy*, *Science*, Vol. 337(6100) (**2012**) 1326–1329.

[116] S. Zint et al., *Imaging Successive Intermediate States of the On-Surface Ullmann Reaction on Cu(111): Role of the Metal Coordination*, *ACS Nano*, Vol. 11(4) (**2017**) 4183–4190.

[117] D. Ebeling et al., *Adsorption Structure of Mono- and Diradicals on a Cu(111) Surface: Chemoselective Dehalogenation of 4-Bromo-3"-iodo-p-terphenyl*, *ACS Nano*, Vol. 13(1) (**2018**) 324–336.

[118] J. Tschakert et al., *Surface-controlled reversal of the selectivity of halogen bonds*, *Nature Communications*, Vol. 11(1) (**2020**) 5630.

[119] B. Schuler et al., *Adsorption Geometry Determination of Single Molecules by Atomic Force Microscopy*, *Physical Review Letters*, Vol. 111(10) (**2013**) 106103.

[120] G. M. Whitesides et al., *Molecular Self-Assembly and Nanochemistry: a Chemical Strategy for the Synthesis of Nanostructures*, *Science*, Vol. 254(5036) (**1991**) 1312–1319.

[121] G. M. Whitesides & B. Grzybowski, *Self-Assembly at All Scales*, *Science*, Vol. 295(5564) (**2002**) 2418–2421.

[122] D. Philp & J. F. Stoddart, *Self-Assembly in Natural and Unnatural Systems*, *Angewandte Chemie International Edition in English*, Vol. 35(11) (**1996**) 1154–1196.

[123] R. G. Nuzzo & D. L. Allara, *Adsorption of bifunctional organic disulfides on gold surfaces*, *Journal of the American Chemical Society*, Vol. 105(13) (**1983**) 4481–4483.

[124] A. Ulman, *Formation and Structure of Self-Assembled Monolayers*, *Chemical Reviews*, Vol. 96(4) (**1996**) 1533–1554.

[125] S. Casalini et al., *Self-assembled monolayers in organic electronics*, *Chemical Society Reviews*, Vol. 46(1) (**2017**) 40–71.

[126] L. Grossmann et al., *On-surface photopolymerization of two-dimensional polymers ordered on the mesoscale*, *Nature Chemistry*, Vol. 13(8) (**2021**) 730–736.

[127] Q. Li et al., *Self-assembly directed one-step synthesis of [4]radialene on Cu(100) surfaces*, *Nature Communications*, Vol. 9(1) (**2018**) 3113.

[128] Z. Peng et al., *Using Self-Assembly to Control On-Surface Reactions*, Wiley-VCH, Weinheim, 1st Edition (**2022**).

[129] Q. Chen et al., *Steering On-Surface Reactions by a Self-Assembly Approach*, *Angewandte Chemie International Edition*, Vol. 56(18) (**2017**) 5026–5030.

[130] X. Zhou et al., *Steering Surface Reaction Dynamics with a Self-Assembly Strategy: Ullmann Coupling on Metal Surfaces*, *Angewandte Chemie International Edition*, Vol. 56(42) (**2017**) 12852–12856.

[131] Q. Fan et al., *Ultra-Long Poly(p-phenylene) via On-Surface Radical Ring-OpeningPolymerization for Access to Nonbenzenoid Carbon Nanoribbons*, *Submitted, In Revision* (**2025**).

[132] J. V. Barth, *Molecular Architectonic on Metal Surfaces*, *Annual Review of Physical Chemistry*, Vol. 58(1) (**2007**) 375–407.

[133] M. Stöhr et al., *Controlling Molecular Assembly in Two Dimensions: The Concentration Dependence of Thermally Induced 2D Aggregation of Molecules on a Metal Surface*, *Angewandte Chemie International Edition*, Vol. 44(45) (**2005**) 7394–7398.

[134] J. Weckesser et al., *Binding and ordering of C60 on Pd(110): Investigations at the local and mesoscopic scale*, *The Journal of Chemical Physics*, Vol. 115(19) (**2001**) 9001–9009.

[135] C. B. France et al., *Scanning Tunneling Microscopy Study of the Coverage-Dependent Structures of Pentacene on Au(111)*, *Langmuir*, Vol. 19(4) (**2003**) 1274–1281.

[136] H. L. Zhang et al., *Preferential Trapping of C60 in Nanomesh Voids*, *Journal of the American Chemical Society*, Vol. 130(9) (**2008**) 2720–2721.

[137] J. A. Smerdon et al., *Monolayer and bilayer pentacene on Cu(111)*, *Physical Review B*, Vol. 84(16) (**2011**) 165436.

[138] S. Zint et al., *Subsurface-Controlled Angular Rotation: Triphenylene Molecules on Au(111) Substrates*, *The Journal of Physical Chemistry C*, Vol. 120(3) (**2016**) 1615–1622.

[139] P. Maksymovych & D. B. Dougherty, *Molecular self-assembly guided by surface reconstruction: CH_3SH monolayer on the Au(111) surface*, *Surface Science*, Vol. 602(12) (**2008**) 2017–2024.

[140] M. Dreher et al., *Shape control in 2D molecular nanosheets by tuning anisotropic intermolecular interactions and assembly kinetics*, *Nature Communications*, Vol. 14(1) (**2023**) 1554.

[141] H. Glowatzki et al., *Impact of Fluorination on Initial Growth and Stability of Pentacene on Cu(111)*, *The Journal of Physical Chemistry C*, Vol. 116(14) (**2012**) 7726–7734.

[142] Y.-Y. Lo et al., *A Comparative Study on the Adsorption Behavior of Pentacene and Perfluoropentacene Molecules on Au(111) Surfaces*, *Japanese Journal of Applied Physics*, Vol. 52(10R) (**2013**) 101601.

[143] S. Lukas et al., *Novel Mechanism for Molecular Self-Assembly on Metal Substrates: Unidirectional Rows of Pentacene on Cu(110) Produced by a Substrate-Mediated Repulsion*, *Physical Review Letters*, Vol. 88(2) (**2001**) 028301.

[144] J. M. MacLeod & F. Rosei, *Molecular Self-Assembly on Graphene*, *Small*, Vol. 10(6) (**2013**) 1038–1049.

[145] A. M. Sweetman et al., *Mapping the force field of a hydrogen-bonded assembly*, *Nature Communications*, Vol. 5(1) (**2014**) 3931.

[146] S. Kawai et al., *Extended Halogen Bonding between Fully Fluorinated Aromatic Molecules*, *ACS Nano*, Vol. 9(3) (**2015**) 2574–2583.

[147] L. L. Patera et al., *Crystallization of a Two-Dimensional Hydrogen-Bonded Molecular Assembly: Evolution of the Local Structure Resolved by Atomic Force Microscopy*, *Angewandte Chemie International Edition*, Vol. 56(36) (**2017**) 10786–10790.

[148] G. R. Desiraju et al., *Definition of the halogen bond (IUPAC Recommendations 2013)*, *Pure and Applied Chemistry*, Vol. 85(8) (**2013**) 1711–1713.

[149] G. Cavallo et al., *The Halogen Bond*, *Chemical Reviews*, Vol. 116(4) (**2016**) 2478–2601.

[150] J. Teyssandier et al., *Halogen Bonding in Two-Dimensional Crystal Engineering*, *ChemistryOpen*, Vol. 9(2) (**2020**) 225–241.

[151] T. Clark et al., *Halogen bonding: the σ-hole: Proceedings of "Modeling interactions in biomolecules II"*, *Journal of Molecular Modeling*, Vol. 13(2) (**2006**) 291–296.

[152] P. Politzer et al., *An overview of halogen bonding*, *Journal of Molecular Modeling*, Vol. 13(2) (**2006**) 305–311.

[153] P. Metrangolo et al., *Fluorine-Centered Halogen Bonding: A Factor in Recognition Phenomena and Reactivity*, *Crystal Growth and Designs*, Vol. 11(9) (**2011**) 4238–4246.

[154] P. Metrangolo et al., *The fluorine atom as a halogen bond donor, viz. a positive site*, *CrystEngComm*, Vol. 13(22) (**2011**) 6593.

[155] K. C. Nicolaou, *The Emergence of the Structure of the Molecule and the Art of Its Synthesis*, *Angewandte Chemie International Edition*, Vol. 52(1) (**2012**) 131–146.

[156] K. C. Nicolaou, *Organic synthesis: the art and science of replicating the molecules of living nature and creating others like them in the laboratory*, *Proceedings of the Royal Society A: Mathematical, Physical and Engineering Sciences*, Vol. 470(2163) (**2014**) 20130690.

[157] M. Xi & B. E. Bent, *Mechanisms of the Ullmann coupling reaction in adsorbed monolayers*, *Journal of the American Chemical Society*, Vol. 115(16) (**1993**) 7426–7433.

[158] S.-W. Hla et al., *Inducing All Steps of a Chemical Reaction with the Scanning Tunneling Microscope Tip: Towards Single Molecule Engineering*, *Physical Review Letters*, Vol. 85(13) (**2000**) 2777–2780.

[159] P. C. M. Grim et al., *Submolecularly Resolved Polymerization of Diacetylene Molecules on the Graphite Surface Observed with Scanning Tunneling Microscopy*, *Angewandte Chemie International Edition in English*, Vol. 36(23) (**1997**) 2601–2603.

[160] J. M. Gottfried et al., *Direct Synthesis of a Metalloporphyrin Complex on a Surface*, *Journal of the American Chemical Society*, Vol. 128(17) (**2006**) 5644–5645.

[161] J. Cai et al., *Atomically precise bottom-up fabrication of graphene nanoribbons*, *Nature*, Vol. 466(7305) (**2010**) 470–473.

[162] H. Zhang et al., *On-Surface Synthesis of Rylene-Type Graphene Nanoribbons*, *Journal of the American Chemical Society*, Vol. 137(12) (**2015**) 4022–4025.

[163] R. Zuzak et al., *Synthesis and reactivity of a trigonal porous nanographene on a gold surface*, *Chemical Science*, Vol. 10(43) (**2019**) 10143–10148.

[164] M. Telychko et al., *Ultrahigh-yield on-surface synthesis and assembly of circumcoronene into a chiral electronic Kagome-honeycomb lattice*, *Science Advances*, Vol. 7(3) (**2021**) eabf0269.

[165] Y.-Q. Zhang et al., *Homo-coupling of terminal alkynes on a noble metal surface*, *Nature Communications*, Vol. 3(1) (**2012**) 1286.

[166] H. Gao et al., *Glaser Coupling at Metal Surfaces*, *Angewandte Chemie International Edition*, Vol. 52(14) (**2013**) 4024–4028.

[167] F. Klappenberger et al., *On-Surface Synthesis of Carbon-Based Scaffolds and Nanomaterials Using Terminal Alkynes*, *Accounts of Chemical Research*, Vol. 48(7) (**2015**) 2140–2150.

[168] F. Ullmann & J. Bielecki, *Ueber Synthesen in der Biphenylreihe*, *Berichte der deutschen chemischen Gesellschaft*, Vol. 34(2) (**1901**) 2174–2185.

[169] M. Ammon et al., *On-Surface Synthesis of Porous Carbon Nanoribbons from Polymer Chains*, *Journal of the American Chemical Society*, Vol. 139(37) (**2017**) 12976–12984.

[170] R. K. Houtsma et al., *On-Surface Ullmann-Type Coupling: Reaction Intermediates and Organometallic Polymer Growth*, *Advanced Materials Interfaces*, Vol. 11(4) (**2023**) 2300728.

[171] F. Schulz et al., *Precursor Geometry Determines the Growth Mechanism in Graphene Nanoribbons*, *The Journal of Physical Chemistry C*, Vol. 121(5) (**2017**) 2896–2904.

[172] K. A. Simonov et al., *From Graphene Nanoribbons on Cu(111) to Nanographene on Cu(110): Critical Role of Substrate Structure in the Bottom-Up Fabrication Strategy*, *ACS Nano*, Vol. 9(9) (**2015**) 8997–9011.

[173] P. H. Jacobse et al., *One Precursor but Two Types of Graphene Nanoribbons: On-Surface Transformations of 10,10'-Dichloro-9,9'-bianthryl on Ag(111)*, *The Journal of Physical Chemistry C*, Vol. 123(14) (**2019**) 8892–8901.

[174] P. Henkel et al., *Influence of the Coinage Metal(111) Surface on the Orientation of the σ Hole and the Halogen Bonding Strength of Bromo/Iodobenzene*, *The Journal of Physical Chemistry C*, Vol. 128(14) (**2024**) 5848–5859.

[175] M. Di Giovannantonio et al., *On-Surface Growth Dynamics of Graphene Nanoribbons: The Role of Halogen Functionalization*, *ACS Nano*, Vol. 12(1) (**2017**) 74–81.

[176] D. G. de Oteyza et al., *Substrate-Independent Growth of Atomically Precise Chiral Graphene Nanoribbons*, *ACS Nano*, Vol. 10(9) (**2016**) 9000–9008.

[177] Q. Zhong et al., *Substrate-Modulated Synthesis of Metal–Organic Hybrids by Tunable Multiple Aryl–Metal Bonds*, *Journal of the American Chemical Society*, Vol. 144(18) (**2022**) 8214–8222.

[178] J. H. Williams, *The molecular electric quadrupole moment and solid-state architecture*, *Accounts of Chemical Research*, Vol. 26(11) (**1993**) 593–598.

[179] G. W. Coates et al., *Phenyl–Perfluorophenyl Stacking Interactions: A New Strategy for Supermolecule Construction*, *Angewandte Chemie International Edition in English*, Vol. 36(3) (**1997**) 248–251.

[180] A. P. West Jr et al., *Theoretical Studies of the Supramolecular Synthon Benzene - - - Hexafluorobenzene*, *Journal of Physical Organic Chemistry*, Vol. 10(5) (**1997**) 347–350.

[181] K. W. Hipps et al., *A Self-Organized 2-Dimensional Bifunctional Structure Formed by Supramolecular Design*, *Journal of the American Chemical Society*, Vol. 124(10) (**2002**) 2126–2127.

[182] S. Kawai et al., *Obtaining Detailed Structural Information about Supramolecular Systems on Surfaces by Combining High-Resolution Force Microscopy with ab Initio Calculations*, *ACS Nano*, Vol. 7(10) (**2013**) 9098–9105.

[183] Z. Han et al., *Imaging the halogen bond in self-assembled halogenbenzenes on silver*, *Science*, Vol. 358(6360) (**2017**) 206–210.

[184] A. Steiner & K. Y. Amsharov, *The Rolling-Up of Oligophenylenes to Nanographenes by a HF-Zipping Approach*, *Angewandte Chemie International Edition*, Vol. 56(46) (**2017**) 14732–14736.

[185] M. Kolmer et al., *Fluorine-programmed nanozipping to tailored nanographenes on rutile TiO_2 surfaces*, *Science*, Vol. 363(6422) (**2019**) 57–60.

[186] H. Chen et al., *Stereoselective On-Surface Cyclodehydrofluorization of a Tetraphenylporphyrin and Homochiral Self-Assembly*, *Angewandte Chemie International Edition*, Vol. 59(40) (**2020**) 17413–17416.

[187] P. E. Hofmann et al., *Unilaterally Fluorinated Acenes: Synthesis and Solid-State Properties*, *Angewandte Chemie International Edition*, Vol. 59(38) (**2020**) 16501–16505.

[188] D. B. Dougherty et al., *Variable Temperature Scanning Tunneling Microscopy of Pentacene Monolayer and Bilayer Phases on Ag(111)*, *The Journal of Physical Chemistry C*, Vol. 112(51) (**2008**) 20334–20339.

[189] J. Götzen et al., *Structural Evolution of Perfluoro-Pentacene Films on Ag(111): Transition from 2D to 3D Growth*, *Langmuir*, Vol. 27(3) (**2010**) 993–999.

[190] D. de Oteyza et al., *Effect of fluorination on the molecule–substrate interactions of pentacene/Cu(100) interfaces*, *Chemical Physics Letters*, Vol. 490(1–3) (**2010**) 54–57.

[191] Q. Wang et al., *Impact of fluorination on interface energetics and growth of pentacene on Ag(111)*, *Beilstein Journal of Nanotechnology*, Vol. 11 (**2020**) 1361–1370.

[192] S. L. Wong et al., *Effect of Fluorination on the Molecular Packing of Perfluoropentacene and Pentacene Ultrathin Films on Ag (111)*, *The Journal of Physical Chemistry C*, Vol. 114(20) (**2010**) 9356–9361.

[193] N. Koch et al., *Adsorption-Induced Intramolecular Dipole: Correlating Molecular Conformation and Interface Electronic Structure*, *Journal of the American Chemical Society*, Vol. 130(23) (**2008**) 7300–7304.

[194] Y. Wang et al., *Simulation of the Au(111)-(22x$\sqrt{3}$) surface reconstruction*, *Physical Review B*, Vol. 75(23) (**2007**) 233416.

[195] S. Grabowski, *Hydrogen bonding*, *Challenges and Advances in Computational Chemistry and Physics Ser.*, Springer, Dordrecht, 3rd Edition (**2006**).

[196] B. Dereka et al., *Crossover from hydrogen to chemical bonding*, *Science*, Vol. 371(6525) (**2021**) 160–164.

[197] J. Lagoute et al., *Manipulation and adsorption-site mapping of single pentacene molecules on Cu(111)*, *Physical Review B*, Vol. 70(24) (**2004**) 245415.

[198] S. Kawai et al., *Systematic measurement of pentacene assembled on Cu(111) by bimodal dynamic force microscopy at room temperature*, *Physical Review B*, Vol. 84(8) (**2011**) 085429.

[199] S. Smalley et al., *Monolayer and Bilayer Perfluoropentacene on Cu(111)*, *The Journal of Physical Chemistry C*, Vol. 124(1) (**2019**) 653–658.

[200] X.-Q. Shi et al., *Interactions between Organics and Metal Surfaces in the Intermediate Regime between Physisorption and Chemisorption*, *The Journal of Physical Chemistry C*, Vol. 116(44) (**2012**) 23603–23607.

[201] A. Franco-Cañellas et al., *Resolving intramolecular-distortion changes induced by the partial fluorination of pentacene adsorbed on Cu(111)*, *Physical Review Materials*, Vol. 2(4) (**2018**) 044002.

[202] K. Müller et al., *Multimorphism in molecular monolayers: Pentacene on Cu(110)*, *Physical Review B*, Vol. 79(24) (**2009**) 245421.

[203] K. Müller et al., *Electronic Structure of an Organic/Metal Interface: Pentacene/Cu(110)*, *The Journal of Physical Chemistry C*, Vol. 116(44) (**2012**) 23465–23471.

[204] A. Baby et al., *Anchoring and Bending of Pentacene on Aluminum(001)*, *The Journal of Physical Chemistry C*, Vol. 119(7) (**2015**) 3624–3633.

[205] A. Ugolotti et al., *Chemisorption of Pentacene on Pt(111) with a Little Molecular Distortion*, *The Journal of Physical Chemistry C*, Vol. 121(41) (**2017**) 22797–22805.

[206] S. Henze et al., *Vertical bonding distances of PTCDA on Au(111) and Ag(111): Relation to the bonding type*, *Surface Science*, Vol. 601(6) (**2007**) 1566–1573.

[207] M.-C. Lu et al., *Pentacene on Au(111), Ag(111) and Cu(111): From physisoprtion to chemisorption*, *Journal of Physics: Condensed Matter*, Vol. 28(9) (**2016**) 094005.

[208] P. v. R. Schleyer et al., *The Acenes, Is There a Relationship between Aromatic Stabilization and Reactivity*, *Organic Letters*, Vol. 3(23) (**2001**) 3643–3646.

[209] M.-F. Cheng & W.-K. Li, *A computational study of the Diels–Alder reactions involving acenes: reactivity and aromaticity*, *Chemical Physics Letters*, Vol. 368(5–6) (**2003**) 630–638.

[210] N. Merino-Díez et al., *Width-Dependent Band Gap in Armchair Graphene Nanoribbons Reveals Fermi Level Pinning on Au(111)*, *ACS Nano*, Vol. 11(11) (**2017**) 11661–11668.

[211] A. Basagni et al., *Molecules–Oligomers–Nanowires–Graphene Nanoribbons: A Bottom-Up Stepwise On-Surface Covalent Synthesis Preserving Long-Range Order*, *Journal of the American Chemical Society*, Vol. 137(5) (**2015**) 1802–1808.

[212] V. V. Ivanovskaya et al., *On-Surface Synthesis and Evolution of Self-Assembled Poly(p-phenylene) Chains on Ag(111): A Joint Experimental and Theoretical Study*, *The Journal of Physical Chemistry C*, Vol. 127(1) (**2022**) 393–402.

[213] W. Wang et al., *Single-Molecule Resolution of an Organometallic Intermediate in a Surface-Supported Ullmann Coupling Reaction*, *Journal of the American Chemical Society*, Vol. 133(34) (**2011**) 13264–13267.

[214] X. Zhou et al., *On-surface synthesis approach to preparing one-dimensional organometallic and poly-p-phenylene chains*, *Materials Chemistry Frontiers*, Vol. 1(1) (**2017**) 119–127.

[215] B. Yuan et al., *Resolving Quinoid Structure in Poly(para-phenylene) Chains*, *Journal of the American Chemical Society*, Vol. 142(22) (**2020**) 10034–10041.

[216] S. E. Lewis, *Cycloparaphenylenes and related nanohoops*, *Chemical Society Reviews*, Vol. 44(8) (**2015**) 2221–2304.

[217] Q.-H. Guo et al., *Aromatic hydrocarbon belts*, *Nature Chemistry*, Vol. 13(5) (**2021**) 402–419.

[218] R. Jasti et al., *Synthesis, Characterization, and Theory of [9]-, [12]-, and [18]Cycloparaphenylene: Carbon Nanohoop Structures*, *Journal of the American Chemical Society*, Vol. 130(52) (**2008**) 17646–17647.

[219] E. Kayahara et al., *Synthesis and Characterization of [5]Cycloparaphenylene*, *Journal of the American Chemical Society*, Vol. 136(6) (**2014**) 2284–2287.

[220] J. Xia & R. Jasti, *Synthesis, Characterization, and Crystal Structure of [6]Cycloparaphenylene*, *Angewandte Chemie International Edition*, Vol. 51(10) (**2012**) 2474–2476.

[221] E. R. Darzi et al., *Selective Syntheses of [7]–[12]Cycloparaphenylenes Using Orthogonal Suzuki–Miyaura Cross-Coupling Reactions*, *The Journal of Organic Chemistry*, Vol. 77(15) (**2012**) 6624–6628.

[222] Y. Segawa et al., *Theoretical Studies on the Structures and Strain Energies of Cycloparaphenylenes*, *Organic Letters*, Vol. 12(10) (**2010**) 2262–2265.

[223] B. N. Taber et al., *Quantum Confinement of Surface Electrons by Molecular Nanohoop Corrals*, *The Journal of Physical Chemistry Letters*, Vol. 7(16) (**2016**) 3073–3077.

[224] A. Pérez-Guardiola et al., *Structure and Charge Transport Properties of Cycloparaphenylene Monolayers on Graphite*, *Advanced Materials Interfaces*, Vol. 6(8) (**2019**) 1801948.

[225] P. Hapala et al., *Origin of High-Resolution IETS-STM Images of Organic Molecules with Functionalized Tips*, *Physical Review Letters*, Vol. 113(22) (**2014**) 226101.

[226] S. Kawai et al., *Direct quantitative measurement of the C=O- - -H-C bond by atomic force microscopy*, *Science Advances*, Vol. 3(5) (**2017**) e1603258.

[227] H. Li et al., *Probing the deformation of [12]cycloparaphenylene molecular nanohoops adsorbed on metal surfaces by tip-enhanced Raman spectroscopy*, *The Journal of Chemical Physics*, Vol. 153(24) (**2020**) 244201.

[228] K. A. Simonov et al., *Effect of Substrate Chemistry on the Bottom-Up Fabrication of Graphene Nanoribbons: Combined Core-Level Spectroscopy and STM Study*, *The Journal of Physical Chemistry C*, Vol. 118(23) (**2014**) 12532–12540.

[229] J. Xia et al., *Gram-scale synthesis and crystal structures of [8]- and [10]CPP, and the solid-state structure of C60@[10]CPP*, *Chemical Science*, Vol. 3(10) (**2012**) 3018.

Acknowledgements

Wie bei den meisten wissenschaftlichen Arbeiten war auch die Erstellung dieser Dissertation nur durch die Zusammenarbeit mit vielen motivierten und engagierten Wissenschaftlerinnen und Wissenschaftlern möglich. Daher danke ich den folgenden Personen für ihre Unterstützung:

- Prof. Dr. André Schirmeisen für die Aufnahme in seine Forschungsgruppe, die Ermöglichung des durchgeführten Forschungsprojekts sowie den wissenschaftlichen Austausch während meines gesamten Promotionsstudiums
- Prof. Dr. Hermann A. Wegner für die Übernahme aller Aufgaben als Zweitbetreuer sowie die Begutachtung dieser Doktorarbeit
- PD Dr. Daniel Ebeling für seine alltägliche Unterstützung in experimentellen Anliegen, ohne die diese Arbeit in vorliegender Form nicht möglich gewesen wäre sowie den wissenschaftlichen Austausch während meines gesamten Promotionsstudiums
- Dem Hessischen Landesprogramm „LOEWE“, welches das Projekt „Principles of On-Surface Synthesis “ (PriOSS) finanziert hat
- Prof. Dr. Matthias T. Elm, der die Projekte meiner Bachelor- und Masterarbeit betreut hat und von dem ich zu großen Teilen gelernt habe, was gute wissenschaftliche Arbeit ausmacht
- Prof. Dr. Qigang Zhong and Dr. Daniel Martin-Jimenez for their help at the low temperature atomic force microscope
- Prof. Dr. Gregor Witte und Dr. Maximilian Dreher für die Bereitstellung der Präkursoren der unilateral fluorierten Pentacene und der theoretischen Kristallstruktur
- Prof. Dr. Simone Sanna und Dr. Marvin Krenz für die theoretischen Berechnungen im Projekt der unilateral fluorierten Pentacene
- Dr. Daniel Martin-Jimenez for performing the data analysis on the bending of unilaterally fluorinated pentacenes on Au(111) and Cu(111)
- Prof. Dr. Hermann A. Wegner und Dr. Daniel Kohrs für die Herstellung der Cycloparaphenylen Präkursoren
- Prof. Dr. Ralf Tonner-Zech und Jakob Schramm für die theoretischen Berechnungen im Projekt der Cycloparaphenylene
- Prof. Dr. Qigang Zhong for conducting the experiments on (6)Cycloparaphenylene

- Dr. Dirk Henkensmeier für die Möglichkeit Forschungserfahrung am Korea Institute of Science and Technology, Seoul, im Rahmen des DAAD RISE Programms zu sammeln

- Prof. Dr. Anastasiia Konovalova and Dr. Dmytro Serhiichuk, who became good friends during my research stay in Korea

- Prof. Dr. Udo Schwarz and Dr. Xinzhe Wang for the good collaboration during my research stay at Yale University, New Haven, CT

- Allen weiteren Mitgliedern der AG Schirmeisen: Alexandra Gabriel, Dr. Yiming Song, Dr. Jack Schmidt, Bernd Schmidt, Luca Kaufer, Jennifer Konrad, Xaver Hermann, Elias Eisenschmidt, Dr. Thomas Göddenhenrich, Dr. Jens Falter, PD Dr. Dirk Dietzel

- Den technischen Mitarbeitern, die geholfen haben, das Tieftemperatur Rasterkraftmikroskop in Betrieb zu halten: Yusuf Kücükkaplan, Holger Kern, Andreas Katzer

- Meinen Kommilitonen Juri Becker, Florian Rink, Lars-Erik Maurer, Sascha Kremer und Johannes Schubert

List of Publications

Publications included in this thesis:

Investigation of Hydrogen-Fluorine Interactions in Self-Assembled Unilaterally Fluorinated Pentacene Molecules on Au(111) and Cu(111)
M. Wiche, D. Martin-Jimenez, M. Krenz, M. Dreher, S. Sanna, G. Witte, A. Schirmeisen, D. Ebeling, *In preparation*

Temperature Induced On-Surface Ring-Opening Polymerization Reaction for the Synthesis of Nanoribbons: Strain Influence of Cycloparaphenylenes
M. Wiche, Q. Zhong, D. Kohrs, J. Schramm, R. Tonner-Zech, D. Ebeling, H. A. Wegner, A. Schirmeisen, *In preparation*

Publications contributed to during PhD program:

Effect of *tert*-Butyl Substitution on the Interactions of Cobalt Phthalocyanine with a Carbon Monoxide-Functionalized Tip
X. Wang, P. Zahl, **M. Wiche**, H. Wang, E. I. Altman, U. D. Schwarz
J. Phys. Chem. Lett., 2025, 16, 3664-3671

Low temperature multimode atomic force microscopy using an active MEMS cantilever
M. G. Ruppert, **M. Wiche**, A. Schirmeisen, D. Ebeling
Nanoscale, 2025, 17, 10600-10608

Molecular identification via molecular fingerprint extraction from atomic force microscopy images
M. González Lastre, P. Pou, **M. Wiche**, D. Ebeling, A. Schirmeisen, R. Pérez
Journal of Cheminformatics, 2024, 16:130

Publications contributed to before PhD program:

Unexpectedly High Electronic Partial Conductivity of Porous Yttria-Stabilized Zirconia Thin Films
E. Celik, A. Usler, **M. Wiche**, A. Mazilkin, T. Brezesinski, R. A. De Souza, M. T. Elm
J. Phys. Chem. C 2025, 129, 27, 12585–12594

State of Charge-Dependent Impedance Spectroscopy as a Helpful Tool to Identify Reasons for Fast Capacity Fading in All-Solid-State Batteries
M. Wiche, Y. Yusim, K. Vettori, R. Ruess, A. Henss, M. T. Elm
ACS Appl. Mater. Interfaces, 2024, 16, 3253-3259

Liquid crystal-like active layer for high-performance organic field-effect transistors
Z. Wang, D. Martin-Jimenez, Y. Zhang, **M. Wiche**, L. Liu, D. Ebeling, Q. Zhong, F. Fontein, A. Schirmeisen, L. Huang, Z. Wang, W. Wang, L. Chi
Sci. China Mater., 2023, 66, 1518-1526

Optimized atomic layer deposition of homogeneous, conductive Al_2O_3 coatings for high-nickel NCM containing ready-to-use electrodes
R. S. Negi, S. P. Culver, **M. Wiche**, S. Ahmed, K. Volz, M. T. Elm
Phys. Chem. Chem. Phys., 2021, 23, 6725-6737

„Ich erkläre: Ich habe die vorgelegte Dissertation selbstständig und ohne unerlaubte fremde Hilfe und nur mit den Hilfen angefertigt, die ich in der Dissertation angegeben habe. Alle Textstellen, die wörtlich oder sinngemäß aus veröffentlichten Schriften entnommen sind, und alle Angaben, die auf mündlichen Auskünften beruhen, sind als solche kenntlich gemacht. Ich stimme einer evtl. Überprüfung meiner Dissertation durch eine Antiplagiat-Software zu. Bei den von mir durchgeführten und in der Dissertation erwähnten Untersuchungen habe ich die Grundsätze guter wissenschaftlicher Praxis, wie sie in der „Satzung der Justus-Liebig-Universität Gießen zur Sicherung guter wissenschaftlicher Praxis“ niedergelegt sind, eingehalten.“

Angaben zu auf künstlicher Intelligenz (KI) basierender Hilfen wie ChatGPT oder SchulKI von OpenAI oder Gemini von Google zur Erstellung meiner Dissertation (Zutreffendes angekreuzt):

☐ Ich habe bei der Erstellung dieses Textes kein KI-Tool verwendet.

☒ Ich habe ein KI-Tool in den folgenden Bereichen eingesetzt (Mehrfachnennungen möglich):

- ☐ Ideen finden, meine Kreativität anregen
- ☐ Verstehen von Konzepten, Recherche von Fakten und Definitionen
- ☒ Optimierung eines von mir verfassten Textes
- ☐ Erstellen ganzer Textpassagen nach meinen Vorgaben

Folgende KI-Tools habe ich verwendet, damit aufgeführte Teile meines Textes von dem Tool wie folgt profitiert haben:

OpenAI, GPT-40 mini (in der Maske des JLU kiChat):

Optimierung einzelner von mir verfasster Sätze in allen Kapiteln der Dissertation
(Satzbau; Satzstruktur; Rechtschreibung)

ki@JLU, Text (in der Maske des JLU kiChat):

Optimierung einzelner von mir verfasster Sätze in allen Kapiteln der Dissertation
(Satzbau; Satzstruktur; Rechtschreibung)

DeepL:

Übersetzung einzelner von mir verfasster Textstellen von der deutschen in die englische Sprache in allen Kapiteln der Dissertation

Datum: _____ Unterschrift: _____